The Role of Unsteady Hydrodynamics in the Propulsive Performance of a Self-Propelled Bioinspired Vehicle

Thesis by

Lydia Ann Ruiz

In Partial Fulfillment of the Requirements

for the Degree of

Doctor of Philosophy

California Institute of Technology

Pasadena, California

2010

(Defended August 10, 2009)

To my family, friends, and God who gave me inspiration.

Acknowledgments

I would like to begin my acknowledgments by saying that I am fortunate to be a graduate student of Professor John Dabiri. Through his creativity and insight into scientific discovery, he has inspired me in becoming an innovative scientist and developing a passion for scientific inquisitiveness. He has been and will always be a great role model and friend.

I would also like to acknowledge and give my appreciation to my defense committee: Professor Morteza Gharib, Professor Tim Colonius, and Professor Joseph Shepherd. I am grateful to have had the opportunity to conduct research under Professor Morteza Gharib during my first couple of years at Caltech. Thank you Professor Colonius and Professor Shepherd for your guidance and advice during my research and for reviewing my thesis.

I would like to acknowledge the members of my research group who have been with me during the development of my research, providing helpful comments and assistance in the laboratory. I would like to acknowledge Martha Salcedo for her help with administrative matters and for her friendship. I must acknowledge both the Aeronautics and Physics machine shops for their expertise in manufacturing my experimental components in a timely manner.

I am grateful for all the friendships that I have developed during my time at Caltech. My friends at Caltech have been a great source of strength and laughter with special thanks to Jennifer and Christian Franck, Brenda Hernandez, Kakani Katija, and Sharlotte and Richard Kramer.

I would like to use this opportunity to thank a few role models that have made a tremendous impact in my life during my undergraduate studies. Without these people I would not have made it to Caltech. Thank you to Professor Jonathan Freund, my first fluids instructor at UCLA. He helped me develop an interest in the area of fluid mechanics. I would also like to acknowledge my undergraduate

research advisor, Ann Karagozian. Through an undergraduate research program, I was given the opportunity to conduct research in her laboratories for 3 years. Without that opportunity, I would have never discovered what graduate school had to offer. Professor Ann Karagozian has been a great supporter in my life.

I must acknowledge my mother and father. They have always encouraged me to work hard, strive to do well in all things, and maintain a healthy life balance. Their love is unending.

I would like to state a few special words of acknowledgment to my best friend, husband, and soulmate, Arturo. Without his patience, love, support, and encouragement I would not have made the choice to pursue a graduate career. He provided companionship and assistance during my late-night experiments in the laboratory.

The most important acknowledgment is to God. He has been the true foundation and source of strength of all that I do and all that I am. He has blessed me with tremendous opportunities that have made me the person I am today. He has taught me to persevere through many challenges in hope of all good things to come.

Abstract

Aquatic animals differ from typical engineering systems in their method of locomotion. In general, aquatic animals propel using unsteady dynamics producing vortex rings. Researchers have long shown interest in designing devices that resemble their shape and propulsive behavior. Traditional definitions of propulsive efficiency used to model these behaviors have not taken unsteady effects into account and are typically based on steady flow through propellers or rocket motors. Measurements of aquatic animals based on these quasi-steady metrics have suggested propulsive efficiencies over 80% when utilizing certain swimming kinematics. However, the mechanical efficiency of muscle-actuated biological propulsion has been found to be much lower, typically less than 20%. It is important to take into account the total efficiency of the system, the product of the mechanical and propulsive efficiency, when designing and implementing a biologically inspired propulsive device.

The purpose of my research is to make a direct, experimental comparison between biological and engineering propulsion systems. For this study, I designed an underwater vehicle that has the capability of producing either a steady or unsteady jet for propulsion, akin to a squid and jellyfish, while utilizing the same mechanical efficiency. I show that it is unnecessary to take an approach that mimics animal shape and kinematics to achieve the associated propulsive performance. A bioinspired, propeller-based platform that mimics animal wake dynamics can be similarly effective.

A study on how vortex dynamics plays a key role in improving the propulsive efficiency of pulsed jet propulsion was conducted. Measurements of propulsive performance resulted in superior performance for the pulsed-jet configuration in comparison to the steady jet configuration particularly at higher motor speeds. The analysis demonstrated that vortex ring formation led to the acceleration of two classes of ambient fluid, entrained and added mass, and this consequently led to an increased

total fluid impulse of the jet and propulsive performance. The first source of ambient fluid acceleration investigated was entrained mass. The magnitude of the entrainment ratio was measured and found to be smaller for the steady jet mode of propulsion in comparison to the pulsed jet mode of propulsion given comparable motor speeds. The role of the added mass effect was also investigated in increasing propulsive performance. A model developed by Krueger is used to determine the fraction of the total impulse imparted to the flow that was contributed by the added mass effect. Results demonstrated that the added mass effect associated with the acceleration of ambient fluid at the initiation of a starting jet provides an increase in the total impulse and is thus a source for increased propulsive performance. Last, a model was developed to investigate how an increase in the total fluid impulse due to vortex ring formation is related to the propulsive efficiency. Results obtained using the model are in agreement, within uncertainty, with previous experimental results for the measurement of propulsive efficiency. The results support that the additional force generated from the acceleration of two classes of ambient fluid are the source of increased propulsive efficiency for the pulsed jet configuration in comparison to the steady jet configuration. This model serves as an additional metric for determining the propulsive efficiency of a system utilizing pulsed jet propulsion.

Contents

Contents viii

List of Figures xii

List of Tables xv

Nomenclature xvi

1 Introduction and Background 1

1.1 Motivation . . . 1

1.2 Background . . . 2

1.2.1 Pulsed Jets . . . 2

1.2.2 Vortex Ring Formation . . . 3

1.2.3 Bio-Mimetic and Bioinspired Devices . . . 5

1.2.4 Metrics of Propulsive Performance . . . 6

1.3 Objectives . . . 7

1.4 Thesis Breakdown . . . 8

2 Vehicle Design, Construction, and Operation 9

2.1 Introduction . . . 9

2.2 Detailed Description of Vehicle Design and Construction . . . 9

2.2.1 Vehicle Components . . . 9

2.2.1.1 Mechanical Components . . . 10

2.2.1.2 Internal Electrical Components . . . 13

2.2.2 Description of Jet Mechanism 14

2.2.2.1 Unsteady Jet Configuration 15

2.2.2.2 Steady Jet Configuration 16

2.2.3 Vehicle Operation 18

3 Experimental Techniques and Procedures 20

3.1 Introduction 20

3.2 Test Facility 21

3.3 Measurement Techniques and Applications (Stationary Configuration) 22

3.3.1 Data-Acquisition System 22

3.3.2 Digital Particle Image Velocimetry Measurements 22

3.3.3 Planar Laser-Induced Fluorescence Measurements 24

3.4 Measurement Techniques and Applications (Self-Propelled Configuration) 25

3.4.1 Data Acquisition System 25

3.4.2 Data Acquisition Software 27

3.4.2.1 Motorized Traverse Telemetry 29

3.4.2.2 Distance Sensor Description and Calibration 31

3.4.3 System Control and Automation 32

3.4.4 LDV Measurements 35

3.4.5 Drag Measurements 39

3.4.5.1 Measurement Procedure 39

3.4.5.2 Calibration of Speed versus Drag Force 40

3.4.5.3 Discussion of Spatial Variation of Drag Force Along Flume Rails . . 41

4 Empirical Demonstration and Investigation of Propulsive Performance 46

4.1 Introduction 46

4.2 Experimental Conditions 47

4.3 Jet Characterization: Flow Visualization 49

4.3.1 PIV Measurements 49
4.3.1.1 Inner Shell Modification and Effect to Unsteady Jet Formation . . . 49
4.3.1.2 Steady Jet Configuration 51
4.3.2 PLIF Measurements 52
4.4 Measurement of Propulsive Performance 56
4.4.1 Comparison of Froude Efficiency for Both Steady and Unsteady Jet Propulsion 56
4.4.2 Effects of Increased Vehicle Speed on Froude Efficiency Model 58
4.4.3 Comparison of Total Hydrodynamic Efficiency for Both Steady and Unsteady Jet Propulsion 59
4.5 Comparison of Propulsive Efficiency to Other Biological Organisms 70
4.6 Comparison of Power Consumption for Both Steady and Unsteady Jet Propulsion . 70
4.7 Conclusion 74

5 Role of Entrainment and Added Mass in Propulsive Performance 76

5.1 Introduction 76
5.2 Experimental Conditions 77
5.3 Relationship of Nozzle-Exit Overpressure to the Hydrodynamic Impulse 78
5.4 Relationship of Entrainment to Improved Propulsive Performance 79
5.4.1 Comparison of Velocity Profiles Obtained Using LDV 80
5.4.1.1 Comparison of Velocity Profiles for Uz 80
5.4.1.2 Comparison of Velocity Profiles for Ux 81
5.4.2 Measurement of Entrainment Ratio for Both Steady and Unsteady Jet Propulsion with Equivalent Jet Speeds 82
5.5 Model of Proposed Contribution of Added Mass to Propulsive Performance 89
5.6 Model of Proposed Contribution of Pressure Impulse to Propulsive Efficiency 91
5.6.1 Measurement of Propulsive Efficiency Using Estimated Total Impulse 93
5.7 Conclusion 96

6 Summary and Recommendations **100**

6.1 Summary of Results 100

6.2 Recommendations for Future Work 104

Appendix A Submarine DAQ Implementation Details **106**

Appendix B Traverse Controller Implementation Details **113**

Appendix C Electrical Box Wiring Diagram **117**

Appendix D Summary of Data from Drag Experiments **118**

Appendix E Summary of Data from Performance Studies **121**

Appendix F Summary of Results Obtained Using Modeled Thrust Force **124**

Bibliography **125**

List of Figures

1.1 Illustration of the two classes of ambient fluid accelerated by a vortex ring. 5

2.1 Schematic and image of the fully assembled vehicle. 10

2.2 Image of the anterior cap and the motor housing of the vehicle. 11

2.3 Upstream image of the fluid housing and the fluid nozzle components. 12

2.4 Images of electrical components internal to the vehicle. 14

2.5 Gearing mechanism used to generate both steady and unsteady jet propulsion. 14

2.6 Principle of operation for pulsed jet configuration. 16

2.7 Upstream view of the unsteady rotating shell mounted inside the vehicle. 17

2.8 Images of inner rotating shells for both pulsed jet and steady jet vehicle configurations. 17

2.9 Principle of operation for steady jet configuration. 18

2.10 Schematic of electrical wiring necessary for the operation of the vehicle. 19

3.1 Images of facility and control panel for motorized traverse. 21

3.2 Schematic of DPIV setup for the jet flow of the vehicle in a stationary configuration. . 23

3.3 Schematic diagram of camera frame rate and laser pulsing. 24

3.4 Screenshot of Submarine DAQ user interface. 28

3.5 Screenshot of Traverse Monitor user interface. 30

3.6 Plot of distance sensor calibration. 32

3.7 Screenshot of the Traverse Controller user interface. 33

3.8 Schematic of LDV assembly mounted to the traverse of the vehicle. 36

3.9 FFT of the jet center speed at two pulsing frequencies. 42

3.10 Load cell calibration under compression, y = 0.0019x − 0.003. 43
3.11 Schematic of load cell assembly. 43
3.12 Image of load cell in drag experimental setup. 44
3.13 Drag measurements of traverse both with and without vehicle. 44
3.14 Graph illustrating the variation of the drag force along the flume rails. 45

4.1 Inner shell geometries tested. 49
4.2 Instantaneous velocity field of the jet with 26^o fluid opening. 50
4.3 Instantaneous velocity field of the jet with two unsteady shell geometries. 53
4.4 Instantaneous velocity field and vorticity contour of the jet using final unsteady shell geometry. 54
4.5 Instantaneous velocity field of the jet with vehicle in steady mode of propulsion. . . . 55
4.6 PLIF images illustrating a larger wake size for the pulsed jet in comparison to the steady jet. 55
4.7 Illustration of typical variation in vehicle speed over the duration of an experiment. . 61
4.8 Froude efficiency versus motor speed for motor 1. 62
4.9 Normalized Froude efficiency versus motor speed for motor 1. 62
4.10 Froude efficiency versus motor speed for motor 2. 63
4.11 Normalized Froude efficiency versus motor speed for motor 2. 63
4.12 Compiled results for the measure of Froude efficiency versus motor speed. 64
4.13 Graph of jet speed versus motor speed for both motors. 64
4.14 Formation time versus vehicle speed. 65
4.15 Graph of jet speed versus motor speed for motor 1. 65
4.16 Graph of Froude efficiency versus vehicle speed. 66
4.17 Graph of Froude efficiency versus higher vehicle speed. 66
4.18 Total hydrodynamic efficiency versus motor speed for motor 1. 67
4.19 Normalized total hydrodynamic efficiency versus motor speed for motor 1. 67
4.20 Total hydrodynamic efficiency versus motor speed for motor 2. 68

4.21 Normalized total hydrodynamic efficiency versus motor speed for motor 2. 68

4.22 Compiled total hydrodynamic efficiency versus motor speed. 69

4.23 Graph of power coefficient versus motor speed. 72

4.24 Graph of normalized power coefficient versus motor speed. 73

5.1 Schematic illustrating the translation of the LDV probe volume. 78

5.2 Entrainment ratio. 80

5.3 Variation of axial jet velocity U_z with translational distance in the x direction. 84

5.4 Variation of axial velocity fluctuations w′ with translational distance in the x direction. 85

5.5 Variation of jet velocity U_x with translational distance in the x direction. 86

5.6 Variation of velocity fluctuations u′ with translational distance in the x direction. . . 87

5.7 Relationship between entrainment ratio and motor speed. 88

5.8 Relationship between $I_p(t)/I(t)$ and motor speed. 90

5.9 Plot of ambient fluid entrainment versus downstream distance. 94

5.10 Illustration of accuracy of model in estimating propulsive efficiency. 96

A.1 Submarine DAQ flow chart. 106

A.2 Submarine DAQ VI measure state. 108

A.3 Submarine DAQ VI calibrate state. 109

A.4 Submarine DAQ VI control state. 110

A.5 Submarine DAQ VI log state. 111

A.6 Submarine DAQ VI display state. 112

B.1 Traverse Controller flow chart. 114

B.2 Traverse Controller VI run state. 115

B.3 PID algorithm implementation. 116

C.1 Electrical box wiring diagram. 117

List of Tables

3.1 PI feedback control parameters 35

5.1 Summary of entrainment studies for both pulsed and steady jet propulsion 83

5.2 Summary of parameters used in estimation of pressure impulse model 91

D.1 Summary of experimental data for drag on traverse with vehicle attached 119

D.2 Summary of experimental data for drag on traverse without vehicle attached 120

E.1 Summary of performance data using initial motor. 122

E.2 Summary of performance data using second motor. 123

F.1 Summary of results obtained using modeled thrust force 124

Nomenclature

Greek symbols

η_F Froude efficiency, equation (4.1), page 56

η_{hydro} Hydrodynamic efficiency, equation (4.2), page 59

η_{mech} Mechanical efficiency, equation (1.1), page 6

η_o Overall efficiency, equation (1.0), page 6

η_{prop} Propulsive efficiency, equation (1.2), page 7

η_{th} Mechanical efficiency for shaft power devices, equation (1.1), page 6

ω Angular velocity of the inner rotating shell, equation (4.1), page 50

ρ Density of the fluid, equation (4.4), page 71

σ_{drag} Standard deviation in drag force, page 40

σ_{speed} Standard deviation in speed, page 40

θ_{io} Inner rotational shell fluid opening, page 49

Roman characters

$\dot{m}$ Mass flow rate through the propulsion system, equation (1.3), page 7

$\overline{T_p}$ Average thrust generated during a pulse, equation (5.5), page 90

A_j Area of jet exit, equation (4.3), page 59

C_p Power coefficient, equation (4.4), page 71

C_{AM} Added-mass coefficient of a vortex ring, equation (5.7), page 92

D Diameter of jet exit, equation (4.0), page 49

DAQ Data acquisition, page 27

$DPIV$ Digital particle image velocimetry, page 22

e PI feedback control measured error, equation (3.1), page 34

f LDV sinusoid frequency, page 35

FFT Fast Fourier transform, page 37

$I(t)$ Total impulse supplied to flow or magnitude of the hydrodynamic impulse, equation (5.0), page 78

$I_p(t)$ Impulse added to the flow by nozzle exit overpressure, equation (5.1), page 79

$I_U(t)$ Impulse added to the flow by momentum flux from the jet, equation (5.1), page 79

I_{out} PI feedback control integral term, equation (3.4), page 34

I_{state_1} PI feedback control previous integral state, equation (3.3), page 34

I_{state_2} PI feedback control current integral state, equation (3.3), page 34

K_i PI feedback control integral coefficient, equation (3.4), page 34

K_p PI feedback control proportional coefficient, equation (3.2), page 34

L Pulse length, page 3

LDV Laser Doppler velocimetry, page 35

M Added mass of vortex ring, equation (5.2), page 79

m_{disk} Added mass of circular disk, equation (5.3), page 89

$m_{ejected}$ Mass of fluid ejected from nozzle, equation (5.2), page 79

$m_{entrained}$ Mass of ambient fluid entrained into the vortex ring, equation (5.2), page 79

$miniLDV$ Miniature laser Doppler velocimeter, page 36

MV PI feedback control manipulated variable, equation (3.5), page 34

P_s Shaft power, equation (1.2), page 7

P_{input} Power input supplied to motor, equation (4.3), page 70

P_{in} Power input, equation (1.2), page 7

P_{out} PI feedback control proportional term, equation (3.2), page 34

PI Proportional integral (control loop feedback mechanism), page 33

$PLIF$ Planar laser induced fluorescence, page 24

PV PI feedback control processed variable, equation (3.1), page 34

Q Volumetric flow rate through jet exit, equation (5.3), page 79

Q_{avg} Average measurement of the volumetric flow rate, page 91

$Q_{entrained}$ Volumetric flow rate of entrained flow into jet wake, equation (5.10), page 93

r Jet radius, equation (5.3), page 80

Re_j Reynolds number based on average jet velocity, equation (4.0), page 49

ROS Remote optical sensor, page 13

S Wetted surface area of the vehicle, equation (4.4), page 71

SP PI feedback control setpoint, equation (3.1), page 34

Sr_L Dimensionless pulsing frequency, page 3

$SWOS$ Steady jet without rotating shell, page 57

T Thrust developed by the propulsion mechanism, equation (1.2), page 7

t Fluid discharge time, equation (4.1), page 50

t^* Formation time, equation (4.0), page 49

t_p Pulse duration, equation (5.7), page 91

$TDMS$ Technical Data Management Streaming, page 29

U Speed of the vehicle relative to the surrounding fluid, equation (1.2), page 7

u' Root mean square velocity fluctuation in U_x, equation (5.3), page 81

U_j Jet speed, equation (1.3), page 7

U_v Average vehicle speed, equation (4.2), page 56

U_z Average axial velocity, equation (5.3), page 80

U_{avg} Average jet velocity, equation (4.0), page 49

U_{max} Maximum of $U_J(t)$ over the interval of a pulse, equation (5.3), page 89

V_{cc} Supply voltage, page 31

$VCUUV$ Vorticity control unmanned undersea vehicle, page 6

VI Virtual instrument, page 27

W Translational velocity of a vortex ring, equation (5.2), page 79

w' Root mean square velocity fluctuation in U_z, equation (5.3), page 80

Chapter 1

Introduction and Background

1.1 Motivation

The AAAS (American Association for the Advancement of Science) Atlas of Population and Environment has stated that during the past 50 years, global consumption of commercial energy has risen more than fourfold, far outpacing the rise in population. In one way or another, energy comes from natural resources, whether it be fossil fuels such as coal and oil, living resources such as timber and biomass, nuclear fuel such as uranium, or renewable resources such as flowing water, wind or power from the sun. A generation ago, there was concern that fossil fuels would run out, plunging the world into an energy crisis. Today, the fear is that their continued use might destroy the global climate through carbon dioxide emission.

Energy is used to illuminate, heat and cool our living spaces, for cooking, manufacturing, transportation, and for myriad other purposes. About 29% of our total energy consumption is used for tranportation. Statistics from the U.S. Government, Energy Information Administration estimate that the total delivered energy consumption in the transportation sector as of this writing is 28.8 quadrillion Btu and it is projected to increase to 31.9 quadrillion Btu in 2030. A shift to cleaner, more-efficient sources of energy is vital.

Looking at nature for inspiration in engineering design, a major difference can be noted in the method of locomotion. Animals typically propel using unsteady dynamics producing vortex rings. Vortex rings have been shown in the wakes of fish such as mackerel (Borazjani and Sotiropoulos 2008),

sunfish (Drucker and Lauder 1999), eels (Tytell and Lauder 2004) and other marine animals such as squid (Anderson and Grosenbaugh 2005) and jellyfish (Dabiri et al. 2005) to name a few. Using unsteady jet propulsion, aquatic animals have been shown to display high propulsive efficiencies. Fish (1998) has shown that dolphins can display propulsive efficiencies as high as 84% using certain swimming kinematics. The theoretical anaylysis of Weihs (1977) indicates that an unsteady jet with vortex ring formation can augment thrust and efficiency by nearly an order of magnitude compared to the steady jet propulsion system. It is essential to consider the role of vortex ring formation in increasing the propulsive performance of engineered systems.

1.2 Background

1.2.1 Pulsed Jets

When an organism or vehicle uses pulsed jet propulsion for locomotion, the jet created is highly unsteady and consists of bursts of fluid. A multiplicity of such bursts of fluid or pulses, is called a fully pulsed jet and can lead to a multiplicity of vortex rings in the jet wake. When the unsteady component is a small fraction of the mean jet velocity, this case is referred to as a forced jet. In the limit that the jet velocity returns to zero in between pulses, even for a finite amount of time, the jet is referred to as a fully pulsed jet. The literature on fully pulsed jets is not as abundant in comparison to the literature for forced jets.

Most of the literature on forced jets has focused on the dynamics of the mean and fluctuating velocities of the jet, on the enhancement of ambient fluid entrainment and mixing effects resulting from forcing. When a jet is used for thrust augmentation, or the mixing process, a large mass entrainment near the jet nozzle is desired. Research has also focused on the dynamics of coherent structures produced in the near jet region and the transition to turbulence, (Broze and Hussain 1994, 1996). Crow and Champagne (1971) were among the first to recognize the importance of orderly structures in turbulent jets. Work by Vermeulen et al. (1992) shows that entrainment can be enhanced by acoustic excitation of the jet flow.

Fully pulsed jets have been studied experimentally by Bremhorst and Hollist (1990), Bremhorst and Gehrke (2000) and Krueger (2005). Bremhorst and Hollist (1990) obtained velocity field measurements up to 100 jet diameters downstream from the nozzle. They noted that the ordered nature of the leading vortex produced by each pulse yielded a region of pulse-dominated flow that extended to 50 diameters downstream, and it was not until after this point that the centerline velocity decay and centerline turbulence intensities approached those expected for a steady jet. The Reynolds stresses were considerably larger for the fully pulsed jet than for a steady jet and were considered to be responsible for increased entrainment due to the vortex ring formed by each pulse. Bremhorst and Gehrke (2000) obtained measurements of Reynold stresses and energy budgets in the downstream region (distances greater than 50 diameters from the nozzle) of the jet for the application of modeling turbulence. Krueger (2005) investigated thrust augmentation in a fully pulsed jet as a function of dimensionless pulse size (L/D) and dimensionless frequency (Sr_L). Significant thrust augmentation was observed over the entire parameter range tested when compared to an equivalent steady jet with an identical mass flux. Augmentation appeared to be greatest at small values of L/D. In addition, Krueger noted that as Sr_L increases, the vorticity from preceding pulses is closer to the nozzle at the ejection of each pulse, requiring less fluid to be accelerated by the issuing pulse, therefore reducing nozzle exit overpressure.

1.2.2 Vortex Ring Formation

The concepts of vortex ring formation and issues related to the dynamics of laminar and turbulent vortex rings have been reviewed by Lim and Nickels (1995) and Shariff and Leonard (1992). Vortex rings are most commonly formed in a laboratory using piston-cylinder arrangements. They are generated by the motion of a piston pushing a column of fluid of length L through an orifice or nozzle of diameter D. As fluid is ejected this results in the separation of the boundary layer at the edge of the orifice or nozzle and subsequent spiral roll up. When a single burst of fluid is issued from a nozzle into a quiescent fluid, it is referred to as a starting jet. The evolution of the vortex ring size, position, and circulation have been studied experimentally by Didden (1979), Maxworthy

(1977) and Glezer (1988). In Didden (1979), the research provided insight on the role of internal and external boundary layers in the formation process and circulation of the vortex ring. Saffman (1978) and Pullin (1979) modeled the initial roll up process using similarity theory and obtained expressions for the vortex ring trajectory, circulation, and its vorticity distribution. Nitsche (1996) determined the properties of a vortex ring as a function of the piston motion and found that the initial ring diameter, core size and circulation are well predicted by planar similarity theory.

Most work regarding vortex ring formation ignores the roll up process of the vortex sheet. In most instances, the amount of each dynamic quantity (circulation, impulse, and energy) generated by the piston-cylinder is modeled using a slug flow model where the ejected fluid is seen as having a uniform velocity equal to the piston velocity and pressure equal to the ambient pressure. Glezer (1988) used this model to determine vortex ring impulse. Despite oversimplification, the slug flow model is still used in vortex ring research.

Work by Gharib et al. (1998) showed that the circulation, impulse, and energy of a vortex ring is dependent on stroke ratio. The maximum circulation that a vortex ring can attain during its formation is reached at a stroke ratio of approximately 4, which is referred to as the formation number. Krueger and Gharib (2003) investigated the impulse and thrust generated by starting jets for L/D ratios in the range of 2–8. He showed that a local maximum in average thrust exists for pulses near L/D values associated with vortex rings whose circulation had been maximized. This maximization was shown to be related to the nozzle exit overpressure generated during vortex ring formation. Work by Krueger et al. (2006) examined the formation number of vortex rings formed in uniform background coflow and Dabiri and Gharib (2004) in an imposed bulk counterflow.

The benefit of vortex ring formation for propulsion arises due to the entrainment of ambient fluid by the forming vortex ring (Auerbach 1991, Dabiri 2004, Olcay and Krueger 2008) in addition to the added mass of nonentrained fluid surrounding the vortex that must be accelerated with the vortex ring (Krueger and Gharib 2003). The schematic of a fully developed vortex ring on the left of figure 1.1 illustrates the two classes of ambient fluid accelerated by a starting jet. The ambient fluid entrained into the vortex ring as the shear layer from the nozzle boundary layer rolls up into

a ring near the nozzle exit was first noted by Didden (1979). This effect is apparent by the dark bands in the vortex ring in the planar laser-induced fluorescence image in figure 1.1. The second benefit of vortex ring formation, the added mass effect, occurs as a portion of the fluid in front of the jet must be accelerated out of the way when the starting jet is initiated and ambient fluid must be brought behind the vortex ring to preserve continuity once the vortex begins moving downstream. This effect is illustrated on the left image in figure 1.1 and is represented by the outer dotted oval. The added mass effect is mathematically equivalent to the added mass carried with a solid body in potential flow and can be computed in terms of the velocity potential of the flow outside of the vortex (Dabiri 2006).

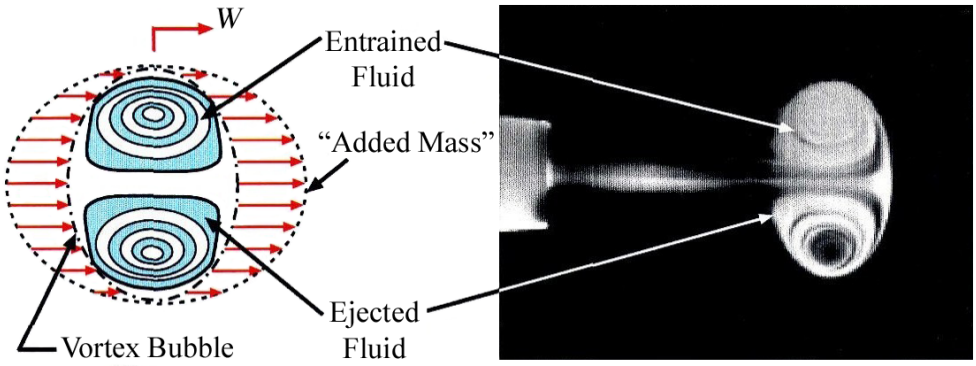

Figure 1.1. Illustration of the two classes of ambient fluid accelerated by a vortex ring. The image on the right is a PLIF flow visualization, Krueger (2001).

1.2.3 Bio-Mimetic and Bioinspired Devices

A rapidly growing area of interest in hydrodynamics and hydropropulsion is the application of strategies used by swimming animals in order to improve current propulsive technology. These efforts have largely involved mimicking the shape and kinematics of swimming animals in order to achieve there propulsive performance and are classified as bio-mimetic devices. In recent years, research in fluid flow mechanisms used by fish for propulsion and maneuvering has demonstrated the utility of bio-propulsion for undersea vehicles. Barrett et al. (1999) illustrated with his RoboTuna apparatus, that manipulation of the body of an undersea vehicle in a fishlike manner could significantly enhance energetic performance. Anderson and Chhabra (2002) designed and developed a vehicle that

uses vorticity control propulsion and maneuvering, known as VCUUV (vorticity control unmanned undersea vehicle) to study the energetics and maneuvering performance of fish-swimming propulsion. VCUUV is a self-contained free-swimming research vehicle that follows the morphology and kinematics of yellowfin tuna. Others, (Tangorra et al. 2007) have been inspired by the coordinated motion of a fish fin and have embarked on research to develop a maneuvering propulsor for unmanned undersea vehicles that is based on the pectoral fin of the bluegill sunfish. Wilbur and collaborators (Ayers et al. 2001) have designed a lamprey-based undulatory vehicle that takes advantage of the animal's manuverablity and energetic efficiency as they produce a reduced-wake signature.

1.2.4 Metrics of Propulsive Performance

Aquatic animals differ from typical engineering systems in their use of unsteady flow for locomotion. Traditional definitions of propulsive efficiency used to model these behaviors have not taken unsteady effects into account and are typically based on steady flow through propellers or rocket motors. Measurements of aquatic animals based on these quasi-steady metrics have suggested propulsive efficiencies over 80% when utilizing certain swimming kinematics. However, the mechanical efficiency of muscle-actuated biological propulsion has been found to be much lower, typically less than 20%. When designing and implementing a biologically inspired propulsive device, it is important to take into account the overall efficiency (η_o) of the system defined as the product of the mechanical (η_{mech}) and propulsive efficiency (η_{prop}) (Hill and Peterson 1992).

$$\eta_o = \eta_{mech} \times \eta_{prop} \tag{1.1}$$

The η_{mech}, is a measure of the efficiency of converting the energy input into mechanical power to drive the propulsion mechanism. For shaft power devices, the mechanical efficiency is defined by

$$\eta_{th} = \frac{P_s}{P_{in}}, \tag{1.2}$$

where P_s is shaft power and P_{in} is the heat energy or power input. The η_{prop} is a measure of the performance of the propulsion system and is the ratio of useful work to the mechanical energy produced in the fluid. The mechanical energy is the increase in kinetic energy of the fluid per unit time. The useful work is the product of thrust, T, and the speed of the vehicle relative to the surrounding fluid, U. The propulsive efficiency can be written as

$$\eta_{prop} = \frac{T\,U}{\dot{m}\left[(U_j^2 - U^2)/2\right]}, \tag{1.3}$$

where $\dot{m}$ is the mass flow rate through the propulsion system and U_j is the speed of the jet flow. Using conservation of momentum, the thrust for a steady jet can be approximated as $T = \dot{m}(U_j - U)$. Making the following substitution into equation (1.3), the propulsive efficiency simplifies to

$$\eta_{prop} = \frac{2}{1 + U_j/U}. \tag{1.4}$$

This result is the ideal (i.e., steady, inviscid) efficiency for a propeller and is otherwise known as the Froude efficiency, Glauert (1935). As a consequence of the steady flow assumption, schemes to enhance propulsive efficiency have focused on manipulating the mean velocity profiles upstream and aft of the propulsor. These efforts have included the use of coaxial contrarotating propellers (Hadler 1969), propellers with vane wheels (Grim 1980, Blaurock 1990), ducted propellers (Stipa 1931, Sachs and Burnell 1962), pre- and post-swirl devices (Narita et al. 1981, Grothues-Spork 1988), and flow-smoothing devices (Glover 1987). These strategies typically provide increases in propulsive efficiency of only a few percent, with a few reports of increases up to 25 percent (Breslin and Anderson 1996).

1.3 Objectives

The main objective of this research is to conduct an investigation allowing for a direct, experimental comparison between biological and engineering propulsion systems. For this study, an underwater vehicle was designed with the capability to produce either a steady or an unsteady jet for propulsion,

akin to a squid and jellyfish, while utilizing the same η_{mech}. Given that the system has the same η_{mech} for both modes of propulsion, the η_{prop} is related to the η_o as $\eta_o = C \times \eta_{prop}$, where the constant $C = \eta_{mech}$. This results leads to an accurate comparison of the system's total efficiency for both modes of propulsion. In other words, measuring and comparing the propulsive efficiency for both modes of propulsion is equivalent to conducting a comparison of the total efficiency. A second objective of the research is to demonstrate that it is sufficient but not necessary to mimic the geometry and kinematics of swimming animals to replicate their propulsive performance. Using the conventional method of propulsion of a propeller platform can be similarly effective provided that the vehicle is capable of producing similar wake dynamics as those of swimming animals. The last objective serves to gain an understanding of the wake dynamics responsible for the production of increased propulsive performance. How does additional impulse generation due to two classes of ambient fluid entrainment in vortex ring formation play a role in altering the propulsive performance in pulsed jet propulsion?

1.4 Thesis Breakdown

This thesis is divided into five main chapters with a chapter for conclusions and 5 appendices of supporting material. Chapter 1 provides the background and support for the research. Chapter 2 describes the methodology behind the design of the vehicle and provides a detailed description of its construction and operation. Chapter 3 describes the experimental techniques and procedures used to characterize the jet flow and used in the investigation of the propulsive performance of the vehicle. Chapter 4 describes the characterization of the jet flow and the investigation of the propulsive performance of the vehicle by obtaining a measurement of the Froude efficiency and the total hydrodynamic efficiency. Chapter 5 provides insight into potential sources that contribute to increased propulsive performance. The analysis demonstrates that the acceleration of two classes of ambient fluid can lead to an increase in propulsive performance. A model is developed to investigate how the increase in total fluid impulse relates to the propulsive efficiency. Results are summarized and recommendations for future work are given in chapter 6.

Chapter 2

Vehicle Design, Construction, and Operation

2.1 Introduction

This chapter describes the design of the vehicle and provides a detailed description of the construction and operation. Section 2.2 is broken up into three parts. Section 2.2.1 provides a breakdown of the vehicle into two categories: the vehicle structural components and the electrical components that are internal to the vehicle. Section 2.2.2 gives a detailed description of the mechanism that allows the vehicle to produce both a steady and unsteady jet with the same mechanical efficiency. The final section, section 2.2.3, outlines the operational components that are external to the vehicle.

2.2 Detailed Description of Vehicle Design and Construction

2.2.1 Vehicle Components

For this study, a self-propelled underwater vehicle was designed and developed capable of producing both a steady and unsteady jet while maintaining the same η_{mech}. The vehicle's physical attributes resemble that of a submarine.

2.2.1.1 Mechanical Components

The design and detailed drawings of the submarine parts were developed using the 3D CAD product design engineering software, SolidWorks. The manufacturing and construction of the submarine shell was performed by David Merriman of D and E Miniatures. The exterior structure of the submarine is composed of four main parts: water filled anterior cap, motor housing, fluid housing with attached hydrofoil and the fluid nozzle as illustrated in figure 2.1. Each part was made from a composite glass-reinforced plastic, and has a 0.13-inch wall thickness. When fully assembled, the submarine is 40.0 inches in length and 6.0 inches in nominal diameter. Figure 2.1 shows a schematic and image of the fully assembled vehicle that has been designed for this project.

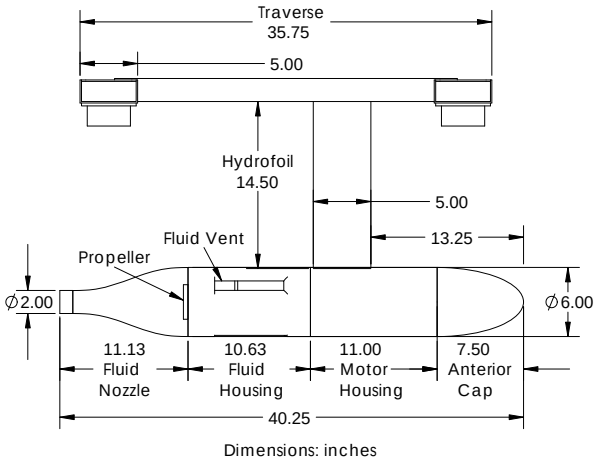

(a) SolidWorks drawing of vehicle components with attached traverse.

(b) Image of vehicle shown with length scale reference.

Figure 2.1. Schematic and image of the fully assembled vehicle.

The anterior cap of the submarine was designed to minimize frontal drag by using an elliptical shape. The cap has a cross-sectional diameter of 6.0 inches and an overall length of 7.5 inches. The submarine was designed to be neutrally buoyant, therefore, located on top of the cap is a button that once pressed allows water to enter and fill the cap. Figure 2.2(a) shows an image of the filling mechanism. The anterior cap of the submarine is attached to the motor housing of the submarine using 8 (6-32 thread, 5/16 inch length) equally spaced screws.

The motor housing component of the submarine is a watertight cylinder that contains the sub-

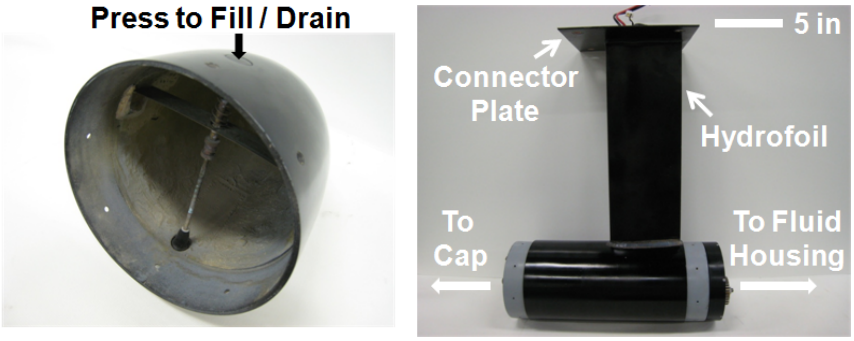

(a) Image of the filling/draining mechanism.

(b) Image of the submarine motor housing with attached hydrofoil and connector plate.

Figure 2.2. Image of the anterior cap and the motor housing of the vehicle.

marine motor and tachometer. The length of the motor housing is 11.0 inches and it is 6.0 inches in diameter. Fused to the body of the housing via epoxy and fiberglass is a hydrofoil. When assembled, the hydrofoil is positioned 0.25 inches away from the seam of the mating location between the motor and fluid housing. The hydrofoil provides the submarine with the stability to travel in a unidirectional path down the flume facility while providing a smaller wake disturbance in comparison to other geometries. The shape of the hydrofoil was inspired by a NACA 0024 airfoil. The hydrofoil has a 5.1-inch chord and is 14.5 inches in length. Its geometry was modified such that the thickness of the hydrofoil was twice that of the NACA 0024 airfoil. This increase in thickness provided increased strength and size to the hydrofoil, allowing for the passage of a steel cylindrical pipe. This increase in the thickness of the hydrofoil increases flow separation at high vehicle speeds (35 to 56 cm/s) but was necessary to provide structural strength to the vehicle. Analysis of jet dynamics was avoided in the area directly behind the hydrofoil. The pipe channels electrical wiring from the surface to the core of the submarine. The steel pipe was welded to a 0.4-inch-thick, 6.5-squared-inch steel plate. The steel connector plate mounts the submarine to a traverse. Figure 2.2(b) shows an image of the core of the submarine with attached hydrofoil and connector plate.

The fluid housing is attached to the backside of the motor housing using 8 (6-32 thread, 5/16 inch length) equally spaced screws. The fluid housing is 6.0 inches in diameter and 10.6 inches in length. Fluid has the ability to enter 3 equally spaced rectangular slots. The slots are 6.0 inches

long, 1.0 inch wide and are positioned axially in the center of the fluid housing. The slot areas were later modified to produce a pulsed jet with vortex ring formation as discussed in section 4.3. Figure 2.3(a) shows an image of the fluid housing.

After fluid enters the fluid housing, it passes through a propeller into the fluid nozzle. The propeller is situated at the intersection of the fluid housing and nozzle. It is a 3-inch, 7 skewed blade brass propeller (Ships n' Things, Manville, New Jersey). The final selection of the propeller was based on availability and evaluated performance. Various other propellers were tested but proved insufficient to provide the thrust necessary to propel the submarine. The final propeller is shown in figure 2.7.

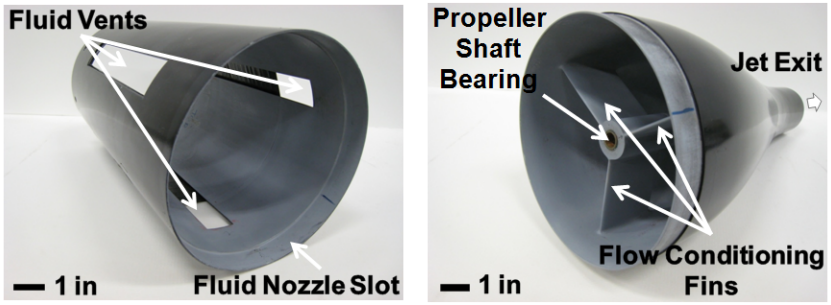

(a) Image of the fluid housing with visible partial blockage of two of the fluid slots.

(b) Image of the inside of the fluid nozzle component.

Figure 2.3. Upstream image of the fluid housing and the fluid nozzle components.

The fluid nozzle is press fit into the fluid housing. It is secured with electrical tape wrapped along the seam. The shape of the fluid nozzle is contracted from a diameter of 6 inches to a diameter of 2 inches using a 6th-order polynomial curve fit to provide smooth, attached flow at the exit of the nozzle. The length of the nozzle is 11.13 inches. The fluid nozzle also provides support to the propeller. Given that the propeller shaft extends slightly beyond the length of the fluid housing, this support is necessary to dampen vibrations induced by the propeller rotation. The end of the propeller shaft sits in a Oilite bearing that is supported by 3 vertical fins. See figure 2.3(b). These fins also provide flow conditioning by breaking up large eddies in the propeller wake.

The submarine is mounted to a traverse by securing four 7/16 inch screws to the center beam of the traverse. The traverse is an I-beam configuration manufactured from $2.0 \times 5.0 \times 0.125$ inch

anodized aluminum rectangular tubing. To protect the surface of the aluminum from oxidation, the parts were anodized. The total length of the traverse spans 35.75 inches and is 54 inches in width. Rectangular holes were cut as necessary along the members of the I-beam to minimize weight. The submarine must not only propel itself but also pull the traverse which rests on four low-friction roller-bearing pillow blocks (Lee Linear) which have a low rolling dynamic coefficient of friction, 0.004 on average, and low resistance to motion. Two of the pillow block bearings are rigidly fixed to the traverse using 4 screws (1/4-20 thread, 0.75 inch length) which connect to a 0.25-inch square plate and then into the traverse. The pillow block bearings on the opposing side are allowed to slide laterally. These two pillow blocks are connected with 4 (1/4-20 thread, 0.75-inch length) screws to a connector plate which is connected to the traverse by a pin which rests in a slot. In figure 2.1(b), the traverse and pillow blocks are partially visible on the top left of the image.

2.2.1.2 Internal Electrical Components

The submarine is powered by a 2 hp motor (AstroFlight Cobalt 60). It contains a superbox that allows for a 2.7 to 1 gear ratio. The voltage range for this motor is 24 to 36 V and supports a maximum continuous current of 35 A. The motor is mounted to an acrylic faceplate. This faceplate creates a watertight seal for the motor housing of the submarine. As the motor rotates, a tachometer (Monarch Instruments) that is mounted to the motor measures the motor rpm using a remote optical sensor (ROS), see figure 2.4(a). The sensor requires 3 to 15 VDC at 40 mA. The ROS is capable of detecting a reflected pulse from a reflective tape covered target at distances up to 36 inches. It produces a negative TTL pulse, from 5 to 0 V as it detects a reflection from the tape. A water detector (Watchdog) is included in the motor housing for safety reasons and is powered by a 9 V battery. The sensor is located at the bottom of the core and shown in figure 2.4(b). A continuous alarm sounds once water comes in contact with the sensor. The alarm is deactivated by allowing the sensor to dry or disconnecting power to the sensor.

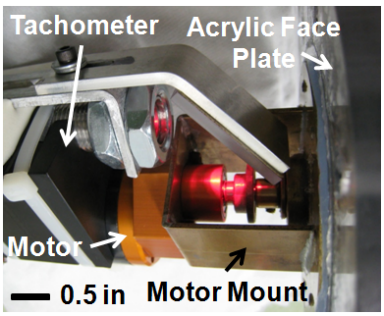

(a) Image of motor mount with attached tachometer.

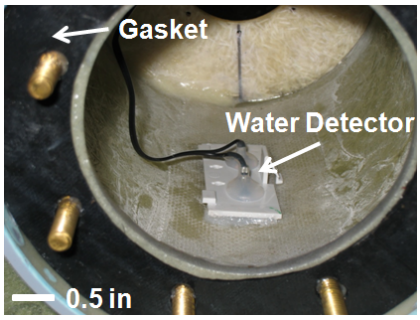

(b) Image of water detector mounted at the bottom of the core of the vehicle with the motor removed.

Figure 2.4. Images of electrical components internal to the vehicle.

2.2.2 Description of Jet Mechanism

The submarine is capable of producing both a steady and unsteady jet with the same η_{mech} by maintaining the same load on the motor in each case. Located inside of the fluid housing is a rotating cylindrical shell. Changing the geometry of this shell allows both modes of propulsion to be produced. These shells rotate through a series of gears (Stock Drive Products/Sterling Instruments) that are connected to the motor shaft. The rotation of the shell is geared down by a ratio of 5. The reduction of the rotational speed of the shell was limited by the size of the inner diameter of the fluid housing and the availability of gears. The gearing mechanism consists of 4 gears; a central gear which is directly connected to the motor shaft, 2 planatery gears, and one ring gear, see figure 2.5.

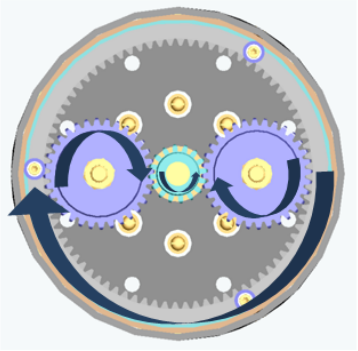

(a) Schematic illustrating gear rotation.

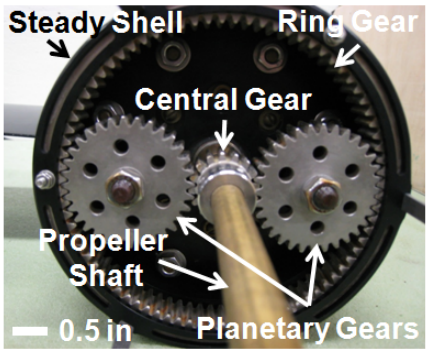

(b) Image of gearing mechanism used to generate both steady and unsteady jet propulsion.

Figure 2.5. Gearing mechanism used to generate both steady and unsteady jet propulsion.

The central gear and planatery gears are stainless steel, and the ring gear is composed of carbon steel. The surface of the ring gear was nickel plated to prevent oxidation. The bore diameter of the central gear was increased from 0.315 to 0.438 inches in order to fit the shaft diameter of the propeller. The two planatery gears are mounted to a face plate using a stainless steel shoulder screw (10 mm shoulder diameter, 25 mm shaft length, M8 thread) which is directly mounted to the motor housing by fastening eight 1/4-20 screws which pass through the face of the submarine core. These screws are permanently set in the core of the submarine with epoxy. The planetary gears were modified by drilling six 0.25-inch diameter through holes in a circle pattern and also cutting a pocket on the inner face of the gear to decrease gear weight. To decrease the friction of the rotating planetary gears, two $10 \times 22 \times 6$ mm shielded stainless steel ball bearings are used. One bearing is mounted on the inside of the face plate and the other is located in the pocket of the gear. The ring gear, which is driven by the planetary gears, is attached to the shell using three M3, 35 mm length socket head cap screws. A total of six $3 \times 10 \times 4$ mm shielded stainless steel bearings are used in supporting the shell rotation inside of the fluid housing. Three bearings are mounted on the ring using the three M3, 35 mm socket head cap screws. The remaining three are mounted on the opposite thin ring using three M3, 18 mm socket head cap screws. The bearings rotate in this ring as the shell rotates. Figure 2.8(a) shows two of the bearing that rotate in the ring along with one of the bearings that is mounted to the ring gear. The thin ring is held in place by fluid housing supports.

2.2.2.1 Unsteady Jet Configuration

The unsteadiness of the jet efflux is generated by the inner rotating cylindrical shell, or flow chopper, and is geared to the primary propeller and rotates between 0 and 13 Hz. Figure 2.6 illustrates the operation. In a pulsed jet configuration, the fluid inlets are periodically blocked by a cylindrical shell that rotates inside the hull of the vehicle. This periodic blockage of the flow inlets results in a pulsed flow at the nozzle outlet. The frequency and amplitude of the pulsing is controlled by the frequency of the inner shell rotation and by the fraction of the fluid inlets that are blocked by the

flow chopper. A small downstream portion of the fluid inlets, 1 inch by 11/16 inches cross-sectional area, remains open to avoid cavitation within the nozzle due to the transient pressure drop that occurs as the inlets are blocked.

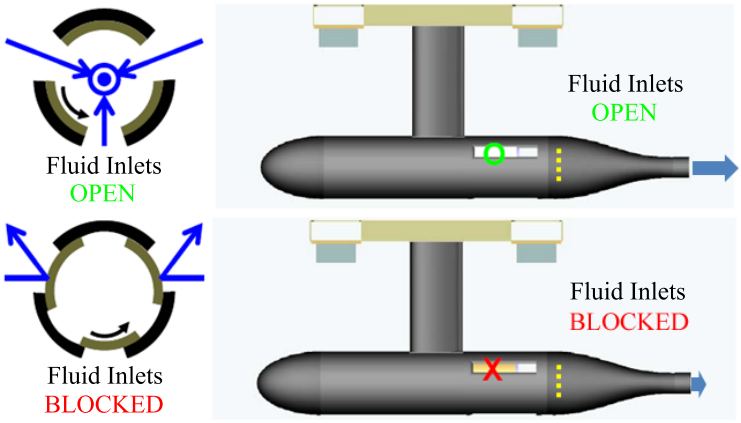

Figure 2.6. Principle of operation for pulsed jet configuration. Black arrows in left panels indicate inner shell rotation.

Figure 2.7 shows an upstream view of the unsteady rotating shell mounted inside the vehicle. The open and blocked orientations of the inner shell are shown in the left and right panels respectively. The planetary gear system, used to control the rotational speed of the shell relative to the rotation speed of the propeller, can be seen in the background. The always-open downstream portion of the fluid inlets is visible in the foreground. The unsteady shell shown in this figure was later redesigned to decrease the frequency of pulsing in order to produce a pulsed jet with vortex ring formation (section 4.3.1). The final design of the unsteady shell geometry was manufactured from a solid piece of aluminum, see figure 2.8(a). In this figure, the unsteady shell is attached to the ring gear. To maintain a constant moment of inertia, two stainless steel counterweights were placed in opposition to the fluid blocker.

2.2.2.2 Steady Jet Configuration

The only difference in the mechanical design of the steady and pulsed jet versions of the propulsion system is in the solidity of the inner rotating shell. The steady shell was designed to have the same moment of inertia of 4.59 kg cm^2 as the unsteady shell. The steady shell design consists of 5 parts;

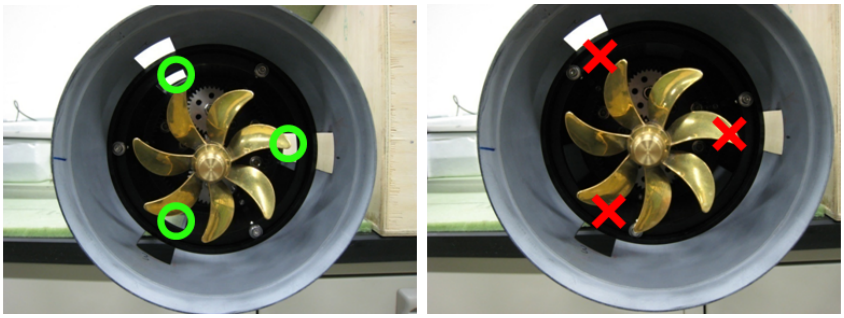

(a) Flow chopping mechanism in an open configuration as denoted by the green circles.

(b) Flow chopping mechanism in a closed configuration as indicated by the red x's, the secondary vents remain open.

Figure 2.7. Image of the upstream view of the unsteady rotating shell mounted inside the vehicle with the nozzle removed.

3 thin stainless steel ribs and 2 aluminum rings as shown in figure 2.8(b).

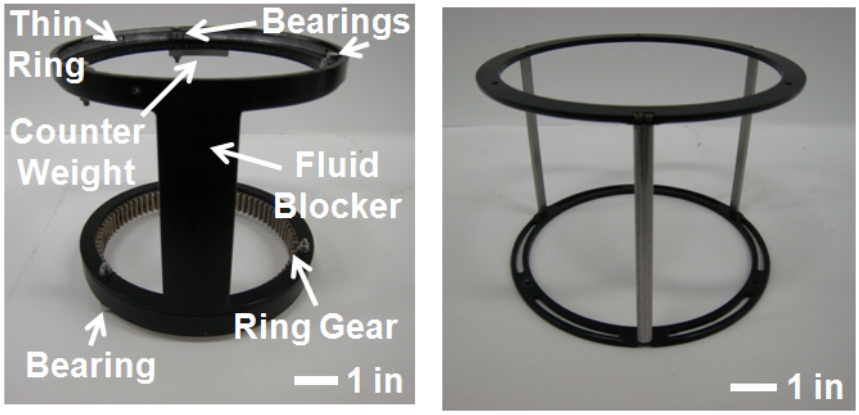

(a) Image of the inner rotating shell for the pulsed jet with attached ring gear.

(b) Image of the inner rotating shell for the steady jet.

Figure 2.8. Images of inner rotating shells for both pulsed jet and steady jet vehicle configurations.

This design feature is intentional to maintain identical mechanical efficiency for both steady and pulsed jet configurations. As shown in figure 2.9, the steady jet system uses a rotating inner shell whose blockage is negligible for any azimuthal position of the shell. The output jet efflux is nominally steady.

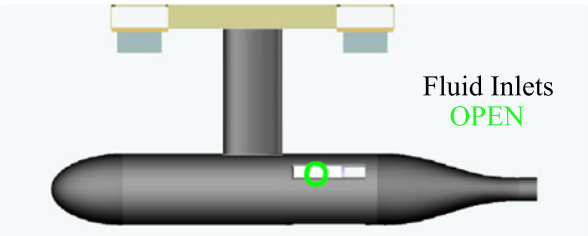

Figure 2.9. Principle of operation for steady jet configuration.

2.2.3 Vehicle Operation

The submarine throttle is controlled by a speed controller (Astro Flight Incorporated) connected to the motor. The voltage range for this controller is 7 to 60 V with a continuous current rating of 60 A. Power is transmitted to the speed controller through a 12-gauge, 25 m long power cable connected to the electrical box stationed on a work table in the center of the testing area. Provided that the electrical box is located in the center of the testing area, a 25 m long power cable is sufficient to allow the submarine to move down the 30 m long testing area. The motor current passes through a 0.01 Ω shunt placed in series on the negative voltage line and located within the electrical box. This shunt is used to measure system current. A power switch is located on the outside of the electrical box which allows opening and closing of the motor power circuit.

Initial experiments were conducted using three 12 V, 7 Ah rechargeable batteries. An Agilent 6674A power supply with a capability to supply 0–60 V at 0–35 A later replaced the batteries. As a safety precaution, a 35 A fuse was placed in series between the speed controller and power supply. Typically during self propulsion, the submarine draws 12 A at 37 V. Communication to the speed controller is achieved through an RF receiver (Polk's Hobby Seeker 6). The wiring diagram is shown in figure 2.10.

The Seeker 6 operates at a 75 MHz frequency and is a six-channel receiver that can be used with any FM transmitter using any of the 50 channels within the 75 MHz aircraft frequency. Only one channel is used to control the throttle of the vehicle. The FM transmitter used in conjunction with the receiver is a Polk's Hobby Tracker III.

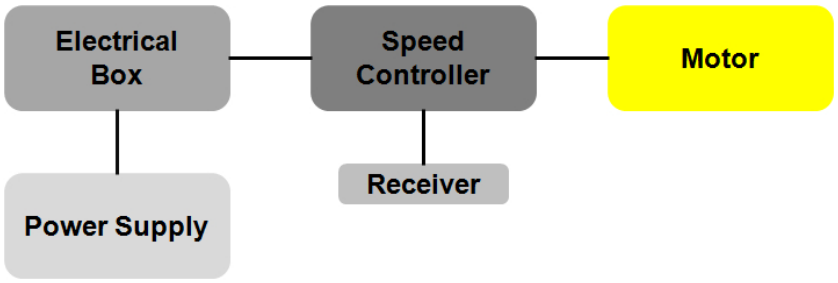

Figure 2.10. Schematic of electrical wiring necessary for the operation of the vehicle.

Chapter 3

Experimental Techniques and Procedures

3.1 Introduction

This chapter describes the experimental techniques and procedures used to characterize the jet flow and the propulsive performance of the vehicle. Section 3.2 describes the features of the facility where the experiments were conducted. The remainder of the chapter is divided into two main sections. Section 3.3 describes the techniques used for experiments in which the vehicle was held in a stationary position and section 3.4 describes the experimental techniques used during the measurements of self-propulsion. Data acquisition during the stationary experiments was relatively simple, as described in section 3.3.1. Two techniques were used to characterize the jet flow. Digital particle image velocimetry is discussed in section 3.3.2 and planar laser-induced fluorescence is described in section 3.3.3. The data acquisition in the self-propelled experiments is described in section 3.4.1. As the vehicle propels down the facility, a motorized traverse was designed to follow the vehicle at a preset distance using a control system as discussed in section 3.4.3. Two experimental techniques were used for the investigation of propulsive performance. Laser Doppler velocimetry was used to obtain measurements of the jet flow as described in section 3.4.4 and drag measurements were used in the estimation of the total hydrodynamic efficiency. The details for the drag experimental procedure are found in section 3.4.5.

3.2 Test Facility

The experiments were conducted in a 40 m tilting water tunnel and wave generation facility in the Keck Laboratory at the California Institute of Technology. The tunnel has a cross-sectional area of 110 cm in width and 60 cm in height. Figure 3.1(a) is an image of the upstream view of the facility. The submarine was designed to be positioned in the center of the tunnel. The long length of the tunnel allowed sufficient run time for the self-propulsion experiments. This facility is equipped with a controllable motorized traverse that translates along the flume rails. A schematic of the traverse can be viewed in figure 3.2. The traverse was used to hold necessary equipment for experiments. In addition to controlling speed, the direction of translation can also be set by a control panel in the center of the facility. Software was developed to control the speed of the motorized traverse via a computer (section 3.4.3) and record the position and speed of the motorized traverse that is displayed on the control panel (section 3.4.3). See figure 3.1(b) for an image of the control panel.

(a) Image of the upstream view of the 40 m water tunnel facility.

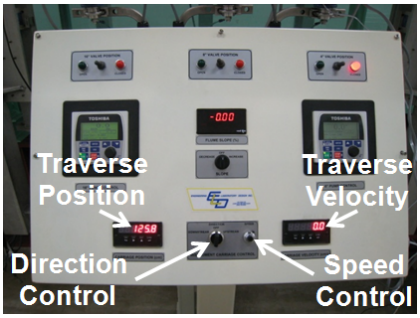

(b) Image of the panel used to control the direction and speed of the motorized traverse.

Figure 3.1. Images of facility and control panel for motorized traverse.

3.3 Measurement Techniques and Applications (Stationary Configuration)

3.3.1 Data-Acquisition System

The initial voltage supplied to the vehicle by a battery was measured using a digital multimeter (Fluke). The current flow into the system was measured by placing a current clamp (Fluke) on one of the power leads to the motor batteries. The output of the current clamp was connected to a digital multimeter and the average display value was recorded. The usable current range of the current clamp is 0.5 to 1000 amps. The accuracy of the device is 2.0% of the reading +/- 0.5 amps. The motor speed was measured by connecting the output from the tachometer to a hand-held tachometer reader (Monarch). This device allowed the motor speed to be displayed and the average value to be recorded.

3.3.2 Digital Particle Image Velocimetry Measurements

Digital particle image velocimetry (DPIV) is a technique for obtaining flow field measurements (Willert and Gharib 1991). A thin laser sheet illuminates a particle-seeded flow. A camera, perpendicular to the laser sheet, records images as the particles are illuminated. By cross-correlating intensity fields in a subsection of two successive images, an average displacement of the particles in the sampling window can be calculated. This procedure is repeated across the image area, generating the flow displacement field between the time at which the two images were taken. Dividing the flow displacement field by the time difference between the two images yields the velocity field of the flow.

Particles used to seed the flow for experiments were neutrally buoyant, silver-coated, hollow glass spheres with a 13 μm diameter and density of 1.6 g/cm^3 (Potters Industries). Plastic barriers were used to confine a 30 m section, eliminating the need to fill the entire tunnel with particles. The particles were illuminated by two Nd:YAG lasers (New Wave) with a power rating of 30 mJ per pulse at a 532 nm wavelength. The laser beam is collimated by a cylindrical lens and then reflected

by a mirror to illuminate a cross-section of the jet. See figure 3.2.

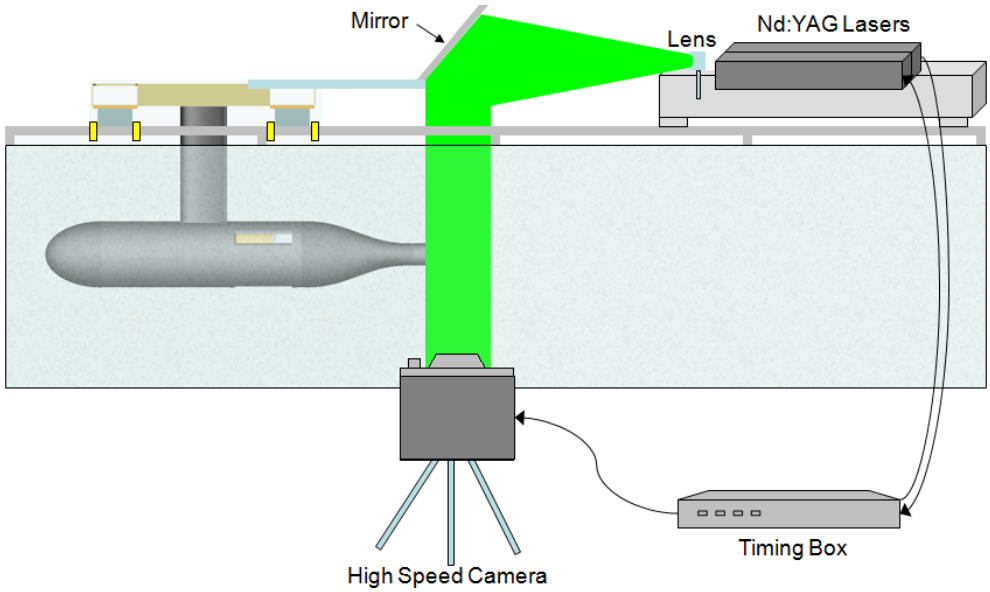

Figure 3.2. Schematic of DPIV setup for the jet flow of the vehicle in a stationary configuration.

The laser and optics are mounted in a stationary position on the motorized traverse. Since the pulsing frequency of the lasers is fixed at 15 Hz, one laser is pulsed at preset time delay to allow for greater measurement resolution. A schematic diagram of the laser pulsing is shown in figure 3.3. One laser is used as a master and sends a +5 V TTL pulse to a custom timing box when the Q-switch laser is energized. The timing box then sends a +5 V TTL pulse to trigger the second laser and camera at preset time delays. Varying the time delay to the second laser is used to set the timing between images. A Photron high speed camera is set to random reset trigger mode with a frame speed of 60 fps and a frame size of 1024×1024 pixels. The time difference between images was varied from 5.31 ms to 21.17 ms. Either a 60 mm or 105 mm lens was used with the camera depending on the field of view desired.

After postprocessing images from initial experiments, many errant vectors resulted. This error was attributed to particles moving in and out of the laser sheet. Honeycomb was placed in the exit of the jet nozzle to remove swirl from the propeller. The honeycomb was 2.0 inches in length and 2.0 inches in diameter, with a 0.125 inch diameter cell size. The honeycomb increased the pressure loss in the nozzle leading to significant thrust reduction. For this reason, it was removed during

experiments involving self-propulsion.

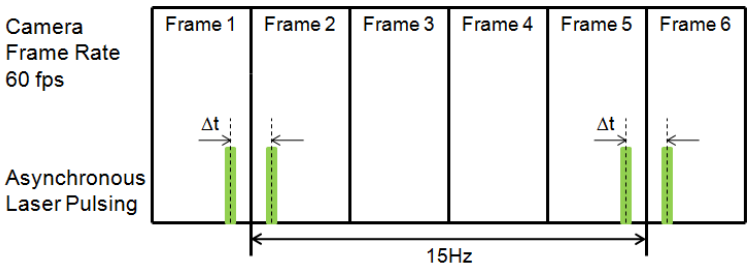

Figure 3.3. Schematic diagram of camera frame rate and laser pulsing.

Processing of the DPIV images was accomplished using an in-house developed code. Generally two approaches were taken depending on the field of view. For the steady jet results, shown in section 4.3.1, the 60 mm lens was used. Postprocessing of this data used a 32×32 pixel sampling window and a 16×16 step size. These parameters produced accurate vector fields with few or no errant vectors per image. For the unsteady shell geometries, a 105 mm lens was used to increase spatial resolution. This field of view encompassed only half the jet diameter. For these sets of images, a sampling window of 64×64 pixels with a 32×32 step size was used. Once it was evident that the unsteady shell geometry was producing fluid roll up, the 60 mm lens was used to verify symmetric fluid roll up otherwise known as vortex ring formation.

3.3.3 Planar Laser-Induced Fluorescence Measurements

Planar laser-induced fluorescence (PLIF) is a technique widely used for flow visualization and for quantitative measurements (Smits and Lim 2000). PLIF was used for flow visualization for the results shown in section 4.3.2. A 60 mm lens was used for imaging, providing a field of view with the spatial resolution of 3 jet diameters in the axial direction and 1.3 jet diameters in radial direction. One difference between DPIV and PLIF is in the medium that is used for illumination. In PLIF, the fluid medium is either comprised of fluorescent material or can be seeded with a fluorescent particulate substance. Rhodamine 6G, a fluorescent dye with maximum absorption wavelength of 530 nm was injected in the fluid housing by a syringe through tygon tubing. Dye was continuously injected imposing negligible momentum to fluid passing through the submarine inlet until sufficient data was

captured. In addition to the Rhodamine dye, the particles present from the DPIV experiments also absorbed the laser light. A deep golden amber filter (Lee Filter), allowing light transmission from 550 to 700 nm, was placed over the camera lens to block out the DPIV particle emission but accept the rhodamine dye fluorescence.

3.4 Measurement Techniques and Applications (Self-Propelled Configuration)

3.4.1 Data Acquisition System

An electrical box provides signal conditioning, sensor power, and submarine power switching. The electrical box is composed of an aluminum housing containing a bread board, sensor power supply and power shunt resistor. Submarine motor power interconnects use 12-gauge wire, while sensor power or data interconnects use 26-gauge wire. The electrical box provides two 9-pin D-subminiature connections. One is an input for submarine telemetry from the submarine and related sensors, while the second is an output of submarine telemetry to the data acquisition box. The electrical box also provides two screw-type Molex connectors. One is an input from the submarine motor power supply, while the second is the submarine motor power output to the submarine. The sensor power supply cord is also routed to the electrical box.

Due to voltage input limitations of +/- 10 V on the data acquisition box, it is necessary to condition the submarine motor voltage measurement before supplying the signal to the data acquisition box. It is also not possible to measure the voltage across the submarine motor directly as this leads to a large common-mode voltage in the measured signal. This is an artifact of the submarine speed controller design. To avoid the common-mode component, the voltage is measured independently, with respect to power supply ground, at the positive and negative side of the submarine motor. The differences between these two measurements is computed in software and results in the effective voltage across the submarine motor. Even with this scheme, it is still necessary to voltage divide the measured signals down to within input limits of the data acquisition box. This is accomplished

through two similar voltage dividing circuits mounted on the electrical box breadboard. Each circuit consists of two 1/4 watt, 5% tolerance resistors of values 15 and 50 KΩ which are connected in series. The circuit output voltage is read across the smaller resistor giving a circuit gain of 0.23 +/- 0.02. This provides the capability of reading submarine motor voltages of over 40V based on data acquisition box input limits. See Appendix C for a wiring diagram of the electrical box.

The electrical box powers the submarine tachometer and traverse distance sensor. These devices require 5 V power. This is provided by the internal Acopian power supply. The Acopian power supply is rated at 0.5 A and packaged in a fully enclosed plastic case with screw-type connectors. It requires standard 110 VAC facility power via a three-prong power plug.

A thermal breaker switch mounted to the surface of the electrical box serves not only as an on-off switch for submarine motor power but also as a safety device. The breaker is rated for a current of 35 A. In addition, the negative submarine motor power line is routed to an internal 0.01 Ω shunt resistor. The voltage drop across the shunt resistor is used to calculate the submarine motor power supply current. The shunt resistor is capable of dissipating the heat generated by the submarine motor current through a built-in heat sink as well as the electrical box housing.

Submarine and sensor telemetry, except for the submarine motor current, is routed via the electrical box to a National Instruments multifunction data acquisition box. The data acquisition box is responsible for sampling and digitizing telemetry voltages for use in software. It also generates the motorized traverse drive signal discussed in section 3.4.3. The data acquisition box analog inputs and outputs operate on 0 to 10 V signals. While the data acquisition box is capable of measuring an aggregate 250K samples per second for all channels, software processing restricts the sampling rate to approximately 400 Hz.

Submarine motor current is measured via a current clamp (Fluke). The current clamp is attached to the negative line of the submarine power cable between the submarine and the speed controller. This location was chosen in order to avoid including the speed controller's internal current draw in the submarine motor current measurement. The current clamp produces a 1 mV per current amp signal +/- 2.0% of the reading +/- 0.5 A. It is zeroed prior to submarine power on via its adjustment

knob.

In order to capture the current clamp signal, it was necessary to use a device with a greater sampling rate than provided by the data acquisition box. The submarine speed controller introduces high-frequency components in the submarine motor current due to its voltage chopping mechanism. These high frequency components would lead to aliasing of the signal when measured using the data acquisition box. The Data Physics SignalCalc ACE dynamic signal analyzer was used for this task as it provides a 204.8 KHz sample rate and 24-bit measurement resolution. The signal analyzer consists of a portable, USB powered measurement device, known as Quattro, and a data analysis software suite. A software option was purchased that allows continuous logging of measurements to disk.

3.4.2 Data Acquisition Software

The main telemetry application is the Submarine data acquisition (DAQ). The Submarine DAQ is responsible for the collection, calibration and logging of submarine telemetry as well as the transmission of the motorized traverse control drive signal. This software was implemented in LabVIEW 8.5 on a Windows XP platform and consists of a single top level virtual instrument, or VI, and two sub-VIs. One script contains the application's state machine. Another is used to apply a calibration curve to the raw distance sensor output to convert from volts to centimeters. A third applies a linear moving average to the power supply current, motor voltage, and distance sensor signals to filter out high frequency noise.

The Submarine DAQ user interface is broken down into four areas as shown in figure 3.4. The Telemetry area displays the telemetry sample rate as well as charts submarine telemetry including power supply current, submarine motor voltage, the submarine tachometer output and the distance sensor output. The log area allows the enabling and disabling of the telemetry logging function as well as the location and name of the current log file. The Analog Output area displays and allows the enabling or disabling of the motorized traverse drive signal. Finally a Start button situated in the lower-right corner is used to start the application.

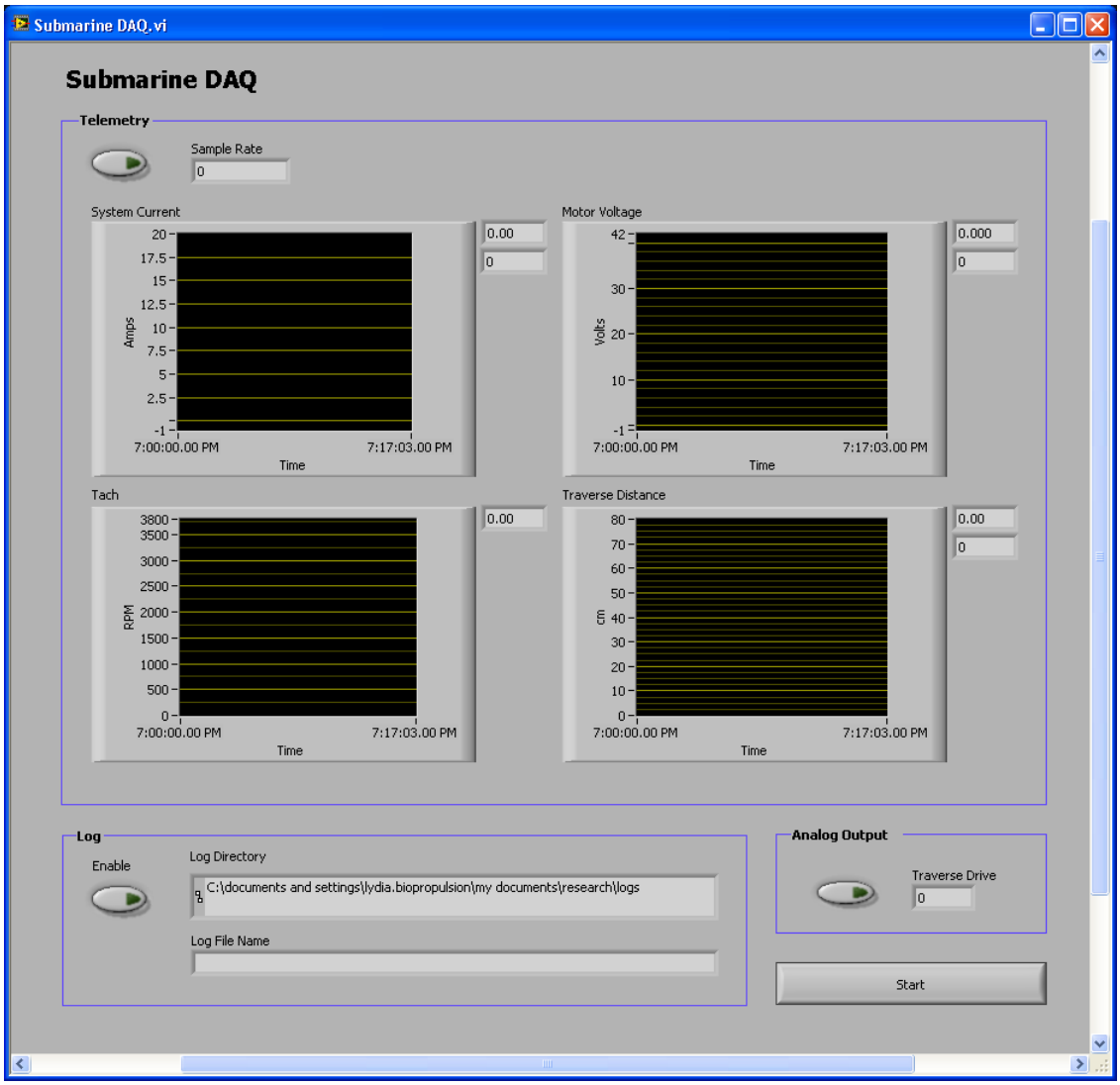

Figure 3.4. Screenshot of Submarine DAQ user interface.

The DAQ VI design consists of a single state machine depicted in the flow chart in Appendix A. Execution begins at the Initialize state. Here the application state is reset and user interface elements are populated with default values. Execution then continues to a wait state. In this state the user interface is monitored until the user clicks on the Start button. Once the Start button is selected, the state machine moves into its main control loop.

The first state in the Submarine DAQ main control loop checks if the user has selected the Stop button. If this is not the case, the control flows to the Measure state. In the Measure state, each of the signals that are connected to the data acquisition box is sampled. The measured signals are

then calibrated in the Calibrate state. Here each measured analog voltage is converted into the desired engineering units. For voltage or current measurements, this is a linear conversion with a single multiplying value. For the distance sensor output, a polynomial calibration curve is applied to convert the signal into centimeters. The tachometer output is a special case as it is a digital signal. The tachometer outputs a square wave whose frequency is proportional to the rotation speed of the motor shaft. In order to derive the signals frequency, the signal is processed using a power spectrum. The peak value of this power spectrum corresponds to the signal's digital frequency. This frequency is in turn used to derive the rotation speed of the motor shaft. At this point, the distance sensor output is also transmitted to the motorized traverse control software via a shared variable. The next state is the Control state. Here a motorized traverse drive value is received from the traverse control software. If enabled, the motorized traverse drive value is output from the data acquisition box. The next two states, Log and Display, perform the described operations. In the event that a log file is not already open upon entering the Log state, the OpenLog state is called which opens a new log file. Execution then moves back to the beginning of the main control loop. If at this point, the user has selected the Stop button, control continues to the Stop state.

The Stop state is responsible for closing an open log file if it exists. Upon completion of this state, the Submarine DAQ software returns to the Wait state where it will remain idle until the user has once again selected the Start button. The Submarine DAQ software produces TDMS formatted binary log files. This is an NI controlled format. This format was chosen as opposed to ASCII text logs as it reduces CPU utilization during logging operations and produces smaller file sizes. The TDMS files may be read from LabVIEW using built in VIs or optionally imported into Excel via an Excel add-in available from the NI website.

3.4.2.1 Motorized Traverse Telemetry

Motorized traverse position and velocity are provided from the motorized traverse control panel over an RS-232 serial interface with an RJ11 connector. The interface protocol uses a 9600 baud rate, eight bit bytes, one stop bit and no parity. To simplify connection to modern workstations, an

RS-232 to USB converter is used for each data channel. This allows direct connection to a computer USB port. The motorized traverse decimal measurements are encoded as ASCII text with carriage return delimiters and transmitted consecutively over the serial interface.

The Traverse Monitor software reads, displays and logs the motorized traverse position and velocity. The Traverse Monitor was implemented in Microsoft Visual C++ 2008 on a Windows XP platform. It connects to one or two serial ports over which the motorized traverse telemetry is received. An initialization file is required as input to the application and one or more log files are produced if logging is enabled.

The Traverse Monitor user interface contains a Telemetry and Options section as shown in figure 3.5. The Telemetry section displays the current motorized traverse position and velocity. The Options section allows the position or velocity channel to be disabled if one is not being used and also enables logging. The bottom of the user interface has a Start and Stop button. The user must select the desired options before selecting the Start button. The Stop button is only made available once the application has started.

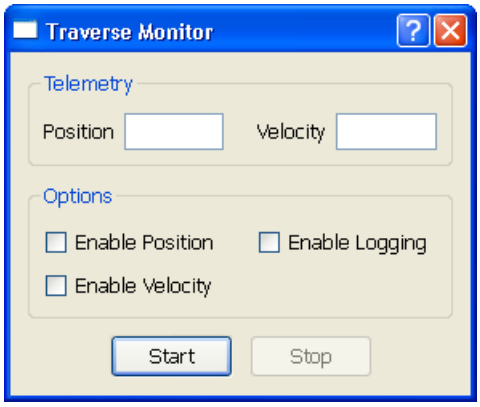

Figure 3.5. Screenshot of Traverse Monitor user interface.

The Traverse Monitor begins execution by reading in the initialization file. The initialization file contains serial port identifiers, display and logging options. Once the initialization file is read, a log file is opened if necessary. Logs contain time stamped measurements in an ASCII text, comma-delimited format. One or two threads are then started depending on whether position, velocity or both channels are enabled. Each thread opens its corresponding serial port and moves into a loop.

The first operation in the loop is to check if the user has stopped the application. If this is not the case, ASCII text data is read from the serial port. This data is then appended to a buffer. The buffer is subsequently searched for stream delimiters which denote the end of a complete measurement. If a delimiter is found, the measurement is extracted, logged and displayed. This sequence of steps continues indefinitely until the user stops the application. The final operation of each thread after the Stop button has been selected is the closing of its corresponding serial port.

3.4.2.2 Distance Sensor Description and Calibration

A wide angle distance sensor (Sharp) measured the linear distance between the submarine traverse and the motorized traverse. The measurement of this distance is required to control the motorized traverse drive as described in section 3.4.3 and is used indirectly to calculate the submarine velocity. The proximity detector is a optoelectronic device that emits an infrared beam and utilizes the reflection from the detected target to produce a nonlinear voltage output with respect to distance. The operational range of the sensor is between 20 and 150 cm over a 25° field of view. The response time of the device is 16.5 ms. The sensor required a supply voltage, V_{cc} , of +5 V, which was delivered through a power line embedded in the 50 ft power cable that connects to the electrical box sensor power supply. Further details about the electrical box can be found in section 3.4.1. In order to filter distance sensor power, a bypass capacitor of 100 μF was inserted between V_{cc} and ground.

The proximity sensor is 55 mm in length, 20 mm in height, and 18 mm in depth. The sensor was screwed into an aluminum holder that was designed for the device. The holder was clamped in place to the submarine traverse and positioned such that the infrared beam would strike a flat white piece of cardboard that was taped to the motorized traverse.

The distance sensor was calibrated by keeping the submarine traverse fixed and moving the motorized traverse by 1 cm increments. The change in distance of the motorized traverse was recorded using the facility control panel display. The voltage output from the sensor was sent to the National Instruments data acquisition box through a serial cable and was recorded by the Submarine DAQ software (3.4.1). The distance sensor output was recorded from a distance range of 16 +/- 1

cm to 140 +/- 1 cm. A 6th-order polynomial equation was fit to the data. See figure 3.6.

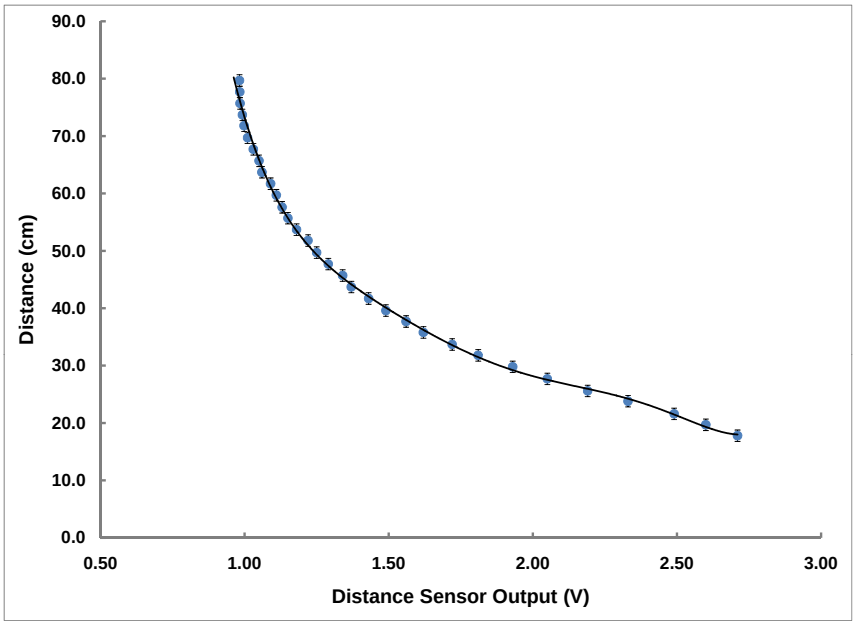

Figure 3.6. Plot of distance sensor calibration.

The relationship between distance and output voltage is nonlinear. There is a greater change or sensitivity in output at smaller distances. As the distance increases past 60 cm, the sensitivity is greatly reduced. Thus the motorized traverse was set to track the submarine traverse at a fixed distance of 40 cm.

3.4.3 System Control and Automation

The motorized traverse control panel accepts an analog control signal. The signal is output from the data acquisition box via 26 gauge wire and connected to the motorized traverse control panel via screw terminals. The motorized traverse control panel accepts a 0 to 10 V signal with 0 V halting the motorized traverse and 10 V accelerating the motorized traverse to maximum speed.

The Traverse Controller was implemented using LabVIEW 8.5. It is responsible for controlling the motorized traverse drive such that the motorized traverse tracks the submarine traverse at a

user specified distance. To accomplish this, the Traverse Controller uses the proportional-integral or PI control loop feedback mechanism. This application is composed of two VIs. The first VI implements the application's state machine as depicted in the flow chart in Appendix B. The second VI implements the PI control feedback mechanism.

The traverse controller user interface displays the PI algorithm parameters, the current distance sensor reading, the target motorized traverse to submarine traverse distance and charts the motorized traverse drive signal as shown in figure 3.7. Two buttons allow overriding of the motorized traverse drive value. The "Fixed Speed" button sets the motorized traverse drive signal to 2.5 V. This is a safe, moderate speed useful when relocating the motorized traverse along the water tunnel to prepare for an experiment. The "Stop Traverse" button sets the motorized traverse drive signal to 0 V and effectively stops the motorized traverse. The Stop button is used to shut down the application.

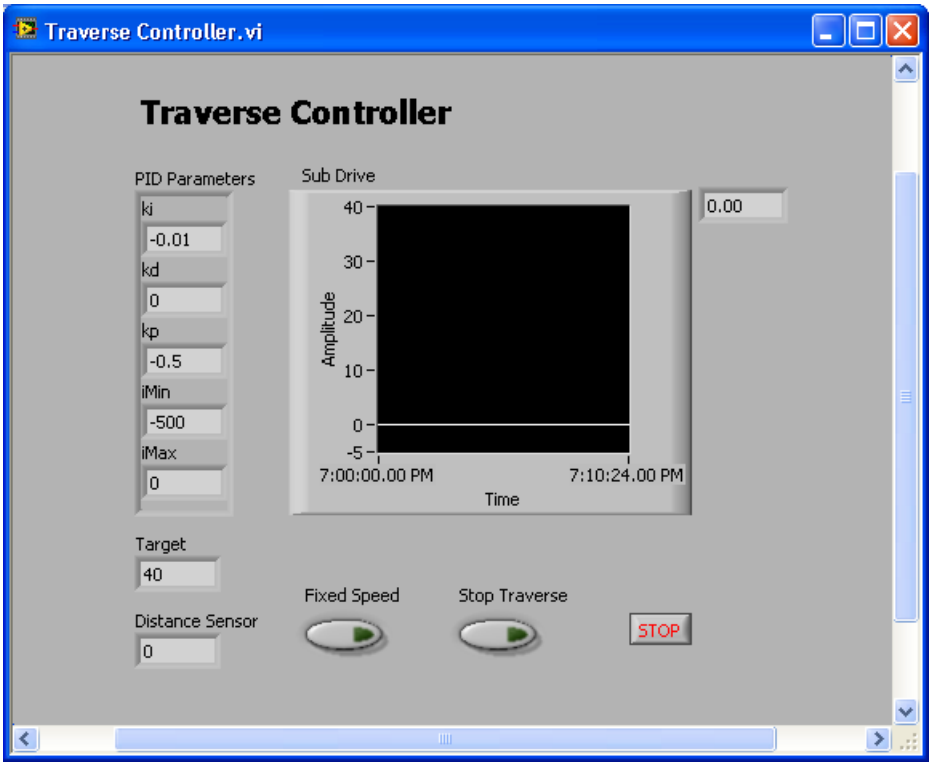

Figure 3.7. Screenshot of the Traverse Controller user interface.

The traverse controller is implemented using a state machine of three states. This application starts in the Initialize state where the PI control state is initialized. The next state is Run. This

state applies the PI control algorithm. First the current distance sensor value is received from the Submarine DAQ via a shared variable. This value is then fed into the PI algorithm. The PI algorithm output is limit checked into the valid motorized traverse drive signal range of 0 to 10 V. This value is then transmitted back to the Submarine DAQ via a second shared variable. The final state, Quit, is only executed if the user selects the Stop button. The state machine is halted and the application shuts down if this state is called. The PI algorithm uses the following internal equations:

$$SP - PV = e, \tag{3.1}$$

$$e \times K_p = P_{out}, \tag{3.2}$$

$$e + I_{state_1} = I_{state_2}, \tag{3.3}$$

$$I_{state_2} \times K_i = I_{out}, \tag{3.4}$$

$$P_{out} + I_{out} = MV, \tag{3.5}$$

where SP is the setpoint or, in this case, the desired tracking distance between the motorized traverse and the submarine traverse. PV is the processed variable or, in this case, the distance between the motorized traverse and the submarine traverse as measured by the distance sensor. The difference between these two values produces the error, e. The error multiplied by the proportional coefficient, K_p, leads to the proportional term, P_{out}. The error added to the integral state, I_{state_1}, produces the new integral state, I_{state_2}. This value is limit checked to lie within I_{min} to I_{max} inclusive to prevent the integral state from attaining values of extremely large magnitude. In the next iteration of the control algorithm, I_{state_2} will be used in place of I_{state_1}. The new integral state multiplied

Table 3.1. PI feedback control parameters

K_p	-0.5
K_i	-0.01
I_{max}	0
I_{min}	-500
SP	40

by the integral coefficient, K_i, produces the integral term, I_{out}. Adding P_{out} to I_{out} produces the manipulated variable MV or, in this case, the motorized traverse drive. Table 3.1 summarizes the PI parameters used.

3.4.4 LDV Measurements

Laser Doppler velocimetry (LDV) is a single point optical measuring technique which enables the velocity of seeded particles conveyed by a fluid flow to be measured in an unintrusive manner and is used to measure the velocity profile of the jet during self-propulsion. This technique was first reported by Yeh and Cummins (1964). See also Albrecht et al. (2003).

The LDV system consists of highly coherent light split into 2 beams and sent through a transmitter which crosses the beam in the probe volume to create a fixed interference pattern. As particles travel through the probe volume, they reflect light into a receiver when it crosses a region of constructive interference.

The tunnel was seeded with 13 μm diameter silver-coated glass hollow spheres to increase the number of particles that pass through the probe volume. Optics in the receiver allow the reflected light to focus onto an active area of an ultrafast photodiode. As seen by the photodetector, the light signal is a sinusoid modified by a Gaussian envelope. The sinusoid is isolated by a band-pass frequency filter. The frequency, f, of the sinusoid is typically measured using a Fast Fourier Transform. Since the fringe spacing in the interference pattern is known from calibration, thus, the speed of the particle can be calculated as follows:

$$Speed = fringe\ spacing \times f. \tag{3.6}$$

A one-component miniature laser Doppler velocimeter system (Measurement Science Enterprise miniLDV) was used in the experiments. The miniLDV is able to capture velocity measurements in the range of 1 to 300 m/s. The repeatability uncertainty is 0.1% with a typical accuracy of 99.7%. The probe must be rotated to measure multiple components of velocity.

An aluminum probe strut was designed to mount the miniLDV in a probe holder as shown in figure 3.8. The probe strut was attached to a 100 mm translational stage, thus allowing the miniLDV to translate in the vertical direction. The vertical stage was then mounted to a second 100 mm stage through a 90^o bracket plate. The second traverse allowed for translation of the probe in the horizontal direction. Software provided by Measurement Science Enterprise allowed for control of the motorized stages. The horizontal stage was attached to the traverse of the vehicle using eight 8-32 screws. The miniLDV probe volume was situated 0.5 inches away from the jet exit, or 0.25 jet diameters downstream. The probe volume was aligned so that the origin was referenced from the center of the jet.

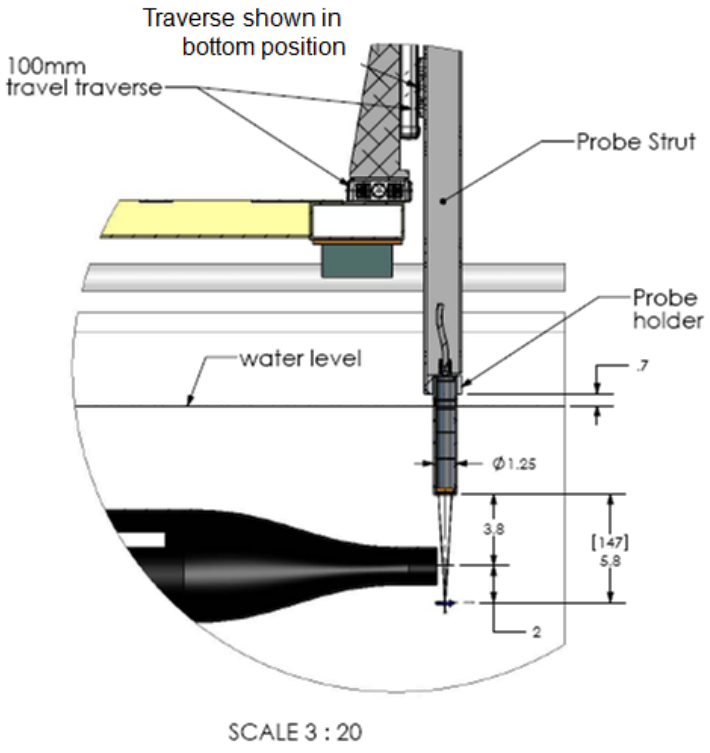

Figure 3.8. Schematic of LDV assembly mounted to the traverse of the vehicle.

The miniLDV system consists of the miniLDV probe, Processing Engine, and the 1D Burst Processor Acquisition Manager software package. The Processing Engine combines driver electronics, a band-pass filter, and a PCI acquisition card into one device, providing a USB 2.0 connection to the host computer and the Burst Processor Acquisition Manager software. The Burst Processor software collects data, moves the probe using the electronic traverses and presents flow statistics.

In initial propulsive efficiency experiments, a prototype of the modeled probe was used. This model was not capable of supporting a digital band-pass filter, so an analog band-pass filter was used in conjunction with the processing engine. Depending on the jet speed, the high-pass and low-pass filter settings were manually adjusted. For the self-propulsion experiments, the Doppler frequency of the jet ranged from 160 to 225 kHz. Within this speed range, the high-pass filter was set to 75 kHz and the low-pass filter was set to 100 kHz. The signal was amplified by adjusting the gain to a value of 20, and the minimal acceptable signal-to-noise ratio was set to a value of 3. The fringe spacing of this probe was 8.56 μm.

The second propulsive efficiency studies, along with the entrainment studies, were conducted using a later model of the miniLDV with a fringe spacing of 5.42 μm. The Processing Engine for this probe included the built-in digital filter. The following parameters were set for data acquisition using the Burst Processor Acquisition software: decimation, number of fast Fourier transform (FFT) points, threshold, minimum speed, maximum speed, minimum signal-to-noise ratio, and signal width. These parameters were adjusted depending on the speed of the fluid flow and which component of velocity was being measured. The decimation parameter adjusts the equivalent digitization rate of the hardware. The analog-to-digital converter hardware has a maximum digitization rate of 25 MHz. For lower frequency signals, a higher decimation parameter was used. The Doppler frequency of the signal is obtained by performing a FFT of the signal. As the number of FFT points increases there is a corresponding increase in the resolution of the results. Typically this was set to a value of 1024 or 512. The threshold parameter determines the processor signal trigger and was set slightly above the noise level. The minimal acceptable signal-to-noise ratio was set to a value of 4 for all experiments. Setting the signal width parameter allows for processing optimization of the entire

Doppler burst and was set to a value of "typical."

For LDV experiments, the water tunnel was seeded with neutrally buoyant, silver-coated hollow glass spheres with a 13 μm diameter and density of 1.6 g/cm^3 (Potters Industries) to increase the number of particles passing through the probe volume, hence increasing the data acquisition rate. Plastic barriers were used to confine the test section to 30 m in length, thus reducing the need to fill the entire tunnel with particles. The Processing Engine was mounted on the motorized traverse and was connected via USB to a computer located on the traverse. The Burst Processor software parameters were set by a remote connection from the water tunnel computer. The water tunnel computer was used to run the LabVIEW data acquisition software in conjunction with the traverse controller software.

Temporal data of the speed at the jet center located 0.25 jet diameters downstream was obtained using LDV. The Fast Fourier Transform (FFT) was calculated to determine if the pulsing frequency was distinguishable at various motor speeds for the pulsed jet configuration. Figure 3.9 shows the FFT results obtained for two different motor speeds. The predominant frequency determined through FFT at the lower motor speed was 2.36 Hz. The pulsing frequency as determined from the measurement of the rotational speed of the inner rotating shell was 2.3 +/- 0.1 Hz. The predominant frequency obtained through FFT of the jet speed correlates to the pulsing frequency at low motor speeds. As the motor speed increases, the predominant frequency as determined from the FFT is not as clearly defined. There appears to be a maximum peak at 8.4 Hz. Other peaks are present at 5.3, 6.4 and 9.9 Hz which are near in amplitude to the maximum peak. The pulsing frequency as determined from the measurement of the rotational speed of the inner rotating shell was 9.3 +/- 0.1 Hz, which is close to the predominant frequency. The pulsing frequency may be more clearly evident in the jet wake by modifying the location of the LDV probe volume to measure other axial and radial positions. It was shown in figure 4.6 that pulsing was clearly evident outside the diameter of the jet, denoted by dark regions in between jet pulses. LDV measurements of the jet speed within these regions may exhibit more clearly defined predominant frequencies in the FFT analysis.

3.4.5 Drag Measurements

Drag experiments were conducted to allow for measurements of the total hydrodynamic efficiency. Further details are discussed in section 4.4.3. Drag measurements of the submarine traverse, both with and without the vehicle, were obtained using a miniature precision load cell (Omega). The load cell was designed to measure both tension or compression loads with a 5 lb capacity. To minimize the effects of off-axis loads, the load cell uses a stainless steel weld construction. The accuracy of the device is +/- 0.15% of the full scale (linearity and hysteresis). The maximum output of the load cell is 10 mV without amplification. The load cell required a 5 VDC power input and was supplied by an AC powered signal conditioner (Omega Bridgesensor). The signal conditioner contains a precision differential instrumentation amplifier with voltage output. The frequency response of the device is 2 kHz with a gain range of 40 to 250. The excitation voltage supply range is 4 to 15 VDC, and was set to supply the necessary 5 VDC for the load cell. The output of the load cell was amplified by compressing the load cell by a known weight, near 100% of the full scale, and adjusting a potentiometer to achieve the desired full scale output. The load cell was then calibrated under compression by applying a series of known weights and measuring the amplified voltage output with a digital multimeter. The following curve was obtained as shown in figure 3.10. The output displays a linear relationship with applied load as expected.

3.4.5.1 Measurement Procedure

After calibration the load cell was placed in an assembly allowing the device to measure compression loads during the drag experiments. The load cell was anchored between the motorized traverse and submarine traverse. The active side of the load cell was screwed into a rod with a swivel bearing on the other end. This swivel bearing design relieved off-axis loads due to possible misalignment. The bearing was attached to an aluminum holder which was screwed into the submarine traverse by two 10-32 screws. See figure 3.11. An image of the drag experimental setup is shown in figure 3.12.

The drag force of the system was measured by setting the speed of the motorized traverse, allowing the load cell to compress and subsequently push the traverse with the attached submarine.

The experiments were then repeated without the submarine attached to measure the force necessary to push the traverse. The amplified load cell output was sent to the National Instruments data acquisition box and LabVIEW software was used to record the output. The Traverse Monitor software, as discussed in section 3.4.2.1, measured and recorded the motorized traverse speed and position. The friction force varied along the rails as they are not perfectly aligned. Data was recorded at the same start and stop position along the flume rails for each trial.

3.4.5.2 Calibration of Speed versus Drag Force

During self-propulsion experiments, the speed of the vehicle ranged from 8 to 55 cm/s. The drag on traverse both with and without the submarine was measured from speeds ranging from 8 to 60 cm/s. Figure 3.13 shows the relationship between drag force and speed. As speed increases, the drag of the traverse both with and without the submarine increases. The relationship between the traverse drag and speed is approximately linear. The force required to move the submarine traverse without attached submarine is the dominant contributor to the total drag on the system. On average, 89% of combined drag was due to friction in the submarine traverse. At lower speeds, the submarine traverse drag is as high as 96% of the combined drag. An estimate of the drag on the vehicle was obtained by subtracting the submarine traverse drag from the combined drag. The drag force on the submarine traverse increased at a higher rate with vehicle speed in comparison to the drag force on the vehicle itself. Due to magnitude of the uncertainty in the measurement of drag on the vehicle, it is not apparent that the drag on the vehicle is U_v^2.

A summary of the drag results for the traverse both with and without the vehicle attached is shown in Appendix D. Also shown in both summary tables is the standard deviation in the measurement of the drag force, σ_{drag}, and speed, σ_{speed}. The percent contribution of σ_{speed} to speed is greatest at the lower speed range for both cases as illustrated in figure 3.13.

3.4.5.3 Discussion of Spatial Variation of Drag Force Along Flume Rails

In general, as the speed increases the standard deviation in the drag force, σ_{drag}, increases. See figure 3.13. During drag experiments for the combined system, the percent contribution of σ_{drag} to the drag force reaches 26% in the lower-speed range in comparison to 17% in the higher-speed range. For the drag experiments of the traverse only, the percentage range is lower. The contribution reaches 24% at lower speeds and 14% at higher speeds. The variability in the drag measurement is a result of the misalignment of the flume rails. This misalignment increases the drag force on the submarine traverse pillowblocks. Figure 3.14 illustrates the variation of the drag force along the flume rails from a position of 0 to 700 cm as measured from the control panel.

Two cases are shown in the figure. One is at the low speed of 10.2 cm/s and another at a higher speed of 60.1 cm/s. Both of these cases are for combined system drag measurements. Although the measured drag is different for both cases, the dynamics of the measurements are similar. Both cases have peaks or increases in drag at similar positions along the flume rails. Given that the drag force varies along the rails, the experiments used the same start position.

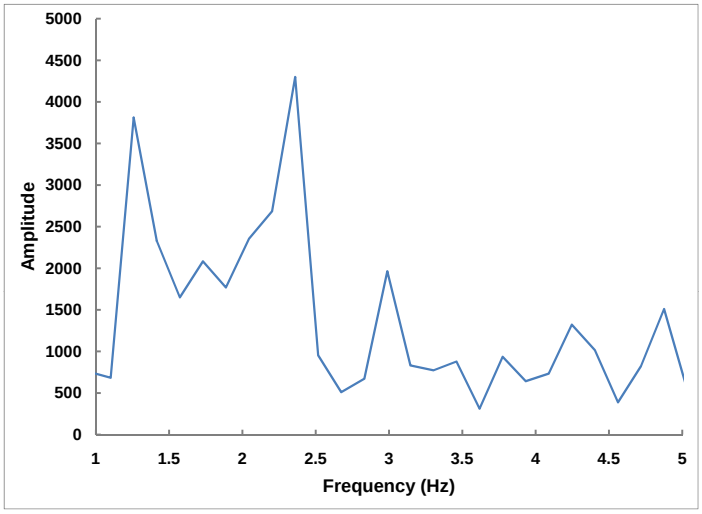

(a) FFT of jet center speed at a pulsing frequency of 2.3 Hz.

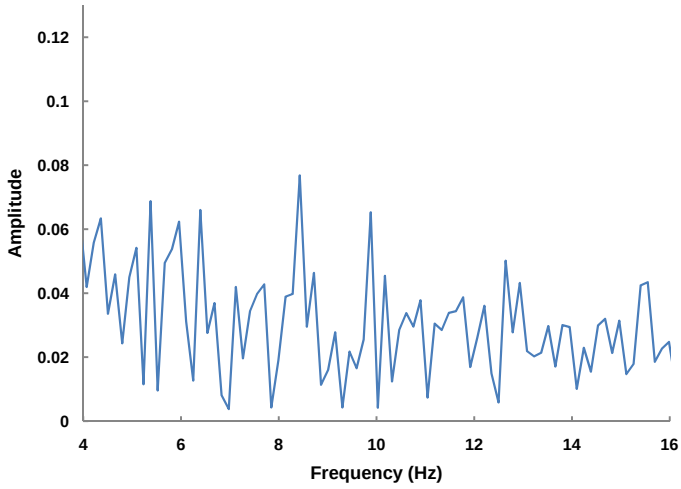

(b) FFT of jet center speed at a pulsing frequency of 9.3 Hz.

Figure 3.9. FFT of jet center speed at two pulsing frequencies. Pulsing frequency is distinguishable at the low motor speed.

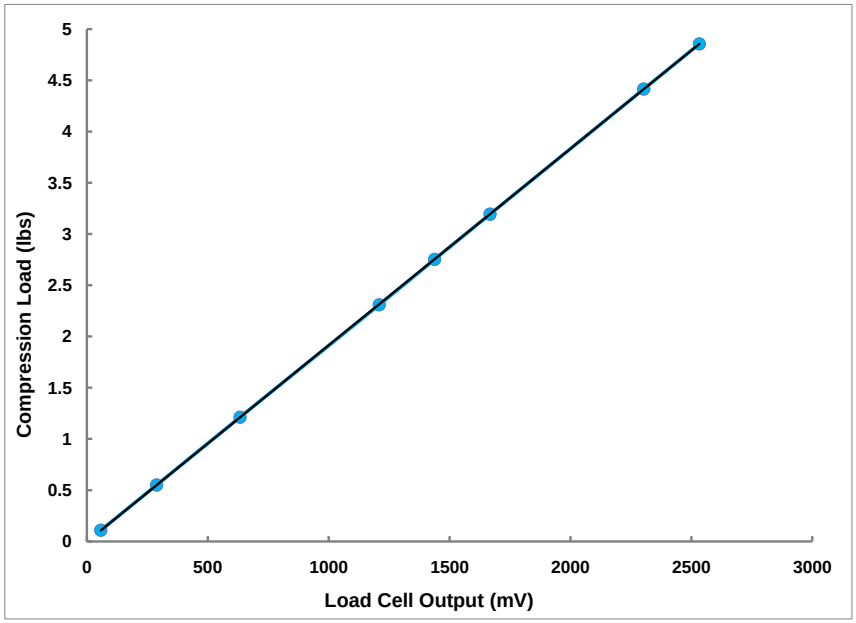

Figure 3.10. Load cell calibration under compression, y = 0.0019x − 0.003.

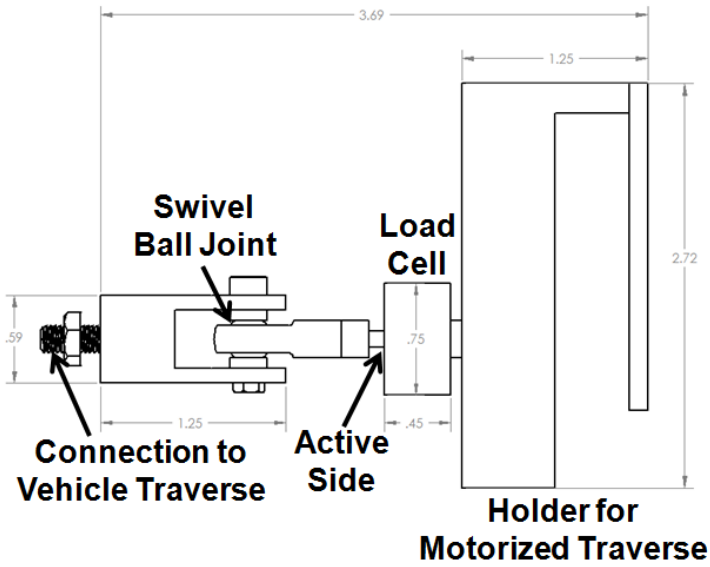

Figure 3.11. Schematic of load cell assembly.

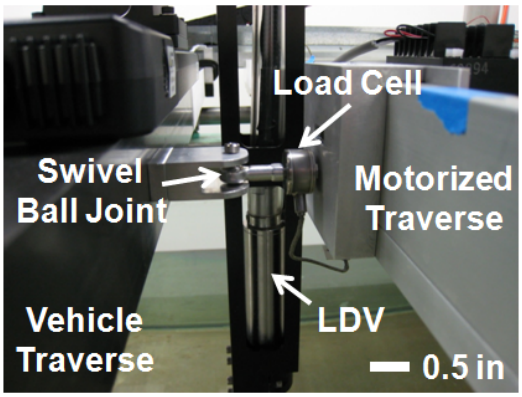

Figure 3.12. Image of load cell in drag experimental setup.

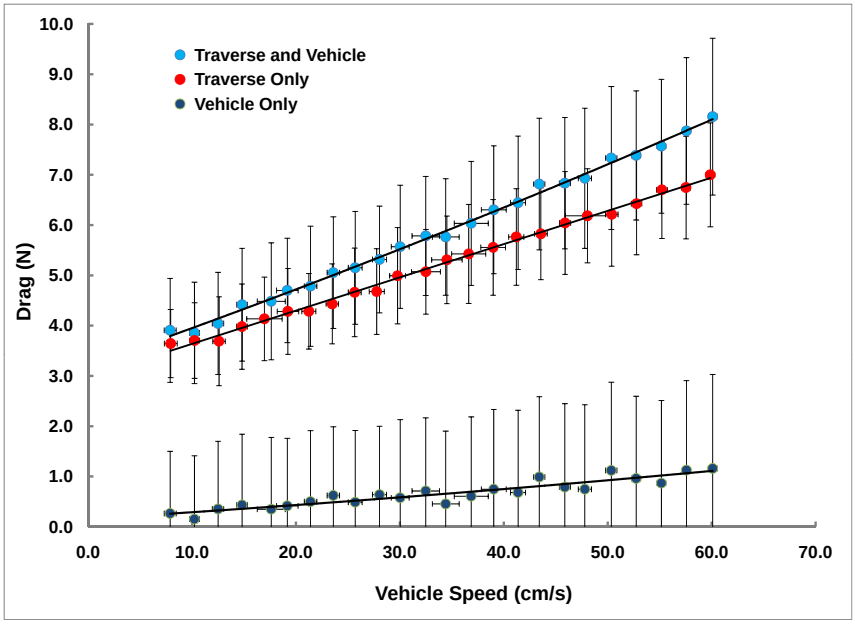

Figure 3.13. Drag measurements of traverse both with and without vehicle.

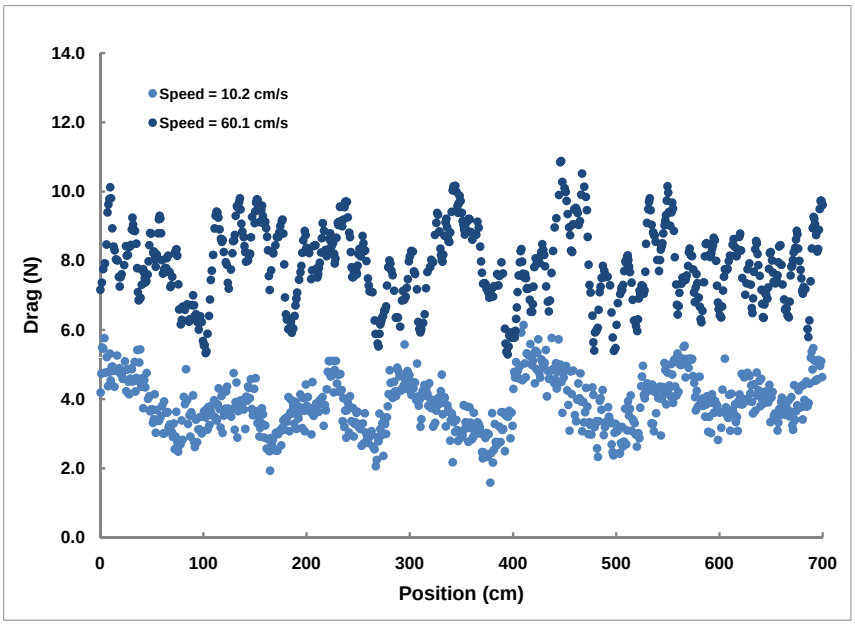

Figure 3.14. Graph illustrating the variation of the drag force along the flume rails.

Chapter 4

Empirical Demonstration and Investigation of Propulsive Performance

4.1 Introduction

This chapter describes the characterization of the jet flow and the investigation of the propulsive performance of the vehicle. Section 4.2 describes the experimental procedures and conditions that existed during experimentation. In section 4.3, the jet is characterized using two different experimental techniques, digital particle image velocimetry and planar laser-induced fluorescence. More specifically, section 4.3.1 shows the results obtained from the digital particle image velocimetry experiments. This technique was used to select an inner shell geometry for the pulsed jet configuration and to make comparisons between the steady and unsteady jet flow field. In section 4.3.2, the results obtained from the planar laser-induced fluorescence experiments were used as a tool for flow visualization. They provide insight on the behavior of the jet flow for both the steady and pulsed jet mode of propulsion. Section 4.4 shows results of propulsive performance measurements for three modes of vehicle propulsion. The configurations consisted of the steady jet with the inner rotating shell, the steady jet without the inner rotating shell and the pulsed jet. Initially the Froude efficiency of the vehicle was used as a propulsive performance metric. The results are displayed in section 4.4.1. It was discovered that increased Froude efficiencies may exist at higher vehicle speeds. This concept is explored in section 4.4.2. Another metric, the total hydrodynamic efficiency, was used to make

comparisons of the propulsive performance between the different modes of propulsion. The results from these experiments are found in section 4.4.3. Section 4.5 examines the propulsive efficiency observed in biological organisms. Finally, section 4.6 discusses the power coefficient and how it was measured to determine if a trade-off existed between improved propulsive performance and power consumption.

4.2 Experimental Conditions

The vehicle was held in a stationary position for the jet characterization results in section 4.3. The vehicle was set to operate at a constant motor speed. As a simplification, no inner rotating shell was used for the duration of the experiments in the steady propulsion mode. The rotational speed of the propeller was between 480 and 500 rpm. For the unsteady jet experiments, the geometry of the inner rotating shell was varied to observe the effects on jet dynamics. The rotational speed of the propeller was in the range of 650 to 730 rpm. Two fluid vents located on the top side of the vehicle were blocked using electrical tape upon discovering that it was necessary to decrease the pulsing frequency. Only the bottom fluid vent remained open. Given that the rotational rate of the inner shell is geared down by a ratio of 5 from the rotational rate of the propeller, the pulsing frequency ranged from 2.2 to 2.5 Hz. Both DPIV and PLIF measurements were made in spans ranging between 5 and 10 seconds. Numerous runs were conducted for each motor speed to ensure repeatability and reduce measurement noise.

To evaluate the propulsive performance of the steady and pulsed jet mode of propulsion, it was necessary to conduct these experiments during self-propulsion. The vehicle was set to propel down the facility at approximately the same start position. While in motion, the power consumed by the system, the rotational speed on the motor shaft, and the jet velocity were measured. The velocity of the vehicle was measured indirectly by recording the velocity of the motorized traverse that tracked the vehicle at a preset distance of 40 cm. Depending on the speed of the vehicle, 5 to 10 seconds of data was acquired per run. Sufficient time was necessary to allow for temporal averaging to reduce measurement noise. Only the axial jet velocity at the center of the jet was measured using LDV

given that the axial jet velocity along the radial direction of the jet is constant. See section 5.4.1.

Initial propulsive performance studies were conducted for three vehicle configurations, the steady jet with the inner rotating shell, the steady jet without the inner rotating shell and the pulsed jet. It was discovered from the characterization studies that an inner shell opening of 300^o was necessary to produce a pulsed jet with vortex ring formation. Fifteen trials of experiments were conducted with this inner shell geometry. The rotational speed of the propeller ranged from 2540 to 2960 rpm. A total of 16 trials were performed with an inner shell geometry producing a steady jet with an equivalent mechanical efficiency as the unsteady configuration. The rotational rate of the propeller operated in a range of 2580 to 2920 rpm. Finally, 16 baseline trials were performed in a steady configuration without an inner rotational shell. The propeller rotational rate for these cases ranged from 2420 to 2970 rpm. Difficulties arose in reaching and maintaining higher rotation speeds than those tested due to input power requirements.

Another series of performance studies was conducted to observe the propulsive performance at higher vehicle speeds. A 60 V power supply was used to supply the constant power necessary for the vehicle to attain higher speeds. The original motor was replaced due to mechanical failure. The performance of the new motor varied from the original despite using the same model. It was observed that an increased propeller rotational speed was necessary to achieve the same vehicle speed, therefore decreasing the pulse duration.

Two sets of experiments were conducted for the secondary study. A total of 12 experiments were conducted evaluating the propulsive performance of the unsteady mode of propulsion. The rotational rate of the propeller varied from 2740 to 3770 rpm. Twelve experiments of the steady jet configuration without the rotational shell were performed as comparison. The steady shell was not used in order to simplify the experiments and to decrease motor stress. The rotation rate of the propeller spanned 2900 to 3830 rpm. The power supplied directly to the motor was measured and recorded in addition to system power usage.

4.3 Jet Characterization: Flow Visualization

4.3.1 PIV Measurements

4.3.1.1 Inner Shell Modification and Effect to Unsteady Jet Formation

The initial inner shell geometry was designed with three 26^o fluid openings. See figure 4.1(a) where θ_{io} is the inner rotational fluid shell opening. One complete revolution of the inner shell results in 3 instances in time where the fluid vents were aligned, resulting in 3 jet pulses per revolution. An instance of the velocity field of the jet obtained using DPIV is shown in figure 4.2. The motor was operating at 671 rpm during this particular trial, hence, the fluid vents aligned at a frequency of 7.70 Hz. The Reynolds number, Re_j of the jet based on the average jet velocity, U_{avg}, and D, the exit jet diameter, was 2700.

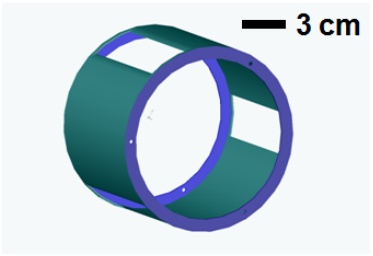

(a) Shell with $\theta_{io} = 26^o$ and $t^* \approx 0.038$.

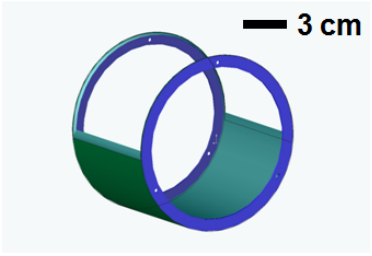

(b) Shell with $\theta_{io} = 180^o$ and $t^* \approx 0.321$.

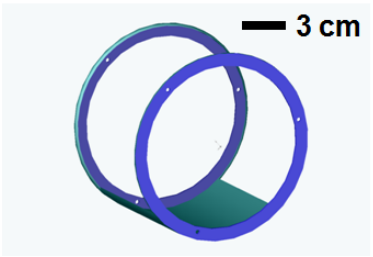

(c) Shell with $\theta_{io} = 270^o$ and $t^* \approx 0.472$.

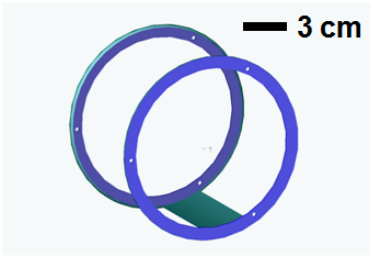

(d) Shell with $\theta_{io} = 334^o$ and $t^* \approx 0.888$.

Figure 4.1. Inner shell geometries tested. The shell with $\theta_{io} = 334^o$ was selected for the propulsive performance studies.

The formation time, t^*, was also measured and used to characterize the jet flow. The formation time is the nondimensional time equivalent to the ratio of the length to the diameter of an ejected fluid column otherwise known as the stroke ratio (Gharib et al. 1998). It is expressed as

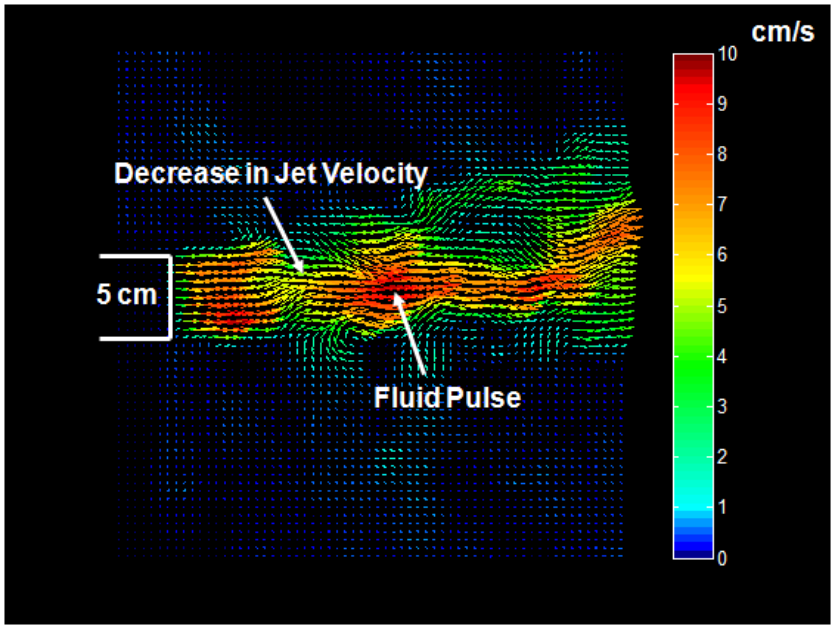

Figure 4.2. Instantaneous velocity field of the jet with the vehicle configured with the 26^o fluid opening for the inner shell geometry.

$$t^* = \frac{U_{avg}\, t}{D}, \tag{4.1}$$

where $t = \theta_{io}/\,\omega$ is the fluid discharge time or the amount of time the fluid vents are aligned per pulse duration and ω is the angular velocity of the inner rotating shell.

From figure 4.2 it is evident that no vortex ring formation is present with this shell geometry. Pulsing of the jet is evident by a period of time where the core jet velocity is 10 cm/s followed by a period of time where the jet velocity decreases to 5 cm/s. Using the measurement of U_{avg} obtained from the DPIV data, the formation time was calculated to be 0.04 for the case of the vehicle configured with the 26^o degree fluid opening in the inner shell geometry operating at a motor speed of 670 rpm.

Didden (1979) noted that isolated vortex rings could not be produced for $t^* < 0.4$. Given this condition on t^*, θ_{io} was increased in an effort to increase the fluid discharge time. As a consequence of increasing θ_{io}, the two fluid vents located on the top of the submarine were blocked with electrical tape to prevent the inner shell opening from overlapping with more than one fluid vent at a time.

The inner shell was redesigned allowing for only one fluid opening per revolution of the shell.

DPIV experiments were then conducted on the vehicle jet with the motor operating at 640 rpm and a 180^o fluid opening for the inner shell geometry. See figure 4.1(b) for the geometry of the shell. The pulsing frequency was 2.15 Hz as the inner fluid vent aligned with the outer fluid once per revolution. Re_j was 3175 and t^* reached a value of 0.32. The velocity in the core center of each pulse reached a velocity of 14 cm/s. In contrast to the previous experiments conducted with the 26^o inner fluid opening, it was now apparent that ambient flow near the jet exit was entrained into the jet during the formation of a pulse. These flow characteristics can be seen in figure 4.3(a).

The inner fluid shell opening was further increased to 270^o. See figure 4.1(c) for the geometry of the shell. DPIV experiments were conducted on the jet flow of the vehicle with the motor operating at a comparable rotational speed to previous experiments. The rotational speed was 650 rpm giving a pulsing frequency of 2.2 Hz. This increase in shell opening led to a further increase in t^* to a value of 0.47. The Re_j for the jet flow was 3630. With the increased inner shell fluid opening, the velocity in the core of the pulse had a corresponding increase to 20 cm/s. Flow roll up was now apparent which is suggestive of vortex ring formation. See figure 4.3(b).

To further increase the fluid roll up, t^* was increased by increasing the size of the inner shell fluid opening to 334^o. The geometry of this inner rotational shell can be seen in figure 4.1(d). The motor was set to operate at 740 rpm producing a pulsing frequency of 2.5 Hz. At this rotation speed, Re_j was equal to 5443 and t^* increased to 0.89. Vortex ring formation was apparent with this inner shell geometry. See figure 4.4(a). The maximum velocity in core of the vortex reached 35 cm/s. The vorticity contour is also illustrated for this instantaneous velocity field in figure 4.4(b). The vorticity contour demonstrates symmetric vorticity along the jet centerline. This shell geometry with $\theta_{io} = 334^o$ was used for the remainder of the propulsive performance studies.

4.3.1.2 Steady Jet Configuration

DPIV experiments were also performed on the vehicle for the steady mode of propulsion without the inner rotating shell. The velocity field demonstrates a uniform field with the jet achieving a

maximum velocity of 25 cm/s and a Re_j of 7250. See figure 4.5. The jet maintains a cylindrical shape until 1.5 jet diameters downstream. Downstream from this point, instabilities in the shear layer break up the cylindrical shape of the jet, and the jet appears less ordered and no longer round. There is significantly less entrainment near the nozzle exit in comparison to the unsteady mode of propulsion with the inner shell geometry of $\theta_{io} = 334^o$.

4.3.2 PLIF Measurements

PLIF experiments were conducted for both the steady mode of propulsion without the inner rotating shell and the unsteady mode of propulsion with the inner shell geometry of $\theta_{io} = 334^o$. For these experiments, the rotational speed of the motor for the steady configuration was 500 rpm and 730 rpm for the unsteady configuration. For the pulsed jet configuration, entrainment of the ambient flow into the vortex ring is illustrated by the dark regions within the vortex ring in figure 4.6. The additional mass transfer into the vortex led to a larger wake size in comparison to the the steady jet as a result of vortex ring formation.

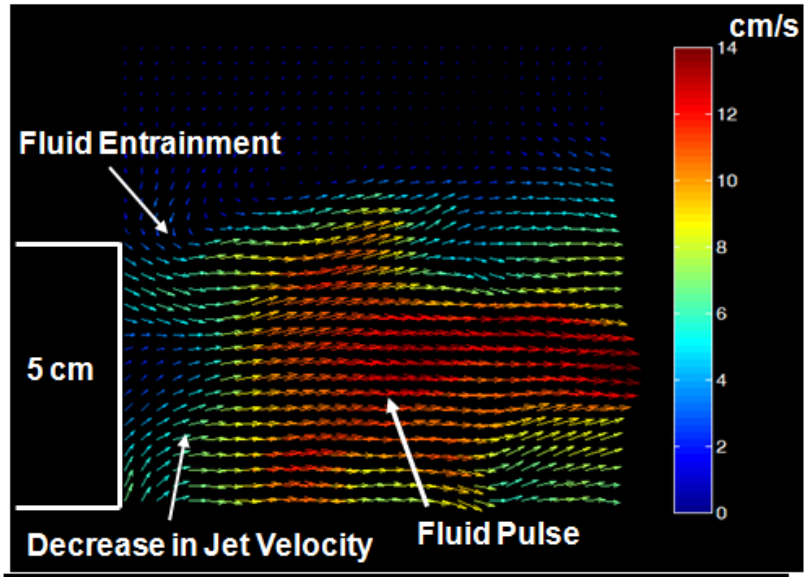

(a) Vehicle configured with the 180^o fluid opening inner shell geometry.

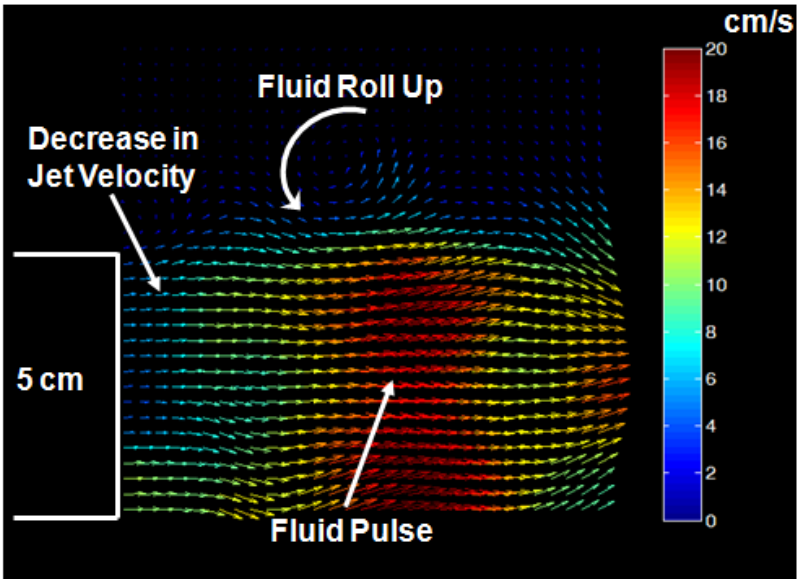

(b) Vehicle configured with the 270^o fluid opening inner shell geometry.

Figure 4.3. Instantaneous velocity field of the jet with the vehicle configured with two unsteady shell geometries.

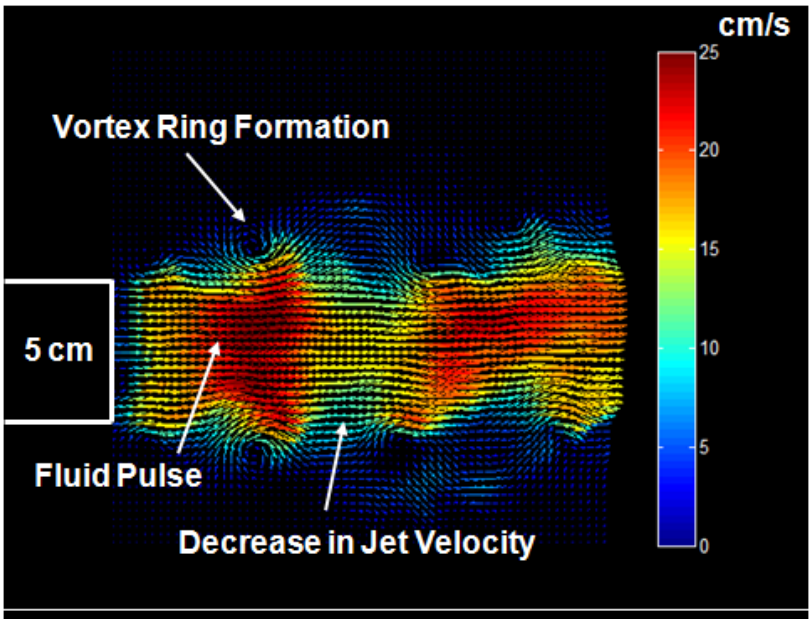

(a) Instantaneous Velocity field illustrating vortex ring formation.

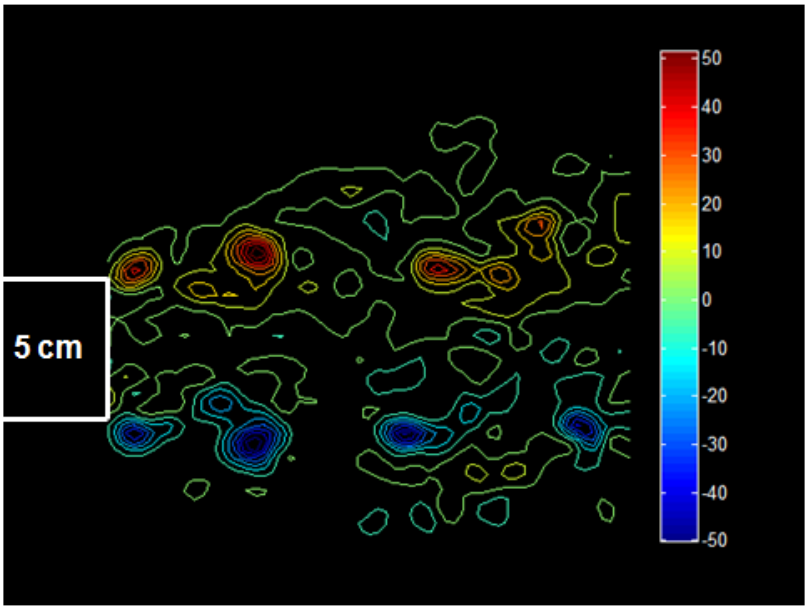

(b) Vorticity contour illustrating symmetric vorticity along jet centerline.

Figure 4.4. Instantaneous velocity field and vorticity contour of the jet with vehicle configured using final unsteady shell geometry with $\theta_{io} = 334^o$.

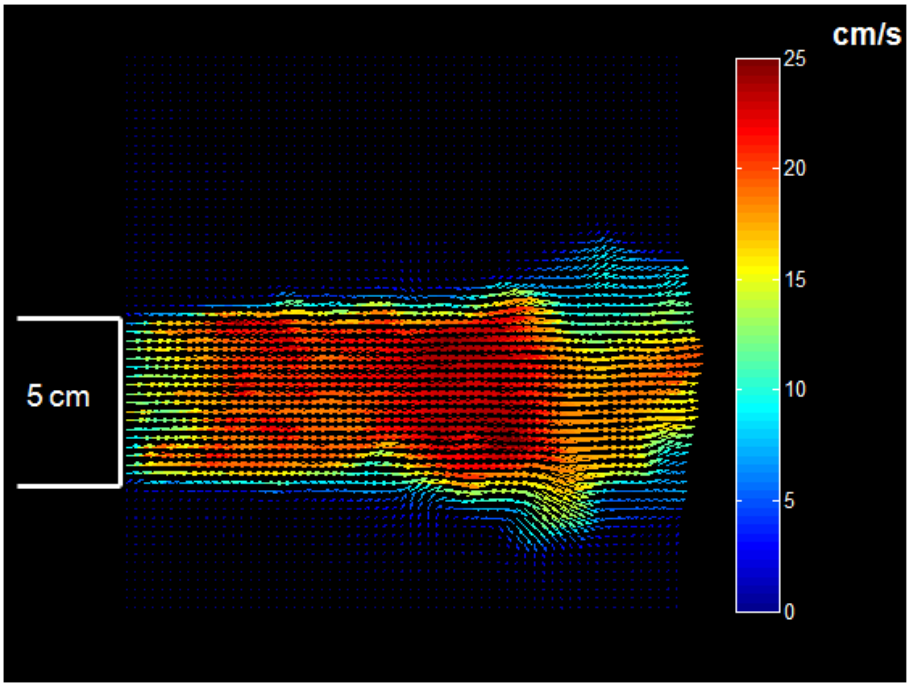

Figure 4.5. Instantaneous velocity field of the jet with vehicle in steady mode of propulsion without the inner rotational shell.

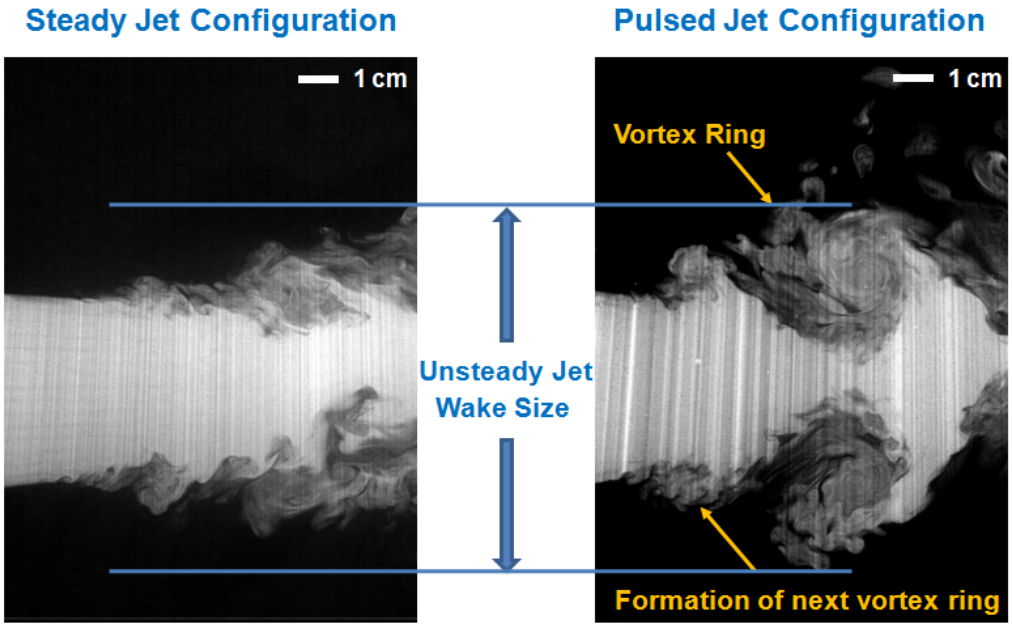

Figure 4.6. PLIF images illustrating a larger wake size for the pulsed jet in comparison to the steady jet due to the formation of vortex rings.

4.4 Measurement of Propulsive Performance

The data obtained from both propulsive performance studies is cataloged in Appendix E. Included with the data are the standard deviations in the measurements. The average standard deviation in the motor speed was 30 rpm. The average standard deviation in the vehicle speed was 3.2 cm/s for the first set of propulsive performance studies. The standard deviation in vehicle speed increased to 5 cm/s for the second set of data obtained using the second motor. It is important to note that although the jet efflux is unsteady for the pulsed jet configuration, the mass of the vehicle acts as a low-pass filter such that oscillations in the cruising velocity are negligible. The deviation in mean speed is due to the nonuniform drag force experienced by the vehicle as it translates along the flume facility and the ability of the speed controller to maintain a constant motor speed. Figure 4.7 illustrates the variation in the speed of the vehicle over the duration of the experiment for both the pulsed jet and steady jet without the rotating shell. It is apparent from the figure that the variation in vehicle speed for the pulsed jet configuration does not coincide with the pulsing frequency.

4.4.1 Comparison of Froude Efficiency for Both Steady and Unsteady Jet Propulsion

For the first set of propulsive performance studies the Froude efficiency was measured for three vehicle configurations, the steady jet with the inner rotating shell, the steady jet without the inner rotating shell and the pulsed jet. The Froude efficiency was calculated using equation (4.2),

$$\eta_F = \frac{2}{1 + U_{avg}/U_v}, \tag{4.2}$$

where U_{avg} is the average jet velocity and U_v is the average vehicle speed. Given that the Froude efficiency applies for a body moving at steady state velocity, the standard deviation in U_v was used to compute the error in the measurement of the efficiency.

Figure 4.8 is a plot of the Froude efficiency versus motor speed for the three modes of propulsion. At the lower motor speeds tested, it is difficult to determine whether a potential benefit exists with

pulsed jet propulsion given the uncertainty in the measurement. As the motor speed increases, the Froude efficiency for the pulsed jet increases at a higher rate in comparison to both steady types. In order to gain an understanding of the magnitude of the increased Froude efficiency generated by using a pulsed jet for propulsion, the data was normalized by the baseline case of the steady jet without the rotating shell. See figure 4.9. The steady jet without the rotating shell is denoted as SWOS. A value of 1 for all motor speeds denotes the normalized efficiency for the steady jet without the rotating shell, and the gray band signifies the uncertainty in the measurement. The Froude efficiency increased linearly with motor speed for all modes of propulsion. The pulsed jet has a higher Froude efficiency in comparison to both steady types for most motor speeds. On average, the pulsed jet has a 40% increase in the Froude efficiency at higher motor speeds. The steady jet with the rotating shell falls within the uncertainty of the steady jet without the rotating shell for most values of normalized efficiency.

The Froude efficiency was also measured for the data obtained using the second motor. The results are shown in figure 4.10. The goal of this set of experiments was to observe the change in Froude efficiency at higher motor speeds. Similar trends were observed with this set of data in comparison to the first data series. The Froude efficiency increased linearly with motor speeds for both modes of propulsion. At the lower motor speeds tested, it is difficult to determine whether a potential benefit exists with pulsed jet propulsion given the uncertainty in the measurement. Similar to previous experiments, as the motor speed increases, the Froude efficiency increases at a higher rate for the pulsed jet mode of propulsion in comparison to the steady jet. The Froude efficiency was normalized by the Froude efficiency of the steady jet without the rotating shell, as shown in figure 4.11. At the higher motor speeds, the pulsed jet achieved on average a 20% increase in Froude efficiency in comparison to the steady jet without the rotating shell. This increase in Froude efficiency is 50% lower than observed with the first series of experiments. To gain an understanding of the source of the difference, the Froude efficiency for all the experiments were plotted together versus motor speed. See figure 4.12.

It is apparent that similar trends exist between both data sets from the compiled Froude efficiency

measurements, however, the results are shifted in motor speed. Another difference is evident in the rate of increase in the measure of Froude efficiency for the pulsed jet mode of propulsion. The rate of increase is steeper for the initial motor results. For the second motor, the motor speed was increased in order to produce an equivalent average jet speed generated using the initial motor. See figure 4.13. The formation time for vortex ring formation was calculated using equation (4.1). The formation time had a corresponding decrease as a result of the increase in motor speed, as shown in figure 4.14. The formation time was greater using the initial motor for a given vehicle speed with the exception of one point. This leads to a larger formation time and an increased impulse generated by the developing vortex ring (Krueger and Gharib 2003). This explains the increase in propulsive performance.

4.4.2 Effects of Increased Vehicle Speed on Froude Efficiency Model

The relationship between jet velocity and vehicle speed was examined to determine the effect of increased vehicle speed on Froude efficiency. Figure 4.15 is a plot of the average temporal jet velocity, U_{avg}, versus the average vehicle speed, U_v, for experiments conducted with the initial motor. The average jet velocity approaches a steady state velocity of 160 cm/s as motor speed increases. The following dashed curve is generated as shown in figure 4.16 by taking the average jet velocity of 160 cm/s and plugging it into the Froude efficiency.

The data obtained using the initial motor was included and plotted in the figure. The data resides on the bottom portion of the dashed curve of the Froude efficiency model. Although the maximum motor speed was comparable among all modes of propulsion, the highest measurement in the Froude efficiency was obtained for the experiments using pulsed jet propulsion. Initial propulsive performance studies suggested that there may be further increases in the Froude efficiency at higher motor speeds. To investigate this possibility, experiments were conducted at higher motor speeds with the secondary motor. A few experiments were conducted at comparable motor speeds to the first series of experiments to verify repeatability. The results from the higher speed experiments were plotted against the model of the Froude efficiency with an average jet velocity of 180 cm/s in

figure 4.17. The higher speed results continue to follow the modeled dashed curve. With increased vehicle speed, the Froude efficiency reached a maximum value of 47% for the pulsed jet configuration. Whether the Froude efficiency would continue to increase could not be determined from the data. It is important to note that as the body velocity approaches the jet velocity, the thrust approaches zero since the thrust is approximated as $\dot{m}(U_{avg} - U_v)$ in the derivation of the Froude efficiency.

4.4.3 Comparison of Total Hydrodynamic Efficiency for Both Steady and Unsteady Jet Propulsion

Another metric for the measure of propulsive performance is the total hydrodynamic efficiency. The total hydrodynamic efficiency is defined as the ratio of useful work over the useful work plus wasted energy. The useful work is the product of the thrust and the vehicle speed. The wasted energy is defined as any kinetic energy left in the wake as a result of jetting relative to the surrounding flow and is equal to the product of $\frac{1}{2}\rho\, A_j\, U_{avg}\,(U_{avg} - U_v)^2$. Making the substitution for useful work and wasted energy into the definition of the total hydrodynamic efficiency, the following result is obtained,

$$\eta_{hydro} = \frac{useful\ work}{useful\ work\ +\ wasted\ energy} = \frac{D\,U_v}{D\,U_v\ +\ \frac{1}{2}\rho\, A_j\, U_{avg}\,(U_{avg} - U_v)^2}, \tag{4.3}$$

where A_j is the area of the jet exit. Given that the system is traveling at steady state, the thrust produced by the system is equivalent to the drag. The drag was measured in an independent experiment, as described in section 3.4.5. The definition of the total hydrodynamic efficiency does not make any approximation of the drag in contrast to the Froude efficiency.

For the first set of propulsive performance studies, the total hydrodynamic efficiency was measured for three vehicle configurations, the steady jet with the inner rotating shell, the steady jet without the inner rotating shell and the pulsed jet. Given that the vehicle is assumed to be traveling at steady state, the standard deviation in the vehicle speed was used to generate the error in the measurement of the efficiency. Figure 4.18 shows the relationship between the total hydrodynamic

efficiency versus motor speed. Similar to the results of the propulsive efficiency, at lower motor speeds, it is difficult to infer whether the pulsed jet produces an increase in efficiency over both steady jet types within the uncertainty of the measurement. At higher motor speeds it is evident that the pulsed jet is superior to both steady jet types. The pulsed jet acquired maximum total hydrodynamic efficiency of 54% at a motor speed of 2890 rpm. The normalized total hydrodynamic efficiency versus motor speed is shown in figure 4.19. At motor speeds above 2800 rpm, there is a 57% average increase in the total hydrodynamic efficiency of the pulsed jet in comparison to the steady jet. With the exception of a few data points, the results for the steady jet with the rotating shell fall within the measurement uncertainty of the normalized hydrodynamic efficiency for the steady jet without the rotating shell.

The results of total hydrodynamic efficiency versus motor speed for the second motor are shown in figure 4.20. It is apparent that the pulsed jet produces a higher total hydrodynamic efficiency at motor speeds higher than 3500 rpm. The total hydrodynamic efficiency reached the highest value of 63% at a motor speed of 3770 rpm for the vehicle traveling in the pulsed jet configuration. There is an average 32% increase in the hydrodynamic efficiency for the pulsed jet at motor speeds above 3500 rpm after normalizing the hydrodynamic efficiency by the results for the steady jet without the rotating shell.

Measurements of the total hydrodynamic efficiency for both series of experiments can be analyzed in figure 4.22. The results from the second study of hydrodynamic efficiency are shifted in motor speed similarly to the compiled results of the propulsive efficiency. The rate of increase in the hydrodynamic efficiency for the initial pulsed jet experiments is greater in comparison to the measurements obtained with the second motor. The decrease in performance for the second motor can be attributed to a decrease in the vortex ring formation time.

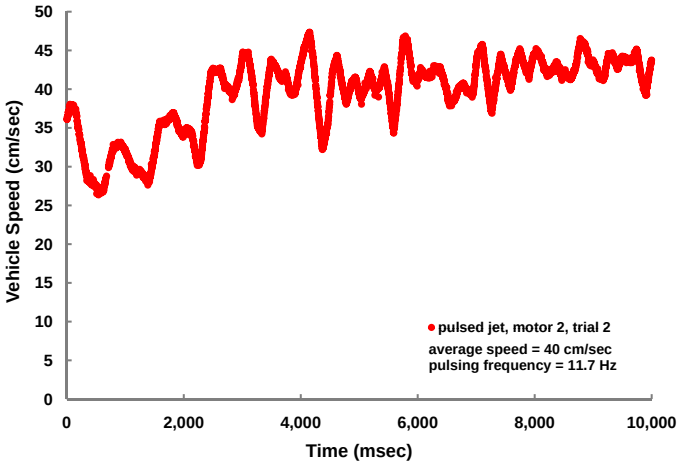

(a) Vehicle speed obtained using a pulsed jet.

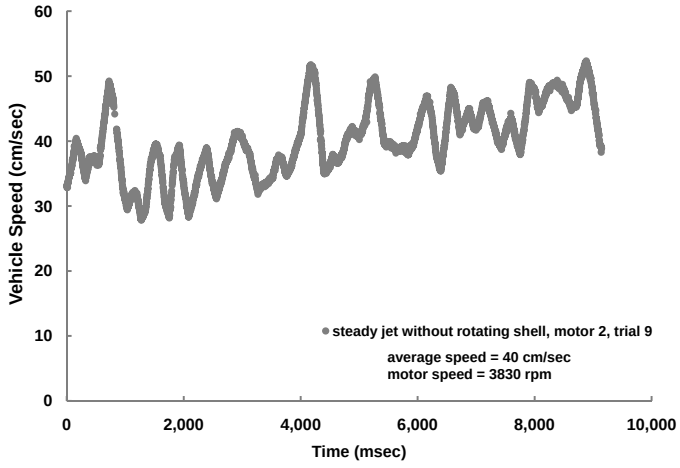

(b) Vehicle speed obtained using a steady jet without the inner rotating shell.

Figure 4.7. Illustration of typical variation in vehicle speed over the duration of an experiment.

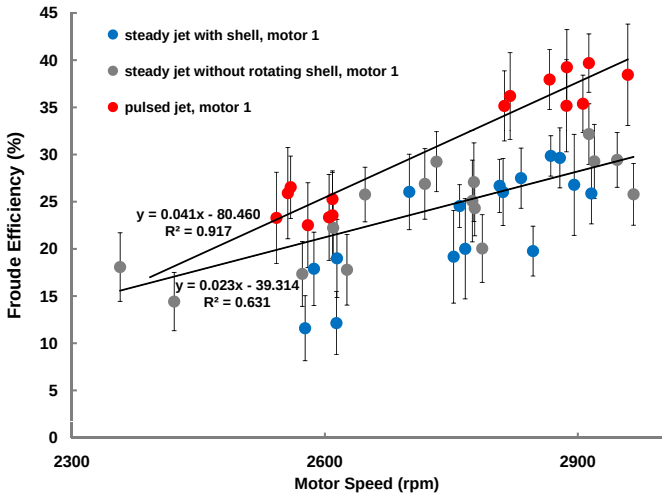

Figure 4.8. Froude efficiency versus motor speed for motor 1.

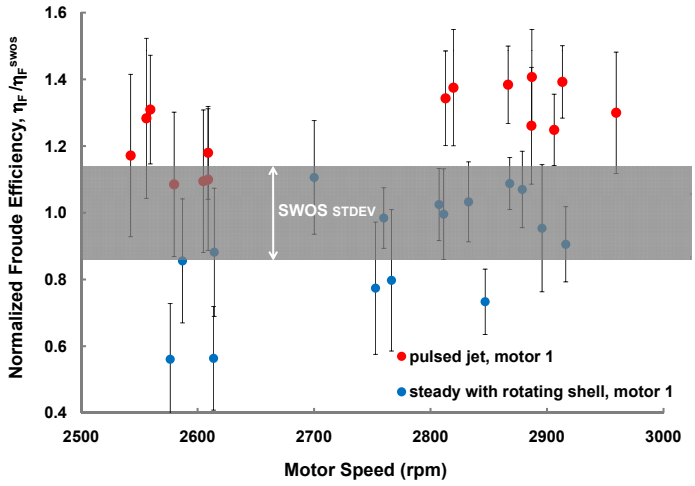

Figure 4.9. Normalized Froude efficiency versus motor speed for motor 1.

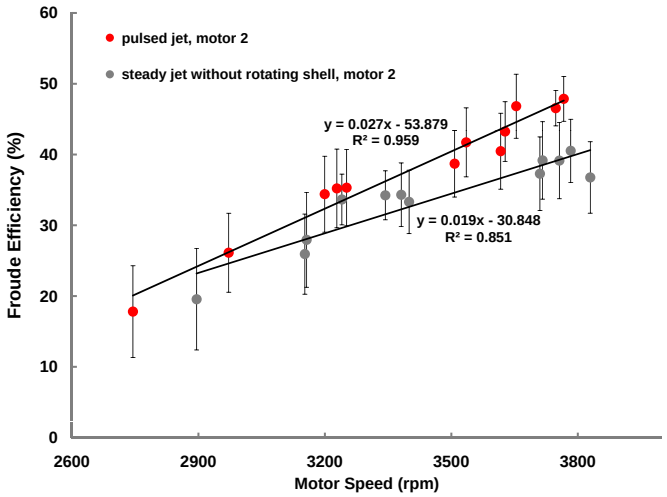

Figure 4.10. Froude efficiency versus motor speed for motor 2.

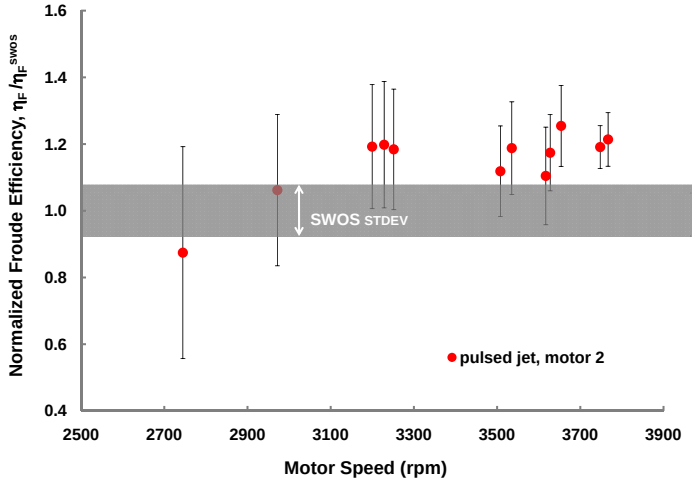

Figure 4.11. Normalized Froude efficiency versus motor speed for motor 2.

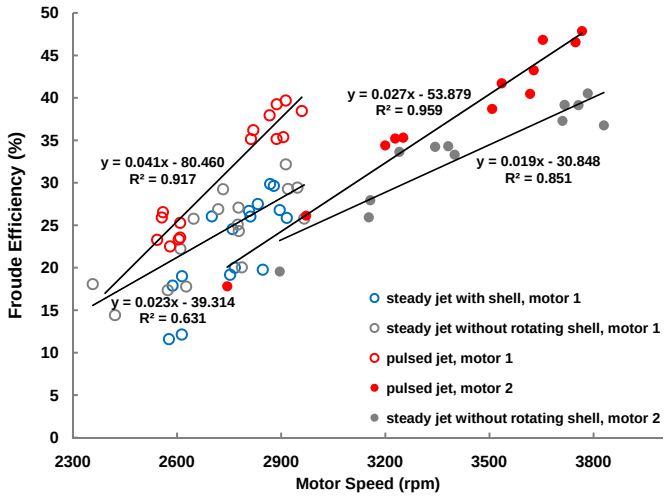

Figure 4.12. Compiled results for the measure of Froude efficiency versus motor speed.

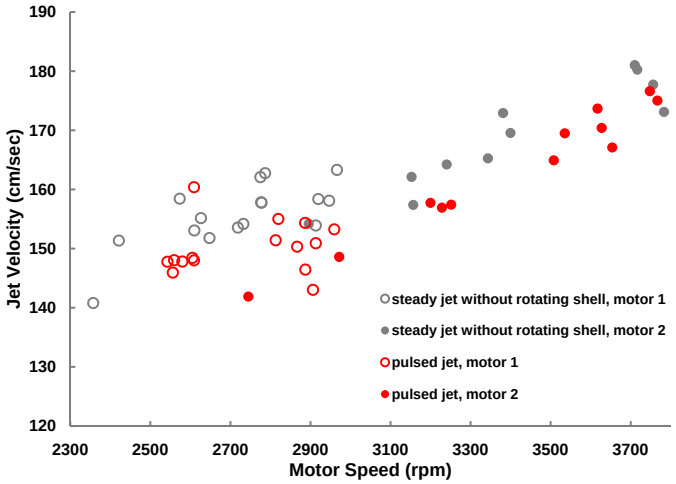

Figure 4.13. Graph of jet speed versus motor speed. An increase of motor speed is necessary with the second motor to produce an equivalent jet speed generated using the initial motor.

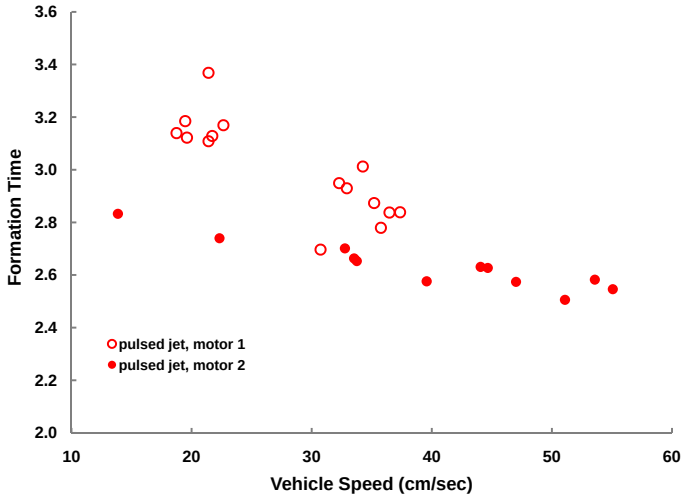

Figure 4.14. Formation time versus vehicle speed.

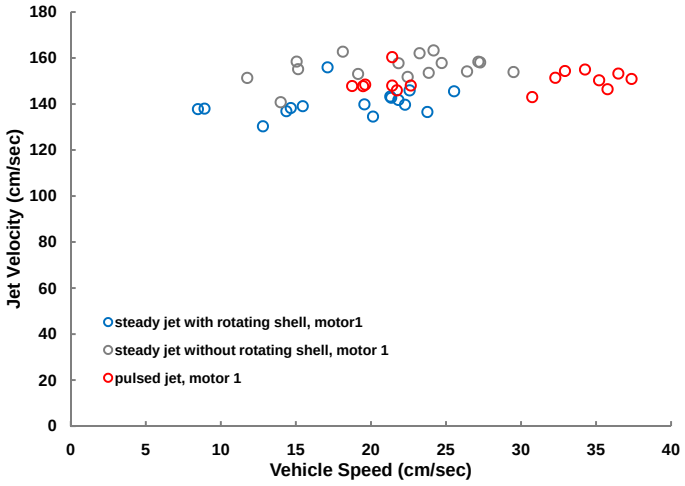

Figure 4.15. Graph of jet speed versus motor speed. Jet speed approaching a steady state value of 160 cm/s.

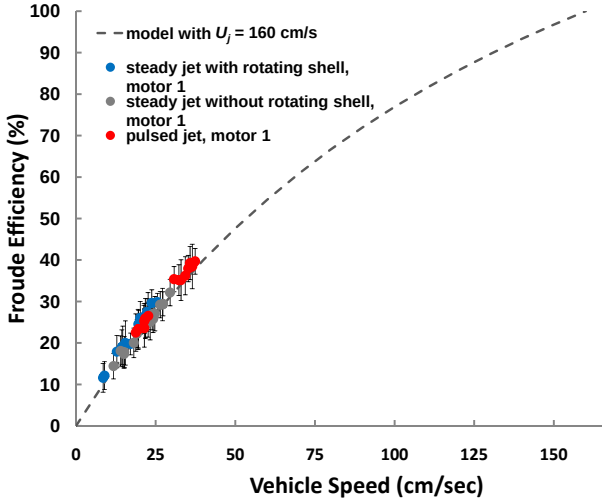

Figure 4.16. Graph of Froude efficiency versus vehicle speed. Possibility of further improvement at higher vehicle speeds.

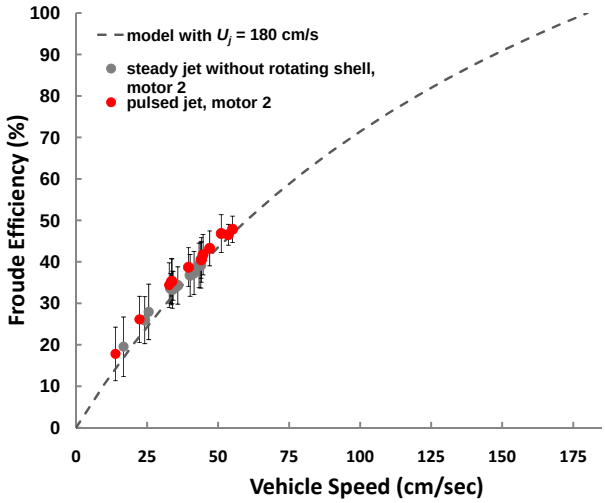

Figure 4.17. Graph of Froude efficiency versus vehicle speed. Demonstration of increased propulsive performance at higher vehicle speeds.

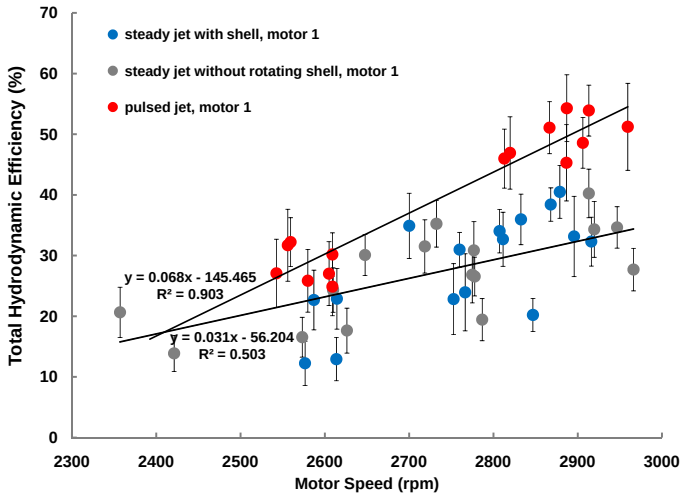

Figure 4.18. Total hydrodynamic efficiency versus motor speed for motor 1.

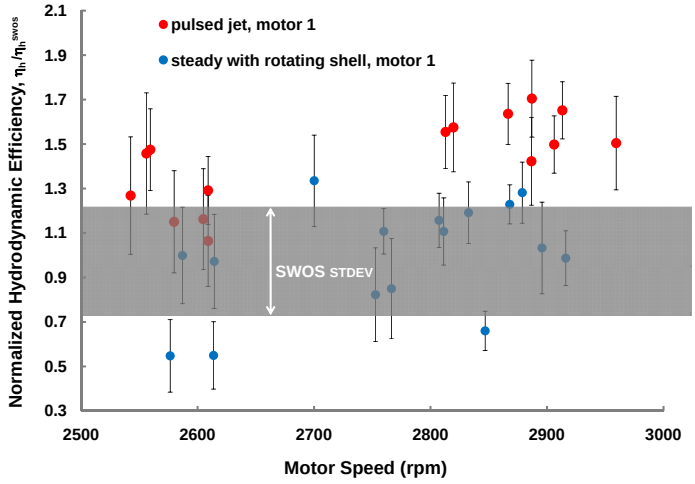

Figure 4.19. Normalized total hydrodynamic efficiency versus motor speed for motor 1.

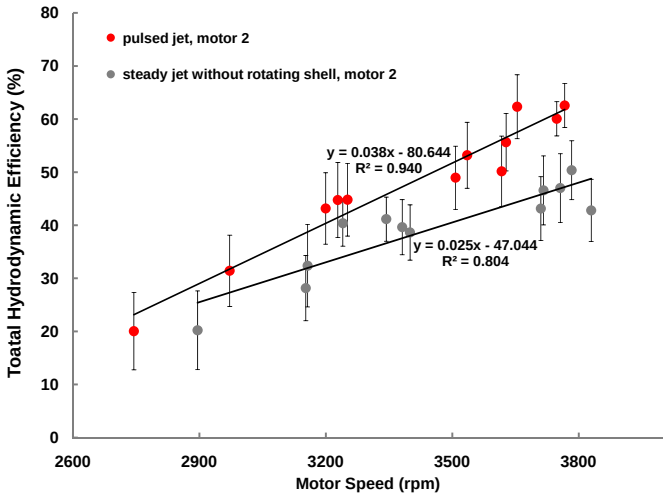

Figure 4.20. Total hydrodynamic efficiency versus motor speed for motor 2.

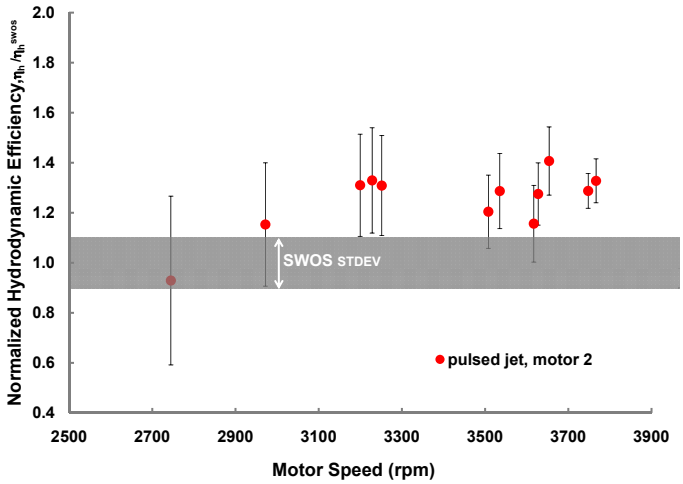

Figure 4.21. Normalized total hydrodynamic efficiency versus motor speed for motor 2.

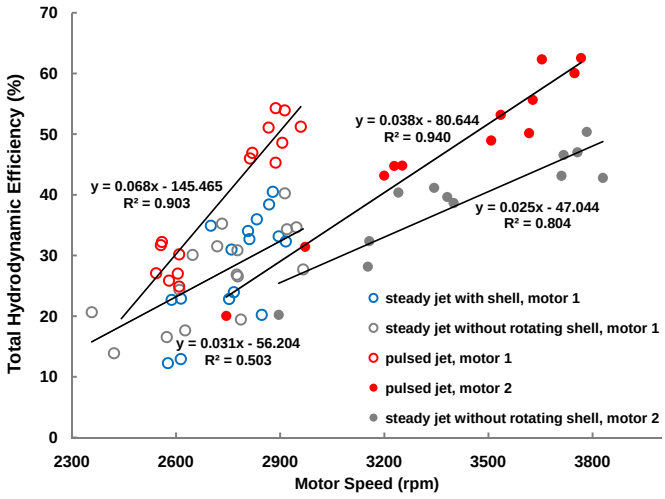

Figure 4.22. Compiled total hydrodynamic efficiency versus motor speed.

4.5 Comparison of Propulsive Efficiency to Other Biological Organisms

Biological organisms have been shown to display high propulsive efficiencies due to the production of vortex rings during propulsion. Squid have been shown to achieve propulsive efficiencies as high as 57.5% at a swimming speed of 9 cm/s, Bartol et al. (2001). At the highest swimming speed of 27 cm/s, the Froude efficiency decreased to 45%. Anderson and DeMont (2000) showed similar results for a 0.2 kg squid swimming at 50 cm/s. The measured average Froude efficiency reached 56%. Tytell and Lauder (2004) was able to measure the Froude efficiency of a steady swimming eel at 1.4 L s^{-1}, which was estimated to range from 50% to as high as 87%. Nauen and Lauder (2002) measured an average Froude efficiency of 74% for rainbow trout swimming at 1.2 Ls^{-1}. In comparison to the Froude efficiency achieved by biological organisms, as illustrated in figure 4.17, the highest measured Froude efficiency for the pulsed jet, propeller driven vehicle was 48% produced at a speed of 55 cm/s. This result in Froude efficiency is close to what has been measured of biological organisms. Furthermore, at higher vehicle speeds, the vehicle may achieve an increased Froude efficiency.

4.6 Comparison of Power Consumption for Both Steady and Unsteady Jet Propulsion

The pulsed jet configuration showed increased propulsive performance in comparison to the steady jet configuration both with and without the inner rotating shell. The power consumed by the motor, P_{input}, was measured to determine if a trade-off exists between improved propulsive performance and power consumption. Using power measurements, a power coefficient, (4.4), was defined similar to the approach utilized by Krueger (2006), Schultz and Webb (2002), Tytell (2004), and Tytell and Lauder (2004).

$$C_p = \frac{P_{input}}{\frac{1}{2}\,\rho\,S\,{U_v}^3}, \tag{4.4}$$

where ρ is the fluid density, S is the wetted surface area of the vehicle, and U_v is the averaged vehicle speed.

As the motor speed increases, the power coefficient significantly decreases for both modes of propulsion. See figure 4.23. The error bars denote the uncertainty in C_p, taking into account the error in the measurement of power. Data points where the error bars are not visible are a result of the error being smaller than the size of the data marker. At the lower motor speeds, a significant portion of the power supplied to the motor is used to overcome the static friction on the pillowblocks before the vehicle begins to move. This results in a higher C_p. At higher motor speeds, the ratio of power supplied to increase the velocity of the vehicle to the power supplied to overcome friction, is higher, resulting in a lower value for C_p. It is advantageous to minimize C_p. This can be accomplished by increasing the velocity of the vehicle while supplying less power. A trend line was used to fit a curve through the steady jet configuration data. The curve fit was used to normalize C_p by the baseline case of the steady jet without the rotating shell. See figure 4.24.

A normalized power coefficient value of 1 for all motor speeds denotes the baseline case for the steady jet without the rotating shell. The gray band represents the uncertainty in the measurement. The error bars indicate the uncertainty in the normalized power coefficient taking into account the error in the measurement of power. Although the pulsed jet configuration utilizes additional power to rotate the planetary gear system, the enhanced thrust production leads to an equivalent or smaller power coefficient in comparison to the steady jet configuration with the exception of two data points. The reduced cost in power for pulsed jet propulsion is most significant at the highest motor speeds. At the highest motor speed the normalized power coefficient is 37% less than the power coefficient for steady jet propulsion.

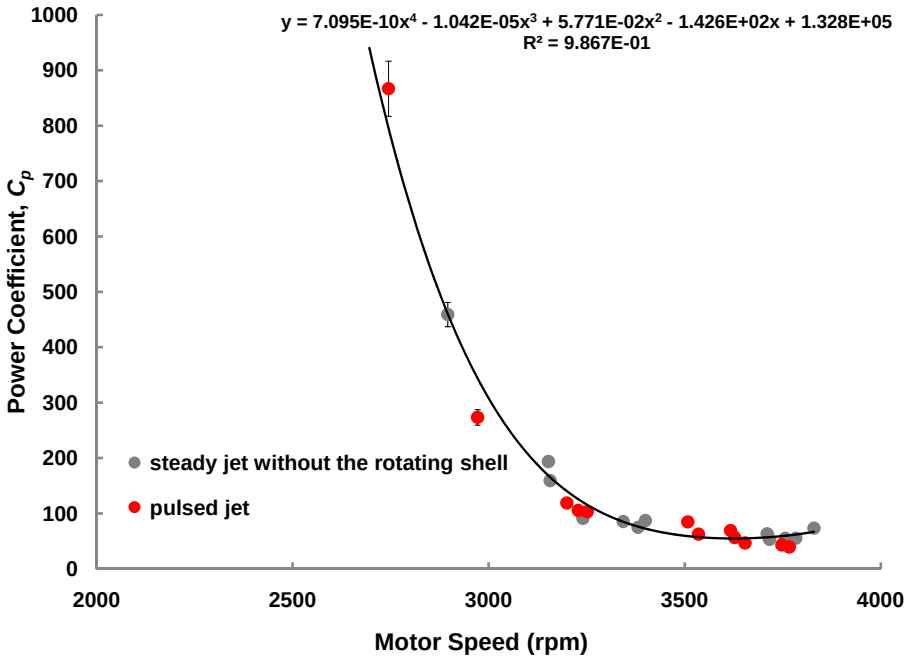

Figure 4.23. Graph of power coefficient versus motor speed illustrates increasing motor speed for both modes of propulsion results in a lower power coefficient.

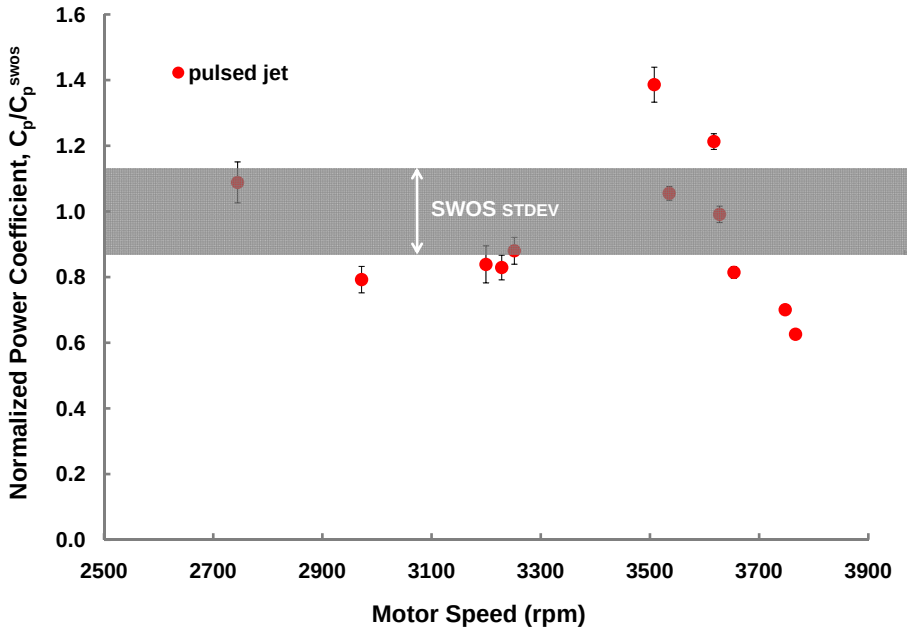

Figure 4.24. Graph of normalized power coefficient versus motor speed. Power coefficient of pulsed jet propulsion is equivalent or less than the steady jet power coefficient.

4.7 Conclusion

From the DPIV experiments, it was determined that an inner shell opening of 334^o was necessary to produce a pulsed jet with vortex ring formation for the studies with a Re_j equal to 5443 and a pulsing frequency of 2.5 Hz. This inner shell geometry was selected for the propulsive performance studies. From the PLIF experiments, it was evident that the wake of the pulsed jet was larger in size in comparison to the wake of the steady jet. This increase in wake size was attributed to the entrainment of the ambient fluid into the vortex during the vortex ring formation.

Two sets of propulsive performance studies were conducted using two distinct motors of the same model. The pulsed jet configuration had a 40% average increase in Froude efficiency at higher motor speeds when utilizing the initial motor. This increase dropped by 50% when the motor was replaced. This decrease in performance was shown to have resulted from the need to increase motor speed to obtain an equivalent jet speed as generated by the initial motor. This increase in motor speed led to a decrease in vortex ring formation time, and consequently, a decrease in the fluid impulse of the vortex. A model of the Froude efficiency versus vehicle speed was generated by supplying a value of 180 cm/s for U_{avg}, the expected maximum steady state jet velocity. Initial studies suggested that there may be further increases in the Froude efficiency at higher motor speeds. Due to mechanical failure of the initial motor used in the experiments, experiments were conducted at higher vehicle speeds using a second motor. With increased vehicle speed, the Froude efficiency reached a maximum value of 47% for the pulsed jet configuration. Information as to whether the Froude efficiency would continue to increase could not be determined from the data. Further higher speed experiments are necessary. It is important to note that as the body velocity approaches the jet velocity, the thrust approaches zero.

A second metric was used to measure the propulsive performance. The total hydrodynamic efficiency was measured for the two sets of experiments. The pulsed jet acquired a maximum total hydrodynamic efficiency of 54% at a motor speed of 2890 rpm with the initial motor. A further increase was measured for the total hydrodynamic efficiency for the second set of experiments, reaching a value 63% at a motor speed of 3770 rpm. Initial studies of motor speeds over 2800

rpm show a 57% increase in the total hydrodynamic efficiency of the pulsed jet in comparison to the steady jet. This increase in hydrodynamic efficiency dropped to 32% for the second set of experiments. The decrease in performance for the second motor can be attributed to a decrease in the vortex ring formation time.

The power consumed by the motor during propulsion was measured to determine if a trade-off exists between improved propulsive performance and power consumption. As the motor speed increased, the power coefficient significantly decreased for both modes of propulsion. Although the pulsed jet configuration utilizes additional power to rotate the planetary gear system, the enhanced thrust production leads typically to an equivalent or smaller power coefficient in comparison to the steady jet configuration without the rotating shell. The largest benefit with regard to reduced pulsed jet propulsion power cost is at the highest motor speeds. At these speeds, the normalized power coefficient was 37% less than the power coefficient for the steady jet propulsion configuration.

Chapter 5

Role of Entrainment and Added Mass in Propulsive Performance

5.1 Introduction

Results for the propulsive performance studies in chapter 4 show that increases in propulsive efficiency are generated for the vehicle in the pulsed jet mode of propulsion in comparison to the steady jet mode of propulsion. This chapter investigates the fluid mechanics that contribute to the increased propulsive performance. Section 5.2 describes the experimental procedures and conditions that existed during the laser Doppler velocimetry trials. Section 5.3 describes the relationship of nozzle-exit overpressure to the hydrodynamic impluse. Section 5.4 investigates the role of ambient fluid entrainment in a developing vortex as a potential source of increased propulsive performance. Jet velocity profiles were measured and presented in section 5.4.1 and are used to obtain a measure of the entrainment ratio discussed in section 5.4.2. Added mass effect is another potential source for increased propulsive performance. A model developed by Krueger (2001) is used in section 5.5 to determine the fraction of the total impulse imparted to the flow that is contributed by added mass. A model was developed in section 5.6 to investigate how the increase in total fluid impulse due to vortex ring formation relates to the propulsive efficiency. The model was applied in section 5.6 to estimate the propulsive efficiency for the pulsed jet configuration at three motor speeds.

5.2 Experimental Conditions

The ambient fluid entrainment into the jet was measured for two motor speeds in the steady jet configuration and three motor speeds in the pulsed jet configuration. To decrease the load on the motor, the steady jet experiments were conducted without the inner rotating shell. It was shown in chapter 4 that the behavior of the jet is similar for both the steady jet with and without the rotating shell. One series of steady jet experiments was conducted with a motor speed of 2900 ± 30 rpm, producing an average jet speed of 154 ± 38 cm/s and a Re_j of 69,950. Another set of experiments was conducted with a motor speed of 3160 ± 40 rpm, generating an average jet speed of 157 ± 38 cm/s and a Re_j of 71,400. In order to make accurate comparisons between both modes of propulsion, comparable motor speeds were obtained for the series of pulsed jet experiments. The first set of experiments were conducted at the lowest motor speed able to sustain steady vehicle speed. These pulsed jet experiments were conducted at a motor speed of 2750 ± 30 rpm, generating an average jet speed of 142 ± 30 cm/s and a Re_j of 64,400. The steady jet configuration was unable to maintain a constant body velocity at the corresponding motor speed, therefore, no steady jet experiments were available for comparison at the lowest motor speed. The second set of pulsed jet experiments were conducted at 2970 ± 30 rpm, producing an average jet speed of 149 ± 30 cm/s and a Re_j of 67,400. The last set of experiments were performed at a motor speed of 3200 ± 30 rpm, producing an average jet speed of 158 ± 32 cm/s.

Given that laser Doppler velocimetry provides a pointwise measurement of the jet speed, it was necessary to translate the measurement probe to obtain a velocity profile as illustrated in figure 5.1. Given that the jet is axisymmetric, the probe volume was programmed to obtain speed measurements of the axial component of the velocity starting at the jet center. Measurements where obtained in 2 mm increments moving in the x direction up to a distance of x/D = 1. See figure 5.1. The y position was kept constant and the z position was fixed at 0.5 inches away from the jet exit. Given the velocity range of the vehicle and the 30 m maximum vehicle translation distance in the facility, the velocity profile could not be captured in a single trial. An entire velocity profile was captured in 4 to 6 segments. Each segment consists of measuring the velocity at 3 to 6 radial positions.

Approximately 3 to 5 seconds of data was captured at each radial position. To reduce measurement noise and error, two to four trials were conducted for each segment of the velocity profile. The miniLDV is capable of measuring only a single component of velocity at a given instant in time. Due to this limitation, the probe was rotated by 90^o to obtain measurements of the speed in the x direction (i.e., radial velocity) and the procedure was repeated. Approximately 18 trials under the same experimental conditions, including motor speed and starting position, were necessary to complete the velocity profile for a given motor speed.

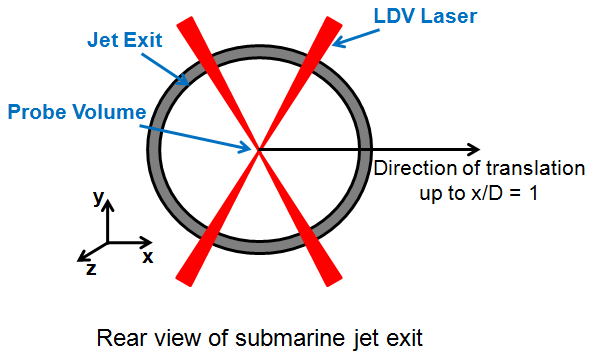

Figure 5.1. Schematic illustrating the translation of the LDV probe volume.

5.3 Relationship of Nozzle-Exit Overpressure to the Hydrodynamic Impulse

The total impulse in the flow, I(t), has been shown to increase by Krueger and Gharib (2003) with the presence of vortex ring formation due to nozzle-exit overpressure. The nozzle-exit overpressure is associated with the acceleration of the ambient fluid by vortex ring formation in the form of added mass and entrained mass. Through a control volume analysis of the fluid region external to the jet exit, it can be shown that the impulse injected into the flow by the jet is determined by a flux term and a contribution from overpressure as described in Krueger (2001), resulting in equation (5.1),

$$I(t) = I_U(t) + I_p(t), \tag{5.1}$$

where $I_U(t)$ is the total impulse due to the jet momentum flux and $I_p(t)$ is the pressure-impulse.

Krueger (2001) defines the total impulse of the flow, I(t), as the following,

$$I(t) = I_U(t) + I_p(t) = (m_{ejected} + m_{entrained} + M)W, \tag{5.2}$$

where $m_{ejected}$ is the mass of fluid that is ejected from the nozzle, $m_{entrained}$ is the mass of the ambient fluid entrained into the vortex ring, and the third component is the added mass of the vortex, M. These three classes of fluid move at the mean velocity of the vortex ring, W. A schematic of a fully developed vortex ring illustrating the three different masses of moving fluid is shown in figure 1.1. Krueger states that the momentum of the ejected fluid ($m_{ejected}\,W$) is derived from the jet momentum, I_U, and not from I_p. As a result, I_p is only associated with $(m_{entrained} + M)\,W$, and contributes only to the acceleration of ambient fluid in the form of added and entrained mass.

5.4 Relationship of Entrainment to Improved Propulsive Performance

As discussed in section 5.3, one benefit of vortex ring formation for propulsion is the entrainment of ambient fluid into the developing vortex ring. The entrained fluid must be accelerated with the vortex thus increasing the impulse supplied by the jet (Krueger and Gharib 2003). The velocity profile of the jet was measured in order to obtain an entrainment ratio. The entrainment ratio is defined by equation (5.3),

$$\frac{Q}{Q_o} \;=\; \frac{\int_0^{2\pi}\int_0^{r_o} U_z(r)dr\,d\theta}{U_{avg}\,A_j}, \tag{5.3}$$

where Q is the total volumetric flow rate defined by the integration under the blue and red curve illustrated in figure 5.2. Q_o is the volumetric flow rate through the jet exit and is represented by the integration under the blue curve simplifying to the product of U_{avg} and A_j. The entrainment ratio was calculated at two motor speeds in the steady jet configuration and three motor speeds in

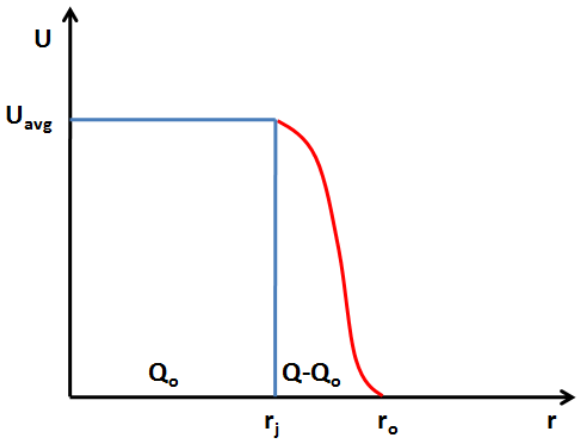

Figure 5.2. Entrainment ratio.

the pulsed jet configuration to investigate the role of entrainment.

5.4.1 Comparison of Velocity Profiles Obtained Using LDV

5.4.1.1 Comparison of Velocity Profiles for Uz

Figure 5.3 shows the axial velocity profiles for three motor speeds. The average axial velocity, U_z, was normalized by the average jet velocity, U_{avg}, and was plotted against a normalized distance x/r. A top hat profile was obtained for both the steady and pulsed jet modes of propulsion and for all motor speeds tested. For the given axial position of z/D = 0.25, these profiles are similar to the work of Reynolds et al. (2003) and Ho and Gutmark (1987). As the jet speed increases, the velocity outside the jet nozzle, x/r > 1.0, decreases rapidly to zero as noted by the smaller values of U_z/U_{avg} for both modes of propulsion. The magnitude of the velocity outside the jet is greater for the pulsed jet in comparison to the steady jet for a given equivalent jet speed suggesting greater fluid entrainment due to vortex ring formation.

The root-mean-square velocity fluctuation in U_z, w′, is normalized by U_{avg} and plotted against x/r in figure 5.4. The velocity fluctuations are greater inside the jet in comparison to the fluctuations in the free stream. Results from the pulsed jet experiments shown in figure 5.4(a) and figure 5.4(c) display two distinct peaks, one at x/r = 0.5 and the other near the jet exit of x/r = 1. The results

in figure 5.4(b) show a turbulent fluctuation peak near the jet exit for both the steady and unsteady modes of propulsion.

5.4.1.2 Comparison of Velocity Profiles for Ux

Figure 5.5 shows the velocity profiles of U_x for three motor speeds. The average velocity of U_x is normalized by the average jet velocity U_{avg} and plotted against a normalized distance of x/r. The magnitude of the velocity U_x is significantly lower than the magnitude of the velocity U_z. Approaching the jet exit, x/r $\rightarrow$ 1, U_x goes to zero and maintains a zero velocity within the jet. This decrease in the velocity of U_x is expected as the direction of jet thrust coincides with the z direction. With increasing motor speed, corresponding to an increase in body speed, the magnitude of U_x decreases. In the results for the second motor speed, figure 5.5(b), there are similarities in the velocity profile of U_x except for deviations after x/r $>$ 1.4. The normalized velocity of U_x sharply decreases to a value of 0.015 for the pulsed jet configuration whereas the normalized velocity of U_x gradually decreases to a value of 0.028 for the steady jet configuration. As the motor speed increases for the pulsed jet configuration, figure 5.5(c), U_x/U_{avg} maintains a relatively constant value of 0.011 for x/r $>$ 1. The normalized value of U_x is not constant for the steady jet configuration and reaches a maximum value of 0.025 for x/r = 1.1. In general, the magnitude of the normalized value of U_x was higher for the steady jet in comparison to the pulse jet. Note that the body speed achieved a higher magnitude for the pulsed jet in comparison to the steady jet with an equivalent jet speed. It is evident that with increased body speed, the magnitude of U_x decreases. The profile of U_x/U_{avg} obtained for the steady jet case in figure 5.5(b) is similar to the pulsed jet profile of U_x in figure 5.5(c). Both cases achieve comparable body speeds.

In figure 5.6, the root-mean-square velocity fluctuation in U_x, u$'$, is normalized by U_{avg} and is plotted against x/r. The velocity fluctuations are greater inside the jet in comparison to the fluctuations in the free stream. As the motor speed increases, there is a corresponding decrease in the velocity fluctuations outside the jet exit. The magnitude of the velocity fluctuations are on the order of the magnitude of the velocity of U_x.

5.4.2 Measurement of Entrainment Ratio for Both Steady and Unsteady Jet Propulsion with Equivalent Jet Speeds

To quantify the amount of entrained ambient fluid in the jet, the streamwise entrainment ratio was measured for both the steady and unsteady configuration. Figure 5.7 illustrates the relationship between the entrainment ratio and the motor speed. As the motor speed increases, there is a similar decrease in the entrainment ratio for both modes of propulsion. Krueger (2006) states that as the ratio of U_v/U_{avg} increases, the formation of the vortex ring process is preempted by the increased ring velocity as a result of convection from the coflow. This hampers the fluid entrainment into the vortex. The magnitude of the entrainment ratio is smaller for the steady jet mode of propulsion in comparison to the pulsed jet mode of propulsion for comparable motor speeds. The pulsed jet produces a 5.87% greater entrainment ratio at a motor speed of 2970 rpm over the steady jet at a motor speed of 2900 rpm. Although the pulsed and steady jet achieve a comparable jet speed at this motor speed, the measurement of the Froude efficiency for the pulsed jet was 26.13 and 6.58% higher than that of the steady jet. The increase in the total hydrodynamic efficiency for the pulsed jet was 11.2% when compared to the steady jet. This increase in propulsive performance supports the proposed benefits of increased ambient fluid entrainment due to vortex ring formation. A similar result was demonstrated at the higher motor speed. The pulsed jet produced a 5.22% greater entrainment ratio over the steady jet at an equivalent jet speed of 157 cm/s. The Froude efficiency was 6.45% higher for the pulsed jet configuration in comparison to the steady jet. The total efficiency measured was 10.79% higher for the pulsed jet configuration. The percentage difference in the measured entrainment ratio does not completely account for the difference in the measured propulsive efficiencies, however, only the benefits of increased entrainment at one particular z/d location have been taken into account. Table 5.1 summarizes the results obtained from the entrainment studies.

The measurement of the ambient fluid entrainment was obtained at only one axial position. As the vortex ring evolves and continues to roll up into a fully developed vortex ring, ambient fluid will continue to entrain into the vortex. The entrainment is constant in the far field of self-similar jets. In the near field, it must increase from zero at the nozzle to its final rate. Work supported

Table 5.1. Summary of entrainment studies for both pulsed and steady jet propulsion

Configuration	Motor Speed (rpm)	σ_{RPM}	U_{avg} (cm/s)	σ_{Uavg} (cm/s)	U_v (cm/s)	σ_{Uv} (cm/s)	η_{Froude} (%)	$\sigma_{\eta Froude}$ (%)	η_{Hydro} (%)	$\sigma_{\eta Hydro}$ (%)	Q_o (cm^3/s)	Q (cm^3/s)	Q / Q_o
Pulsed Jet	3200	29	158	30	32.8	5.0	34.4	6.47	43.16	7.28	2854.40	3186.31	1.12
	2970	28	149	30	22.3	4.8	26.13	5.58	31.42	6.71	2692.26	3041.99	1.13
	2750	29	142	32	13.9	5.1	17.81	5.36	20.04	6.73	2567.76	2944.18	1.15
Steady Jet Without Rotating Shell	3160	27	157	38	25.6	6.1	27.95	7.17	32.37	7.42	2848.06	2995.34	1.05
	2900	36	154	38	16.7	6.1	19.55	6.70	20.22	7.76	2790.70	3036.13	1.09

by Reynolds et al. (2003), Liepmann and Gharib (1992), and Ho and Gutmark (1987) indicate a monotonically increasing entrainment rate in the near field of the jet for values of z/d < 10. Further measures of the entrainment ratio at higher z/d ratios are necessary to determine if a similar trend exists in the pulsed jet vehicle. A further increase in the entrainment ratio for the pulsed jet over the steady jet may become evident. The added mass effect may also play a role in increasing propulsive performance. This concept will be discussed in section 5.5.

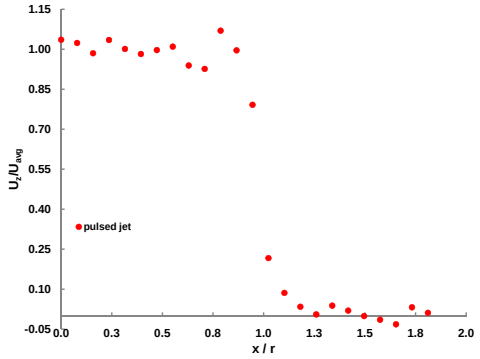

(a) Motor speed = 2750 rpm, U_{avg} = 142 cm/s.

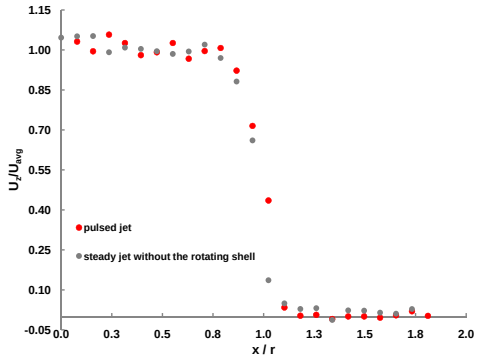

(b) Pulsed jet motor speed = 2970 rpm with U_{avg} = 149 cm/s, Steady jet motor speed = 2900 rpm with U_{avg} = 154 cm/s.

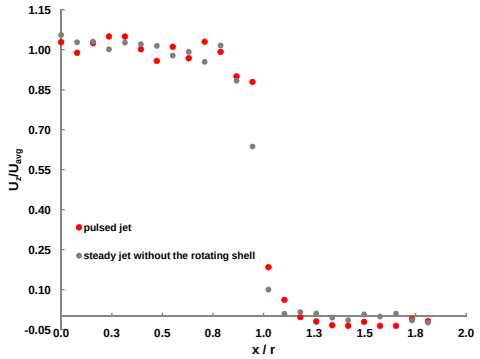

(c) Pulsed jet motor speed = 3200 rpm with U_{avg} = 158 cm/s, Steady jet motor speed = 3160 rpm with U_{avg} = 157 cm/s.

Figure 5.3. Variation of axial jet velocity U_z with translational distance in the x direction.

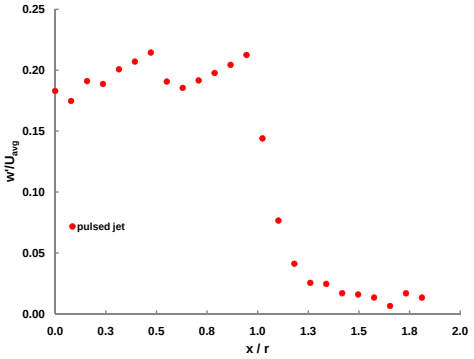

(a) Motor speed 2750 rpm, U_{avg} = 142 cm/s.

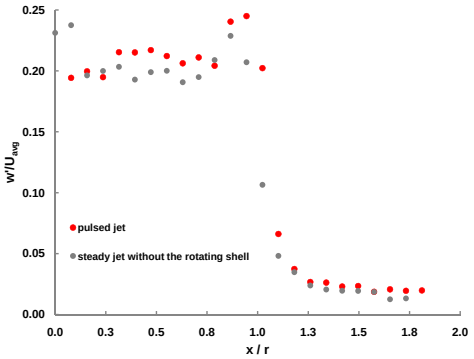

(b) Pulsed jet motor speed = 2970 rpm with U_{avg} = 149 cm/s, Steady jet motor speed = 2900 rpm with U_{avg} = 154 cm/s.

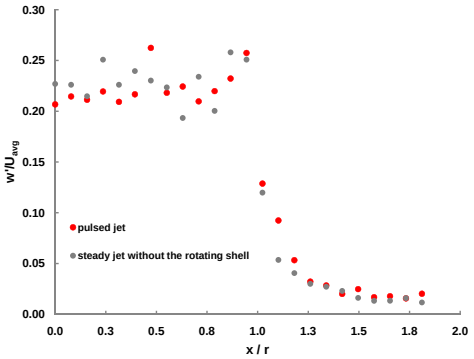

(c) Pulsed jet motor speed = 3200 rpm with U_{avg} = 158 cm/s, Steady jet motor speed = 3160 rpm with U_{avg} = 157 cm/s.

Figure 5.4. Variation of axial velocity fluctuations w′ with translational distance in the x direction.

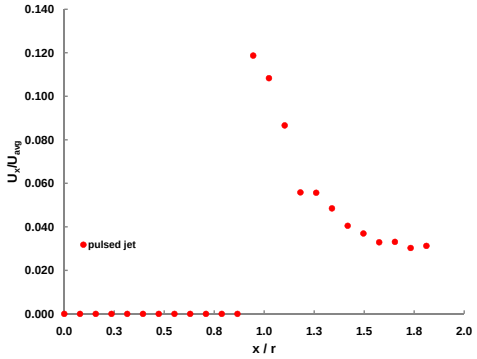

(a) Motor speed = 2750 rpm, U_{avg} = 142 cm/s.

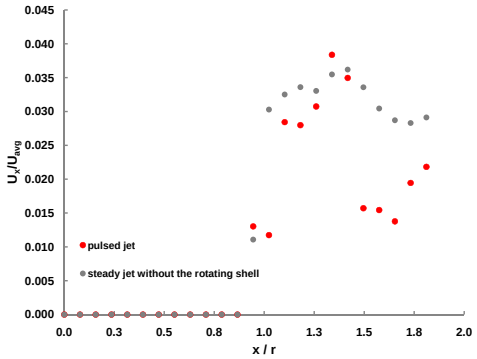

(b) Pulsed jet motor speed = 2970 rpm with U_{avg} = 149 cm/s, Steady jet motor speed = 2900 rpm with U_{avg} = 154 cm/s.

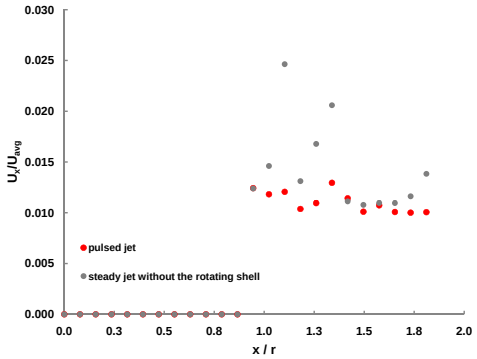

(c) Pulsed jet motor speed = 3200 rpm with U_{avg} = 158 cm/s, Steady jet motor speed = 3160 rpm with U_{avg} = 157 cm/s.

Figure 5.5. Variation of jet velocity U_x with translational distance in the x direction.

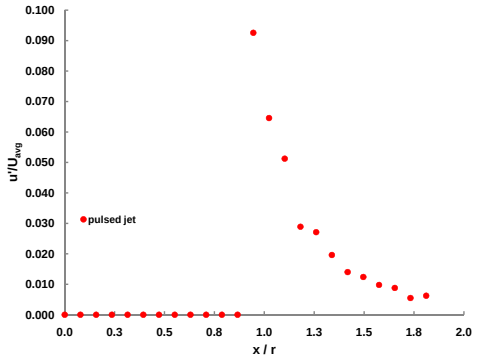

(a) Motor speed = 2750 rpm, U_{avg} = 142 cm/s.

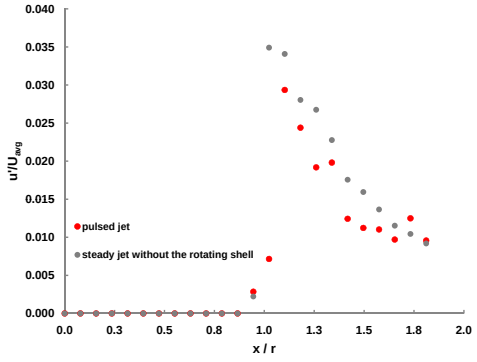

(b) Pulsed jet motor speed = 2970 rpm with U_{avg} = 149 cm/s, Steady jet motor speed = 2900 rpm with U_{avg} = 154 cm/s.

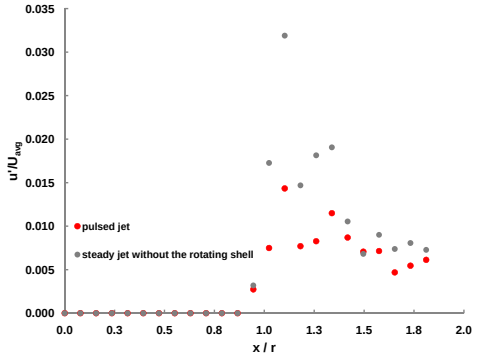

(c) Pulsed jet motor speed = 3200 rpm with U_{avg} = 158 cm/s, Steady jet motor speed = 3160 rpm with U_{avg} = 157 cm/s.

Figure 5.6. Variation of velocity fluctuations u′ with translational distance in the x direction.

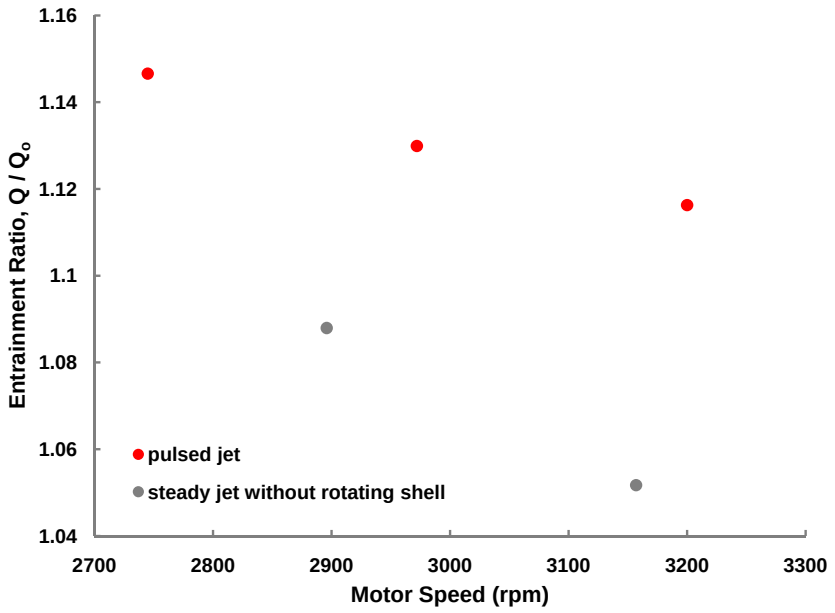

Figure 5.7. Relationship between entrainment ratio and motor speed.

5.5 Model of Proposed Contribution of Added Mass to Propulsive Performance

The second benefit of vortex ring formation for propulsion arises from the added mass effect which was described in section 5.3. In Krueger (2001), a model is presented for the initial stages of pulse ejection to determine an analytical evaluation of I_p. Added mass effects should dominate at the initiation of a pulse as the jet must initially push ambient fluid out of the way as it is ejected. The flow for x > 0 appears similar to the potential flow in front of a circular disk translating at a velocity U_{max} in the x direction. U_{max} is the maximum velocity of $U_J(t)$ over the interval of a pulse. The added mass associated with the flow in front of a circular disk is $m_{disk} = \frac{1}{6}\,\rho\,D^3$ (see section 6.10 of Batchelor (1967)). The impulse required to initiate the flow is given by equation (5.4).

$$I_p(t) \approx I_p(0) = m_{disk}\,U_{max} = \frac{1}{6}\,\rho\,D^3\,U_{max} \tag{5.4}$$

A few assumptions are made in determining an analytical solution for I_p. During the initial stage when the flow is being ejected from the nozzle, it appears more cylinder-like than ringlike for values of x/D << 1. The model ignores the roll up of the vortex ring and the unsteady component of the flow following the initiation of the jet. As a result of this assumption, entrainment is ignored along with the increasing effective diameter of the front of the slug. The model underestimates the contribution of pressure to $I_p(t)$ for t > 0.

To determine if the added mass effect associated with the acceleration of ambient fluid at the initiation of a starting jet can supply a substantial fraction of the pressure impulse, equation (5.4) was used to approximate the ratio $I(t)/I_p(t)$ for the three pulsed jet experiments that were conducted in the entrainment studies. The total impulse was calculated for the duration of a pulse and is defined by equation (5.5).

$$I \equiv \overline{T_p}\,t_p, \tag{5.5}$$

where $\overline{T_p}$ is the average thrust generated during a pulse. For steady state conditions, the thrust force is equivalent to the drag force, thus, the measure of $\overline{T_p}$ was obtained from the drag experiments as discussed in section 3.4.5. A summary of the results are displayed in table 5.2. As the motor speed increases, the ratio of $I_p(t)/I(t)$ slowly decreases as shown in figure 5.8. At the lowest motor speed, the estimated pressure impulse is 7% of the total impulse. This value decreases to 6.5% of the total impulse at the highest motor speed tested. The pressure impulse supplied to the flow due to the added mass effect provides an additional source for the increased proplusive performance that was observed in the pulsed jet mode of propulsion. Note that the estimated value obtained for $I_p(t)$ is an underestimate as the model does not account for the added mass effects associated with the change in the shape of the ring from a disc to an ellipsoid of larger diameter. The result demonstrates that the added mass effect associated with the acceleration of ambient fluid at the initiation of a starting jet provides an increase in the total impulse and is a source for increased propulsive performance.

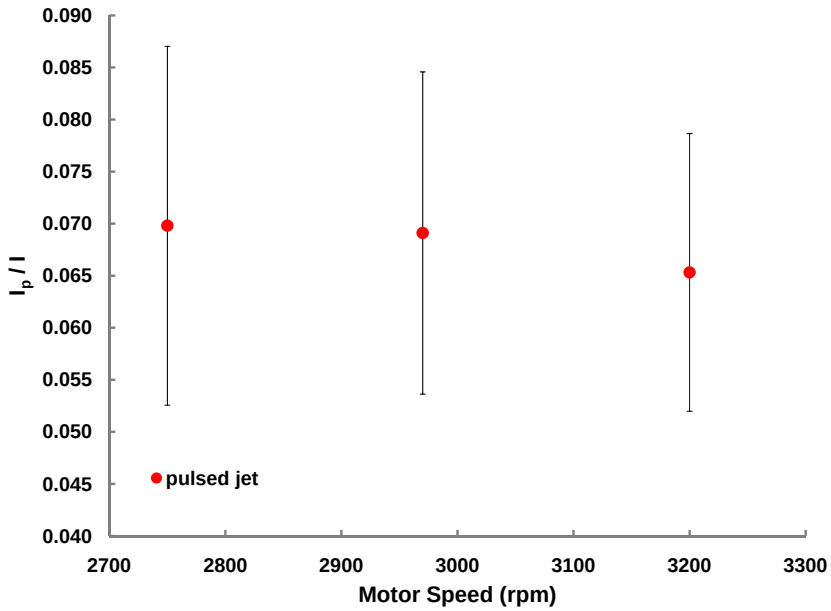

Figure 5.8. Relationship between $I_p(t)/I(t)$ and motor speed.

Table 5.2. Summary of parameters used in estimation of pressure impulse model

Configuration	Motor Speed (rpm)	U_{max} (cm/s)	U_v (cm/s)	t_p (s)	Drag (N)	I (Ns)	Model I_p (Ns)	I_p/I
Pulsed Jet	3200	162	32.77	0.09	5.77	0.541	0.035	0.065
	2970	157	22.33	0.10	4.92	0.496	0.034	0.069
	2750	149	13.87	0.11	4.25	0.465	0.032	0.070

5.6 Model of Proposed Contribution of Pressure Impulse to Propulsive Efficiency

Due to vortex ring formation, the additional acceleration of ambient fluid in the form of entrained and added mass results in an increase in the total fluid impulse. A model was developed to investigate how the increase in total fluid impulse relates to the propulsive efficiency. Recall that the total hydrodynamic efficiency as discussed in section 4.4.3 is equal to the following.

$$\eta_{hydro} = \frac{T\,U_v}{T\,U_v \;+\; \frac{1}{2}\rho\,A_j\,U_{avg}\,(U_{avg} - U_v)^2} \tag{5.6}$$

Provided that the system is traveling at steady state, the thrust produced by the system is equivalent to the drag. As discussed in section 5.5, the total impulse for the duration of a pulse is equal to the product of the average thrust generated during a pulse, $\overline{T_p}$, and the pulse duration, t_p. As shown in section 5.3, the total impulse can also be written as equation (5.2). Equating these two expressions and solving for $\overline{T_p}$, the following equation is obtained.

$$\overline{T_p} = \frac{W}{t_p}(m_{ejected} + m_{entrained} + M) \tag{5.7}$$

Equation (5.7) can be further broken down. The mass of fluid ejected from the nozzle during the pulse duration, $m_{ejected}$, is equal to $t_p\,\rho\,A_j\,U_{avg}$. The mass entrained into the developing vortex ring, can be approximated as $t_p\,\rho\,Q_{avg}$. The average measurement of the volumetric flow rate (Q_{avg})

during the pulse duration is used to prevent on overestimate of the contribution of $m_{entrained}$ to $\overline{T_p}$ given that the mass of the entrained fluid increases over the pulse duration. The added mass of the vortex ring, M, is approximated as the product of the added mass coefficient of the fully developed vortex ring, C_{AM}, and the total mass the vortex ring, $(m_{ejected} + m_{entrained})$. This approximation leads to an overestimate of the added mass force as the model does not account for the added mass effects associated with the change in the shape of the ring from a disc to an ellipsoid of larger diameter. At early stages, for values of z/D << 1, the jet initially appears similar to a disk with a diameter approximately equal to the jet exit diameter, Krueger (2001). As the vortex grows and develops into a fully developed vortex ring, the shape of the vortex becomes ellipsoidal and the added mass is increased. The added mass coefficient of an ellipsoid can be found in Milne-Thomson (1960). Krueger et al. (2006) cites that the vortex ring velocity, W, in the presence of uniform background coflow, can be approximated by equation (5.8). In this experiment, the coflow is generated by the motion of the vehicle, U_v.

$$W \approx \frac{1}{2}\left(U_{avg} + U_v\right) \tag{5.8}$$

This vortex ring velocity expression ignores the effect of the overpressure at the nozzle exit plane developed during the unsteady ring formation process but still provides a reasonable approximation (Krueger et al. 2006).

Taking the approximations for $m_{ejected}$, $m_{entrained}$, and W and plugging their results into equation (5.7), the following equation is generated.

$$\overline{T_p} = \frac{1}{2}\left(U_{avg} + U_v\right)\left[\left(\rho\, A_j\, U_{avg} + \rho\, Q_{avg}\right)\left(1 + C_{AM}\right)\right] \tag{5.9}$$

Taking the result developed for $\overline{T_p}$ in equation (5.9) and substituting into equation (5.6) for T, the following definition for propulsive efficiency is developed.

$$\eta_{model} = \frac{\frac{U_v}{2}\,(U_{avg}+U_v)\,[(\rho\,A_j\,U_{avg}+\rho\,Q_{avg})\,(1+C_{AM})]}{\frac{U_v}{2}\,(U_{avg}+U_v)\,[(\rho\,A_j\,U_{avg}+\rho\,Q_{avg})\,(1+C_{AM})]\;+\;\frac{1}{2}\rho\,A_j\,U_{avg}\,(U_{avg}-U_v)^2} \tag{5.10}$$

This metric for propulsive efficiency clearly establishes a relationship between the propulsive efficiency, ambient fluid entrainment and added mass.

5.6.1 Measurement of Propulsive Efficiency Using Estimated Total Impulse

The model was applied to estimate the propulsive efficiency for the pulsed jet configuration at the three motor speeds described in 5.2. Since the measurement of the ambient fluid entrainment was obtained at only one axial position, z/r = 0.5, the value of Q_{avg} was estimated using a linear fit. In previous work, Reynolds et al. (2003), Liepmann and Gharib (1992), and Ho and Gutmark (1987), the mass of the entrained fluid into the vortex has been shown to approximately equal zero at the nozzle exit and increase linearly as the vortex develops and moves downstream for values of z/d < 10. A linear curve fit for the ratio of $Q_{entrained}/Q_o$ versus downstream distance was developed. $Q_{entrained}$ is the volumetric flow rate of the entrained flow into the wake and is calculated by subtracting Q_o from Q.

To calculate Q_{avg}, the position of the vortex ring at the end of the pulse duration (z_{tp}) is required and was estimated by $z_{tp} \approx W\,t_p$. The value of z_{tp}/r is substituted into the corresponding equation based on motor speed as shown in figure 5.9 and is used to estimate the ratio of $Q_{entrained}/Q_o$ at the end of the pulse duration. The value of Q_{avg} is estimated as $Q_{entrained}/2$ given the linear relationship between $Q_{entrained}/Q_o$ and downstream distance. The results for the measurement of Q_{avg}, W and t_p are summarized in Appendix F.

Substituting for Q_{avg} in equation 5.10, equation 5.11 is obtained.

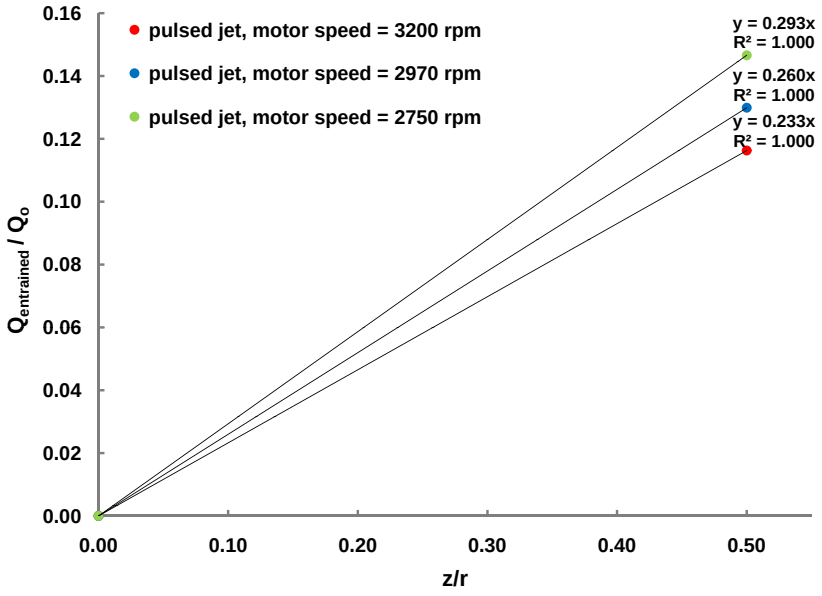

Figure 5.9. Plot of ambient fluid entrainment as a function of downstream distance for three motor speeds.

$$\eta_{model} = \frac{\frac{U_v}{2}\,(U_{avg}+U_v)\,[(\rho\,A_j\,U_{avg}+\rho\,\frac{Q_{entrained}}{2})\,(1+C_{AM})]}{\frac{U_v}{2}\,(U_{avg}+U_v)\,[(\rho\,A_j\,U_{avg}+\rho\,\frac{Q_{entrained}}{2})\,(1+C_{AM})]\;+\;\frac{1}{2}\rho\,A_j\,U_{avg}\,(U_{avg}-U_v)^2} \tag{5.11}$$

The first step in estimating C_{AM} was to calculate the formation time. Given that the geometry of the vortex ring during development is unknown, C_{AM} was estimated indirectly using data of vortex ring geometry from PLIF experiments in Krueger (2001) and from DPIV experiments obtained from Shadden et al. (2007). Supporting data for vortex rings of a comparable formation time was used to estimate the geometry of the fully developed vortex ring. The formation time was approximately 3 for all motor speeds. The vortex ring geometry was estimated using the formation time and C_{AM} was calculated using the added-mass coefficient of an ellipsoid (Milne-Thomson 1960) and found to be 0.72. Using the value of C_{AM} for a fully developed vortex leads to an overestimate in the measurement of the added mass for the duration of the pulse and consequently an overestimate

in $\overline{T_p}$. Due to the unavailability of vortex ring geometry data at a corresponding coflow velocity ratio (U_{avg}/Uv) and formation time, the geometry of the vortex was determined from previous experiments without the presence of a coflow velocity. Krueger et al. (2006) states that the vortex ring formation process is preempted by the increased ring velocity as a result of convection from the coflow, thereby decreasing the size of the vortex ring in comparison to the case without the presence of the coflow. This result of a decrease in vortex ring size due to the presence of the coflow has not be taken into account in the estimate of C_{AM} and may also lead to a further overestimate in $\overline{T_p}$.

The results for estimated propulsive efficiency obtained using equation (5.11) for the three motor speeds are found in Appendix F. The model is sensitive to the value of C_{AM}. Initially the value of C_{AM} was estimated to be the value for a fully developed vortex which led to a higher value of η_{hydro} modeled in comparison to the experimental value of η_{hydro}, see figure 5.10. At the early stages of vortex ring formation the flow being ejected from the nozzle appears more cylinder like than ring like. Choosing a value of C_{AM} for a circular disk, leads to a lower value of η_{hydro} modeled in comparison to the experimental value of η_{hydro}. Using the estimated value of C_{AM} as the shape of a fully developed vortex ring and the shape of a circular disk bound the experimental measurement of η_{hydro}. These results justify the increase in propulsive efficiency for the pulsed jet configuration in comparison to the steady jet configuration due to the increase in thrust production generated by entrained and added mass forces developed during vortex ring formation. Provided that the values of Q_{avg} and C_{AM} can be estimated, this model serves as another metric for determining the propulsive efficiency of a system. It should be noted that as motor speed increases, the ratio of $I_p(t)/I(t)$ slowly decreases as shown in figure 5.8, therefore contributing less to the generation of overpressure at the nozzle exit. An eventual decrease in the overpressure due to increased motor speed will decrease the amount of useful work provided for propulsion and may exhibit a propulsive efficiency comparable to the steady jet configuration. As motor speed increases, the time between fluid pulses decreases, leading to increased vortex interactions. Krueger (2005) has shown that increasing pulsing duty cycle increases the vorticity from preceding pulses near the nozzle at the ejection of each pulse. This behavior requires less fluid to be accelerated by the issuing pulse and

reduces nozzle exit overpressure.

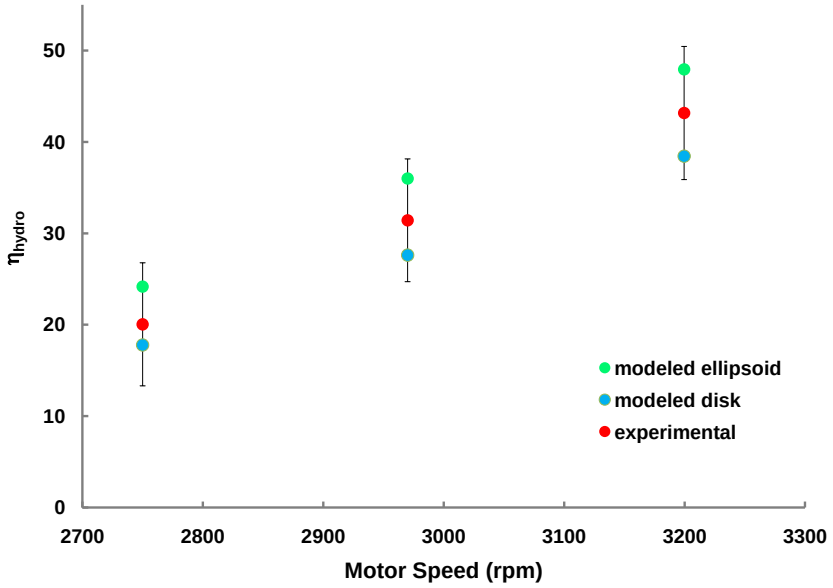

Figure 5.10. Illustration of accuracy of model in estimating propulsive efficiency.

5.7 Conclusion

This chapter discussed the potential sources that contributed to increased propulsive performance. Analysis demonstrates that the acceleration of two classes of ambient fluid can led to an increase in propulsive performance. The first source of ambient fluid acceleration investigated was that of entrained mass that is inducted into the body of the ring as the shear layer rolls up and is convected downstream with the ring. To quantify the amount of entrained ambient fluid into the jet, the streamwise entrainment ratio was measured for both the steady and unsteady jet. The entrainment ratio was measured for two motor speeds in the steady jet configuration and three motor speeds in the pulsed jet configuration. To obtain a measurement of the entrainment ratio, the velocity profile of the jet was measured. The axial jet velocity profiles were similar to a top hat for both the steady

and pulsed jet modes of propulsion and for all motor speeds tested. These profiles are similar to the work of Reynolds et al. (2003) and Ho and Gutmark (1987). The magnitude of the velocity outside the jet was greater for the pulsed jet in comparison to the steady jet for a given equivalent jet speed suggesting increased fluid entrainment due to vortex ring formation.

The velocity profiles for U_x were also measured for three different motor speeds. The magnitude of the velocity U_x is significantly lower than the magnitude of the velocity U_z. As x/r approaches the jet exit, the value of U_x went to zero and maintained a zero velocity within the jet. The decrease in the velocity of U_x was expected as the direction of jet thrust coincided with the z direction. With increasing motor speed and a corresponding increase in body speed, the magnitude of U_x was shown to decrease. In general, the magnitude of the normalized value of U_x was higher for the steady jet in comparison to the pulsed jet. This result may be attributed to the pulsed jet configuration acquiring a higher body speed in comparison to the steady jet configuration with an equivalent jet speed. The root-mean-square velocity fluctuation in U_x, u$'$, was also calculated. The velocity fluctuations were shown to be greater inside the jet in comparison to the fluctuations in the free stream. As the motor speed increased, there was a corresponding decrease in the velocity fluctuations outside the jet exit. The magnitude of the velocity fluctuations were on the order of the magnitude of the velocity U_x.

The measured streamwise entrainment ratio was shown to decrease with increased motor speed for both modes of propulsion. The magnitude of the entrainment ratio was smaller for the steady jet mode of propulsion in comparison to the pulsed jet mode of propulsion at comparable motor speeds. The pulsed jet produced a 5.87% greater entrainment ratio at a motor speed of 2972 rpm over the steady jet at a motor speed of 2896 rpm. Despite both configurations achieving comparable jet speeds at this motor speed, the measured Froude efficiency for the pulsed jet was 26.13 and 6.58% higher in comparison to the steady jet. The increase in the total hydrodynamic efficiency for the pulsed jet was 11.2% over the steady jet. A similar result was demonstrated at the higher motor speed. The percentage difference in the measured entrainment ratio does not completely account for the difference in the measured propulsive efficiencies. However, only the benefit of increased entrainment at one z/d location has been measured and taken into account. A further increase

in the entrainment ratio for the pulsed jet compared to the steady jet may be evident at higher z/d ratios. Work supported by Reynolds et al. (2003), Liepmann and Gharib (1992), and Ho and Gutmark (1987) indicate a monotonically increasing entrainment ratio in the near field of the jet for values of z/d < 10. Further measures of the entrainment ratio at higher z/d ratios are necessary to determine if a similar trend exists with the pulsed jet vehicle.

The role of the added mass effect was investigated for the purpose of increasing propulsive performance. The total impulse in the flow was shown to increase with the presence of vortex ring formation due to nozzle-exit overpressure. A model developed by Krueger (2001) is used to determine the fraction of the total impulse imparted to the flow that is contributed to by added mass. As the motor speed increased, the ratio of $I_p(t)/I(t)$ slowly decreased. At the lowest motor speed, the estimated pressure impulse was 7% of the total impulse and decreased to 6.5% of the total impulse at the highest motor speed. The result demonstrates that the added mass effect associated with the acceleration of ambient fluid at the initiation of a starting jet provides an increase in the total impulse and is thus a source for increased propulsive performance.

A metric for propulsive efficiency was developed to demonstrate the relationship between the propulsive efficiency, ambient fluid entrainment and added mass. The model is sensitive to the value of C_{AM}. Initially the value of C_{AM} was estimated to be the value for a fully developed vortex which led to a higher value of η_{hydro} modeled in comparison to the experimental value of η_{hydro}. Using the estimated value of C_{AM} as the shape of a fully developed vortex ring and the shape of a circular disk bound the experimental measurement of η_{hydro}. These results justify the increased propulsive efficiency of the pulsed jet configuration in comparison to the steady jet configuration due to increased thrust production generated by the entrained and added mass force developed during vortex ring formation. Providing that the values of Q_{avg} and C_{AM} can be estimated, this model serves as another metric for determining the propulsive efficiency of a system. It should be noted that as motor speed increases, the ratio of $I_p(t)/I(t)$ slowly decreases, therefore contributing less to the generation of overpressure at the nozzle exit. An eventual decrease in the overpressure due to increased motor speed will decrease the amount of useful work provided for propulsion and may

exhibit a propulsive efficiency comparable to the steady jet configuration. As motor speed increases, the time between fluid pulses decreases, leading to increased vortex interactions. Krueger (2005) has shown that increasing pulsing duty cycle increases the vorticity from preceding pulses near the nozzle at the ejection of each pulse. This behavior requires less fluid to be accelerated by the issuing pulse and reduces nozzle exit overpressure.

Chapter 6

Summary and Recommendations

6.1 Summary of Results

This research provides for a direct, empirical comparison between biological and engineering propulsion systems. An underwater vehicle was designed with the capability to produce either a steady or an unsteady jet for propulsion while maintaining the same η_{mech}, therefore allowing for an accurate comparison of the propulsive performance. It was shown that using conventional screw-based propulsion, it was not necessary to mimic the geometry and kinematics of swimming animals in order to replicate their performance provided that similar wake dynamics are generated by propulsion.

From DPIV experiments, it was reestablished that a sufficient formation time, $t^* > 0.4$, was necessary to produced isolated vortex rings. An inner shell opening of 334^o was necessary to produce a pulsed jet with vortex ring formation for the studies with a Re_j equal to 5443 and a pulsing frequency of 2.47 Hz. This inner shell geometry was selected for the propulsive performance studies. From the PLIF experiments, it was evident that the wake of the pulsed jet was larger in size in comparison to the wake of the steady jet. This increase in wake size was attributed to the entrainment of the ambient fluid into the vortex during the vortex ring formation.

Two sets of propulsive performance studies were conducted using two distinct motors of the same model. The studies were conducted using a vehicle capable of self-propulsion down a 40 m water tunnel facility. The pulsed jet configuration had a 40% average increase in Froude efficiency at higher motor speeds when utilizing the initial motor. This increase dropped by 50% when the motor was

replaced due to mechanical failure. This decrease in performance resulted from the need to increase motor speed to obtain an equivalent jet speed as generated by the initial motor. This increase in motor speed led to a decrease in vortex ring formation time and, consequently, a decrease in the fluid impulse of the vortex. A model of the Froude efficiency versus vehicle speed was generated by supplying a value of 180 cm/s for U_{avg}, the expected maximum steady state jet velocity. Initial studies suggested that there may be further increases in the Froude efficiency at higher motor speeds. Experiments were conducted at higher vehicle speeds using the second motor. With increased vehicle speed, the Froude efficiency reached a maximum value of 47% for the pulsed jet configuration. This resulting Froude efficiency is close to what has been measured for biological organisms. Information as to whether the Froude efficiency would continue to increase could not be determined from the data. Further higher speed experiments are necessary.

A second metric was used to measure the propulsive performance. The total hydrodynamic efficiency was measured for the two sets of experiments. The pulsed jet acquired a maximum total hydrodynamic efficiency of 54% at a motor speed of 2887 rpm with the initial motor. A further increased total hydrodynamic efficiency was measured for the second set of experiments, reaching a value of 63% at a motor speed of 3767 rpm. Initial studies of motor speeds over 2800 rpm show a 57% increase in the total hydrodynamic efficiency of the pulsed jet in comparison to the steady jet. This increase in hydrodynamic efficiency dropped to 32% for the second set of experiments. The decrease in performance for the second motor can be attributed to a decease in the vortex ring formation time.

To determine if a trade-off exists between improved propulsive performance and power consumption, the power consumed by the motor during propulsion was measured. As the motor speed increased, the power coefficient significantly decreased for both modes of propulsion. Although the pulsed jet configuration utilizes additional power to rotate the planetary gear system, the enhanced thrust production lead to an equivalent or smaller power coefficient in comparison to the steady jet configuration using the rotating shell with the exception of two data points. The largest benefit with regard to pulsed jet propulsion power cost is at the highest motor speeds. At these speeds, the

normalized power coefficient was 37% less than the power coefficient for the steady jet propulsion configuration.

Analysis demonstrated that the acceleration of two classes of ambient fluid led to an increase in propulsive performance. The first source of ambient fluid acceleration investigated was the entrained mass that was inducted into the body of the ring and convected downstream with the ring. To quantify the amount of entrained ambient fluid into the jet, the streamwise entrainment ratio was measured for both the steady and unsteady jet. The entrainment ratio was measured for two motor speeds in the steady jet configuration and three motor speeds in the pulsed jet configuration. To obtain a measurement of the entrainment ratio, the velocity profile of the jet was measured. The axial jet velocity profiles were shaped similar to a top hat for both the steady and pulsed jet modes of propulsion and for all motor speeds tested. These profiles are similar to the work of Reynolds et al. (2003) and Ho and Gutmark (1987). The magnitude of the velocity outside the jet was greater for the pulsed jet in comparison to the steady jet for a given equivalent jet speed suggesting increased fluid entrainment due to vortex ring formation.

The velocity profiles for U_x were also measured for three different motor speeds. The magnitude of the velocity U_x was significantly lower than the magnitude of the velocity U_z. As x/r approaches the jet exit, the value of U_x went to zero and maintained a zero velocity within the jet. The decrease in the velocity of U_x was expected as the direction of jet thrust coincided with the z direction. With increasing motor speed and a corresponding increase in body speed, the magnitude of U_x was shown to decrease. In general, the magnitude of the normalized value of U_x was higher for the steady jet in comparison to the pulsed jet. This result may be attributed to the pulsed jet configuration acquiring a higher body speed in comparison to the steady jet configuration with an equivalent jet speed. The root mean square velocity fluctuation in U_x, u$'$, was also calculated. The velocity fluctuations were shown to be greater inside the jet in comparison to the fluctuations in the free stream. As the motor speed increased, there was a corresponding decrease in the velocity fluctuations outside the jet exit. The magnitude of the velocity fluctuations were on the order of the magnitude of the velocity U_x.

The measured streamwise entrainment ratio was shown to decrease with increased motor speed

for both modes of propulsion. The magnitude of the entrainment ratio was smaller for the steady jet mode of propulsion in comparison to the pulsed jet mode of propulsion at comparable motor speeds. The pulsed jet produced a 5.87% greater entrainment ratio at a motor speed of 2972 rpm over the steady jet at a motor speed of 2896 rpm. Despite both configurations achieving comparable jet speeds at this motor speed, the measured Froude efficiency for the pulsed jet was 26.13 and 6.58% higher in comparison to the steady jet. The increase in the total hydrodynamic efficiency for the pulsed jet was 11.2% over the steady jet. A similar result was demonstrated at the higher motor speed. The percent difference in the measured entrainment ratio does not completely account for the difference in the measured propulsive efficiencies. However, only the benefit of increased entrainment at one z/d location has been measured and taken into account. A further increase in the entrainment ratio for the pulsed jet compared to the steady jet may be evident at higher z/d ratios. Work supported by Reynolds et al. (2003), Liepmann and Gharib (1992), and Ho and Gutmark (1987) indicate a monotonicly increasing entrainment ratio in the near field of the jet for values of $z/d < 10$. Further measures of the entrainment ratio at higher z/d ratios are necessary to determine if a similar trend exists with the pulsed jet vehicle.

The role of the added mass effect was investigated for the purpose of increasing propulsive performance. The total impulse in the flow was shown to increase with the presence of vortex ring formation due to nozzle-exit overpressure. A model developed by Krueger (2001) was used to determine the fraction of the total impulse imparted to the flow that was contributed by the added mass effect. As the motor speed increased, the ratio of $I_p(t)/I(t)$ slowly decreased. At the lowest motor speed, the estimated pressure impulse was 7% of the total impulse and decreased to 6.5% of the total impulse at the highest motor speed. The result demonstrates that the added mass effect associated with the acceleration of ambient fluid at the initiation of a starting jet provides an increase in the total impulse, and is thus a source for increased propulsive performance.

A metric for propulsive efficiency was developed to demonstrate the relationship between the propulsive efficiency, ambient fluid entrainment and added mass. The model is sensitive to the value of C_{AM}. Choosing a value of C_{AM} for a circular disk, leads to a lower value of η_{hydro} modeled in

comparison to the experimental value of η_{hydro}. Using the estimated value of C_{AM} as the shape of a fully developed vortex ring and the shape of a circular disk bound the experimental measurement of η_{hydro}. These results justify the increase in propulsive efficiency for the pulsed jet configuration in comparison to the steady jet configuration due to the increase in thrust production generated by entrained and added mass forces developed during vortex ring formation. Provided that the values of Q_{avg} and C_{AM} can be estimated, this model serves as another metric for determining the propulsive efficiency of a system. It should be noted that as motor speed increases, the ratio of $I_p(t)/I(t)$ slowly decreases, therefore contributing less to the generation of overpressure at the nozzle exit. An eventual decrease in the overpressure due to increased motor speed will decrease the amount of useful work provided for propulsion and may exhibit a propulsive efficiency comparable to the steady jet configuration. As motor speed increases, the time between fluid pulses decreases, leading to increased vortex interactions. Krueger (2005) has shown that increasing pulsing duty cycle increases the vorticity from preceding pulses near the nozzle at the ejection of each pulse. This behavior requires less fluid to be accelerated by the issuing pulse and reduces nozzle exit overpressure.

6.2 Recommendations for Future Work

Given that the research has shown that the propulsive performance of pulsed jet propulsion was superior to steady jet propulsion, particularly at higher vehicle speeds, modifications in the design of the vehicle may further enhance performance. The increase in propulsive performance was attributed to the presence of nozzle-exit overpressure due to vortex ring formation. The nozzle-exit overpressure is associated with the acceleration of the ambient fluid by vortex ring formation in the form of added mass and entrained mass. Further enhancements of propulsive performance due to increased fluid entrainment may be possible through modification of the jet exit geometry. Work by Ho and Gutmark (1987), Husain and Hussain (1991), and Husain and Hussain (1993) discovered increased fluid entrainment in elliptic jets in comparison to circular jets.

For simplicity in design, the inner rotating shell for the pulse jet configuration was geared to the

propeller shaft. This design feature prevented the rotation rate of the inner shell to be set independently of the rotation rate of the propeller. As a result of this limitation, the vortex ring formation time was also dependent on the rotation rate of the propeller. It would be of interest to modify the design of the gear train to allow for variability of the inner shell rotation, and consequently, variability in the vortex ring formation time. Krueger and Gharib (2003) have shown that the total impulse follows a generally increasing trend with formation time until the leading vortex develops a trailing jet or is said to have been pinched off. Typically vortex ring pinch off occurs at a formation time between 3 and 4 (Gharib et al. 1998). It was shown in section 4.4 that there was an increase in propulsive performance attributed to an increase in the vortex ring formation time. It would be worthwhile to investigate if further enhancement in propulsive performance is attainable at higher values in the vortex ring formation time for all motor speeds.

It was apparent in section 4.4.2 that a further increase in propulsive efficiency may be possible at higher motor speeds. Due to power restrictions on the motor, higher speeds were unattainable. A significant amount of energy is also expended due to friction on the flume rails (section 3.4.5). A replacement of the roller bearing system with an air bearing system would conserve energy that would otherwise be dissipated by friction. Unfortunately, due to the 40 m length of the flume rails, the replacement of the roller bearing system is prohibitively expensive.

One objective of the research was to make an accurate comparison between the propulsive performance of pulsed jet and steady jet propulsion. The vehicle was designed to produce both modes of propulsion while maintaining the same mechanical efficiency thus allowing for an accurate comparison of the overall efficiency (η_o). Having shown that pulsed jet propulsion improves propulsive efficiency in comparison to steady jet propulsion, other mechanisms of pulsed jet generation may be explored to possibly further enhance performance and overall efficiency.

Appendix A

Submarine DAQ Implementation Details

Figure A.1 is the execution flow chart for the Submarine DAQ application.

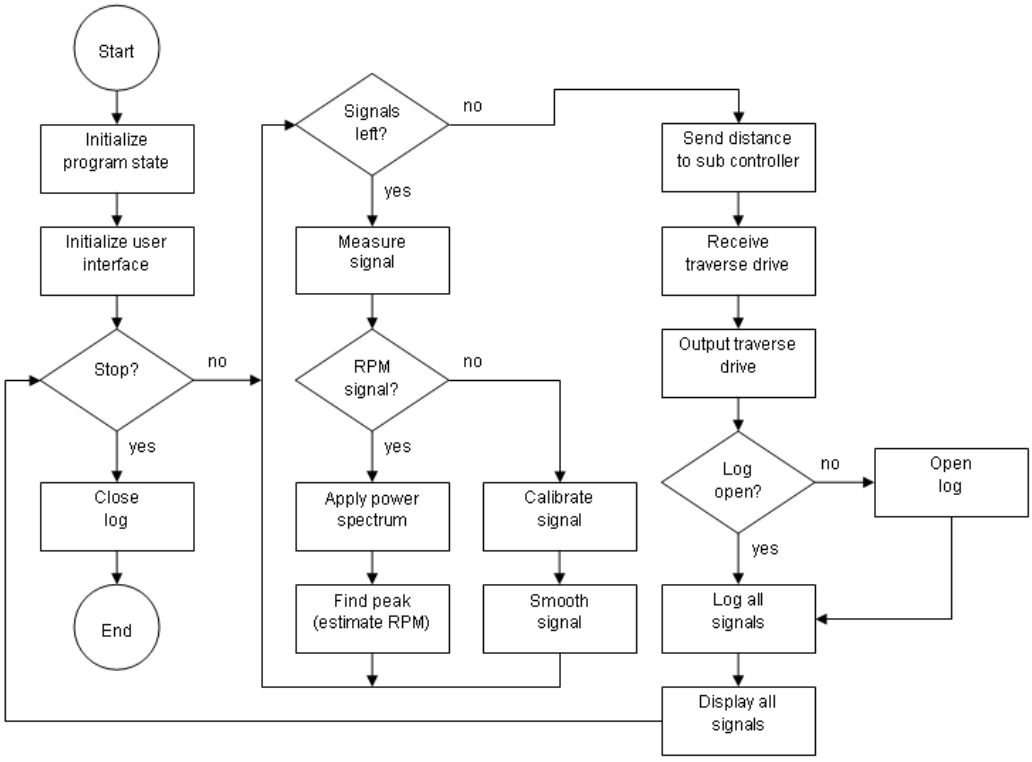

Figure A.1. Submarine DAQ flow chart.

Several portions of the Submarine DAQ LabVIEW implementation are provided for reference. Figure A.2 demonstrates how the NI DAQ Assistant is used to read several telemetry channels.

Figure A.3 demonstrates how each telemetry channel is processed. Figure A.4 demonstrates how the motorized traverse control signal is output using the NI DAQ Assistant. Figure A.5 and figure A.6 demonstrate how telemetry is logged and displayed respectively.

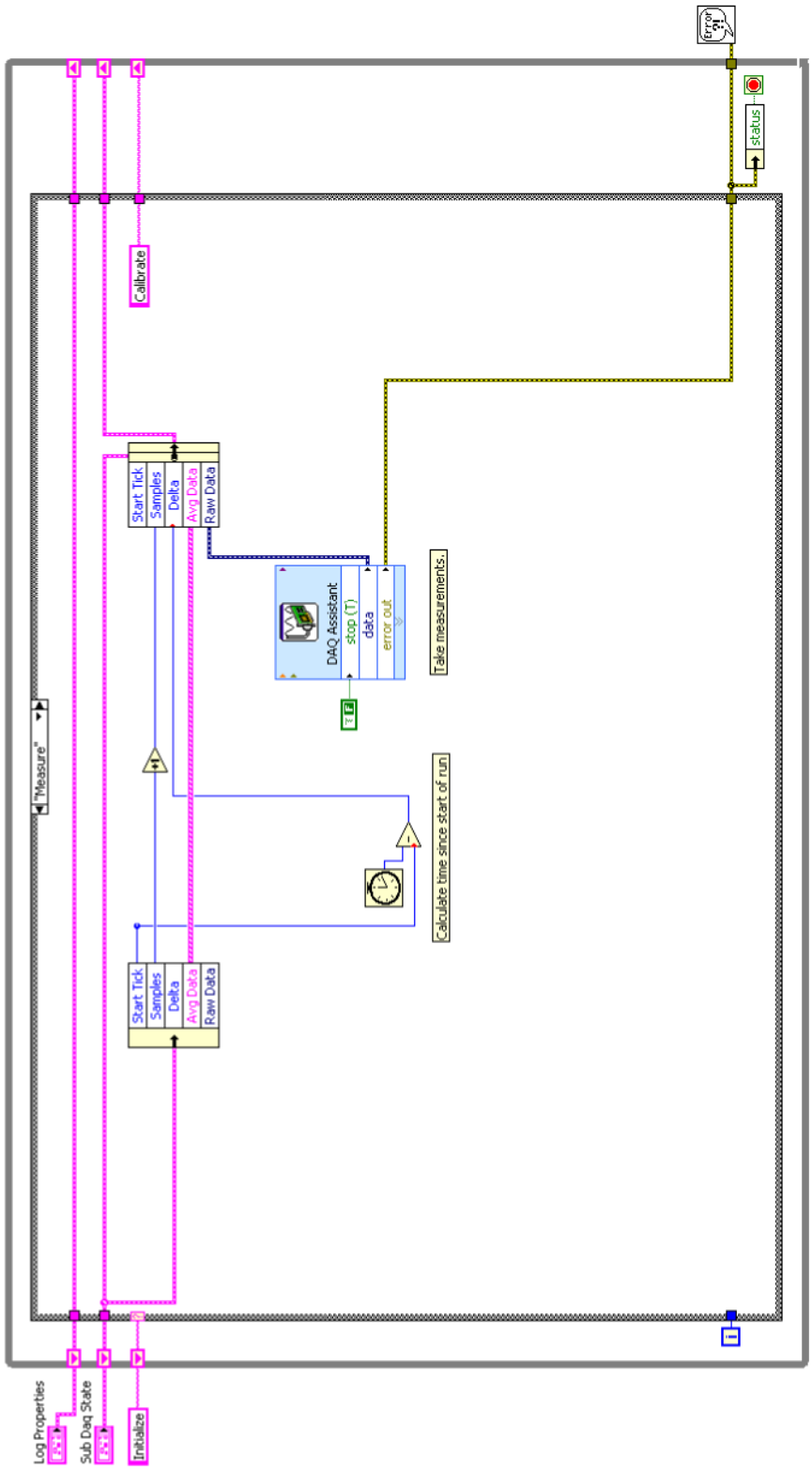

Figure A.2. Submarine DAQ VI measure state.

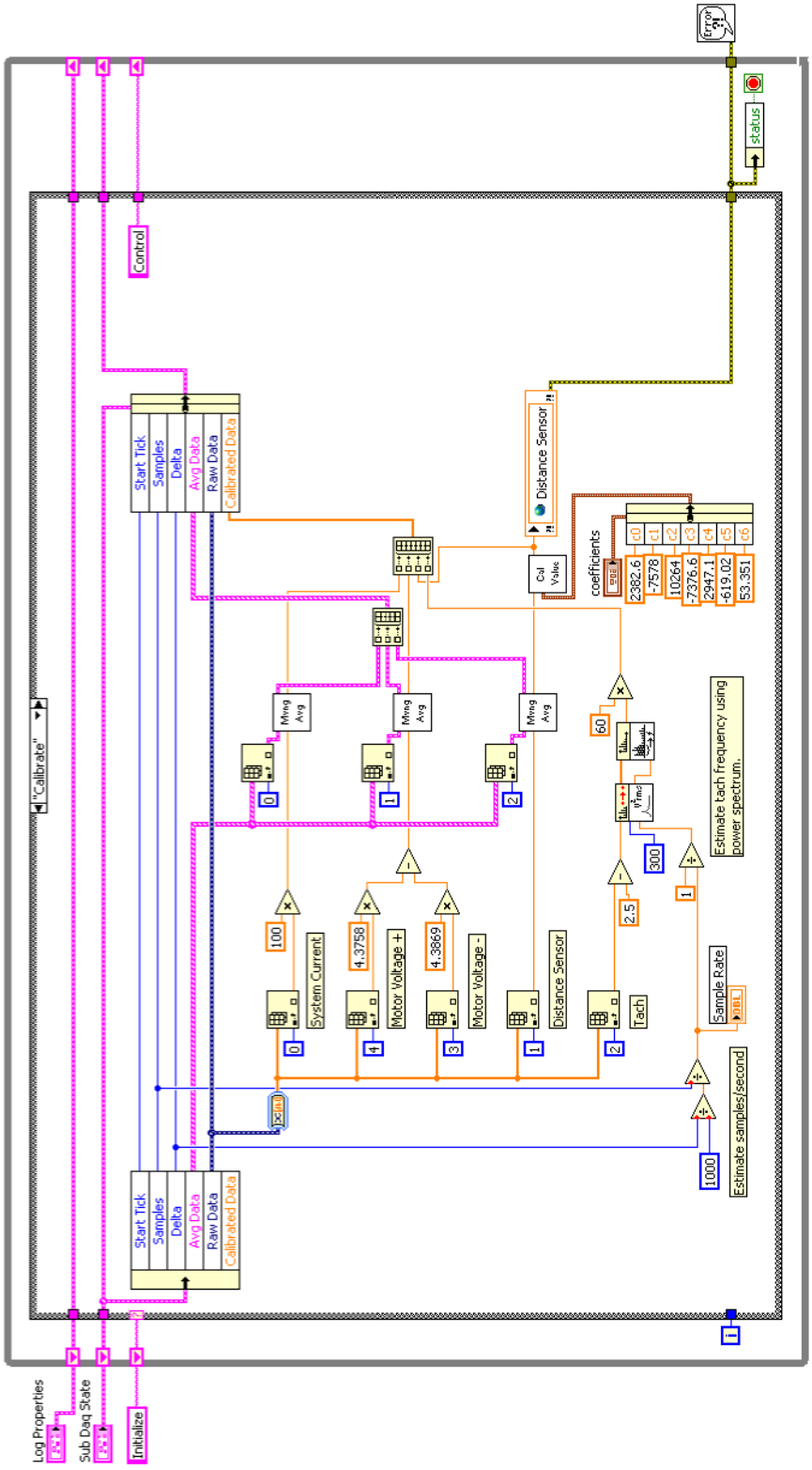

Figure A.3. Submarine DAQ VI calibrate state.

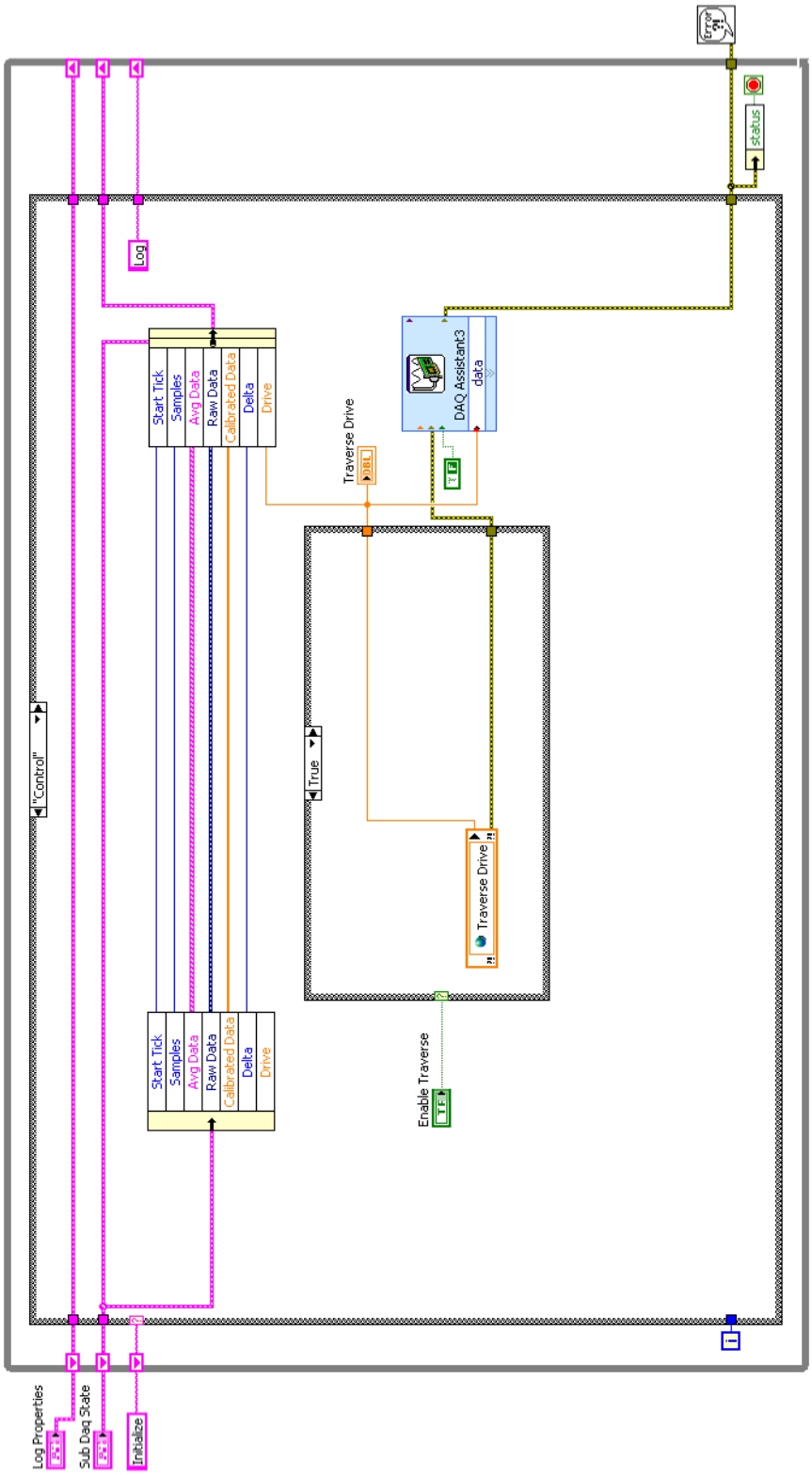

Figure A.4. Submarine DAQ VI control state.

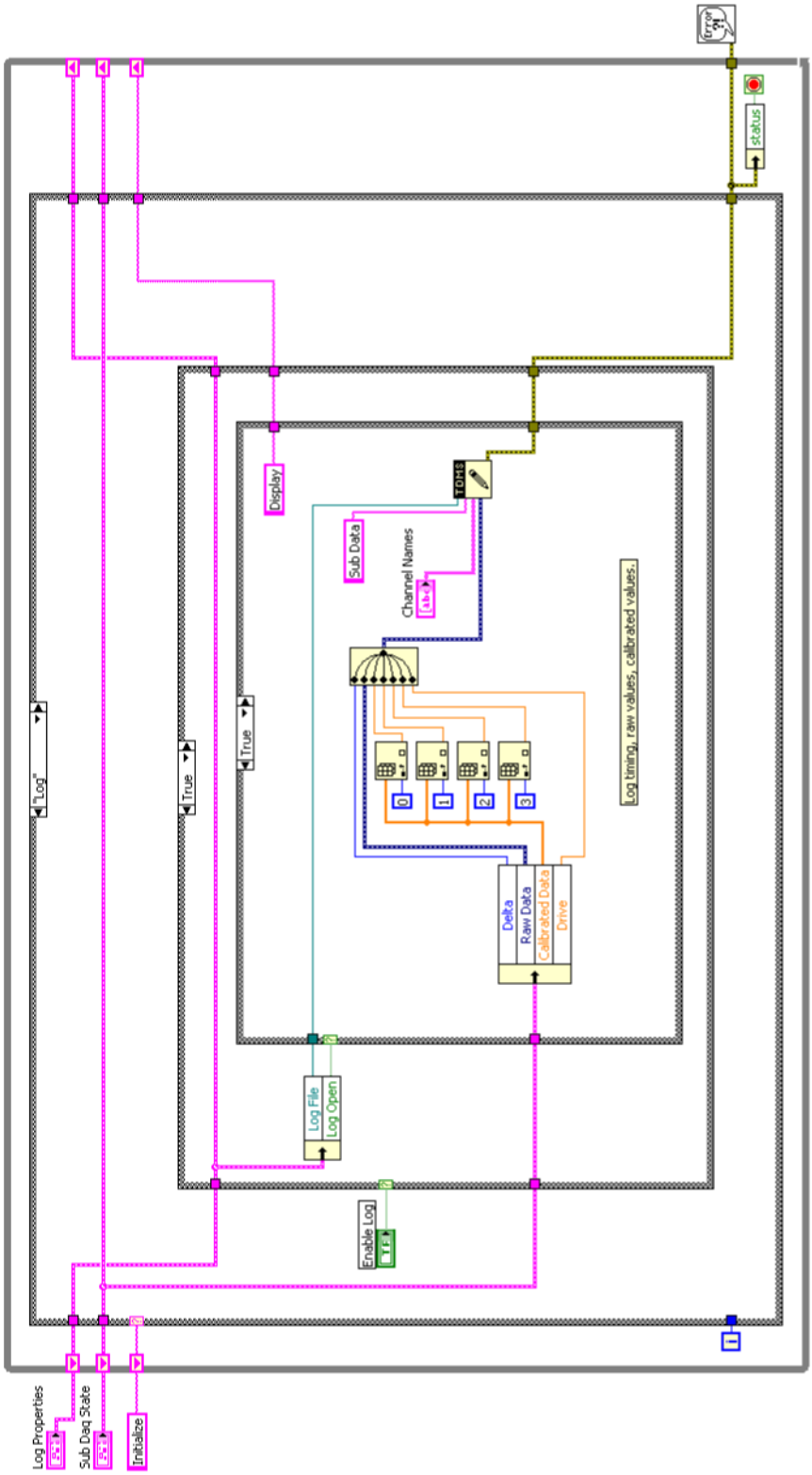

Figure A.5. Submarine DAQ VI log state.

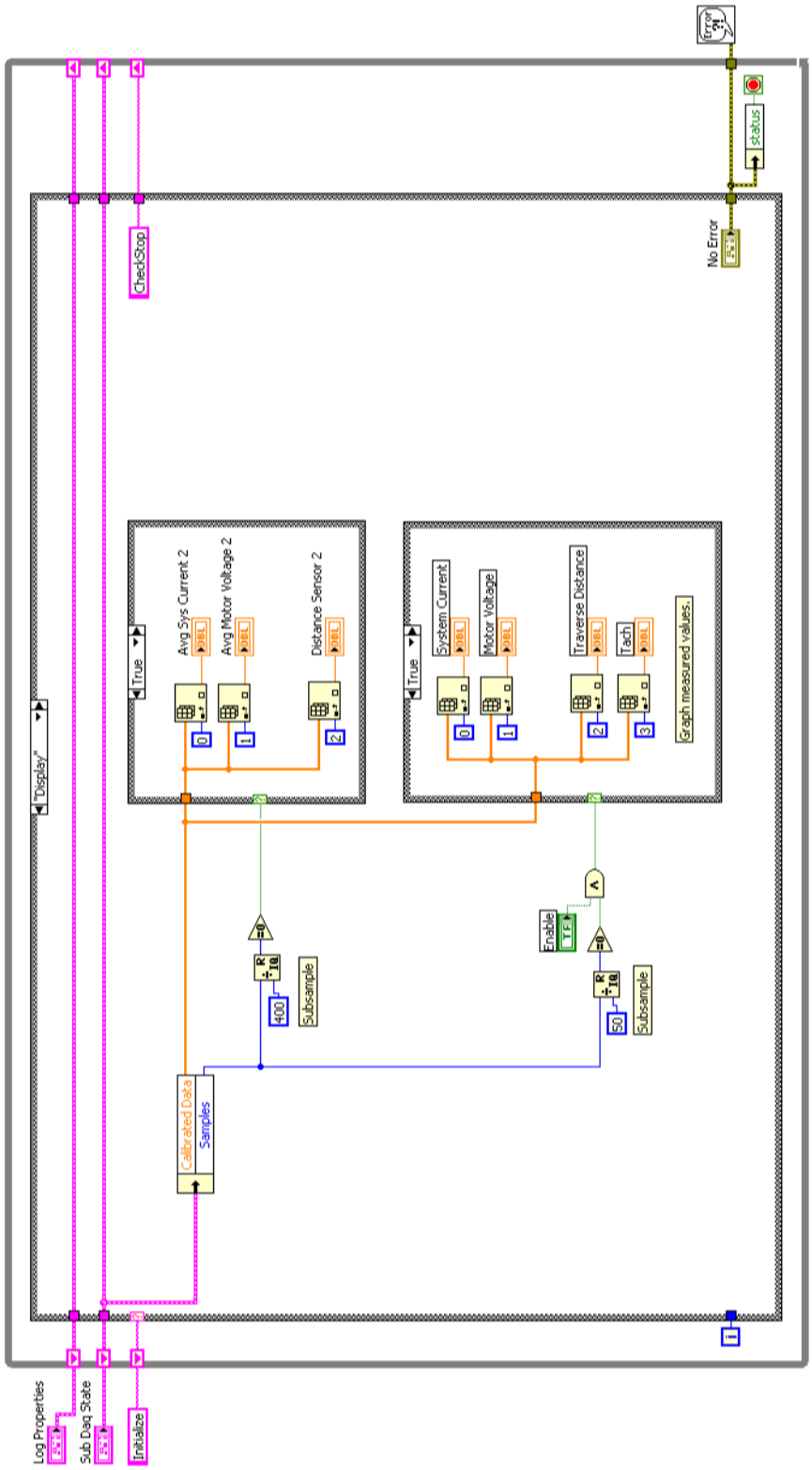

Figure A.6. Submarine DAQ VI display state.

Appendix B

Traverse Controller Implementation Details

Figure B.1 is the execution flow chart for the Traverse Controller application. Two portions of the Traverse Controller LabVIEW implementation are provided for reference. Figure B.2 demonstrates how distance measurements are received and processed. It also shows how the traverse drive value is transmitted from the application. Figure B.3 demonstrates the PID algorithm implementation.

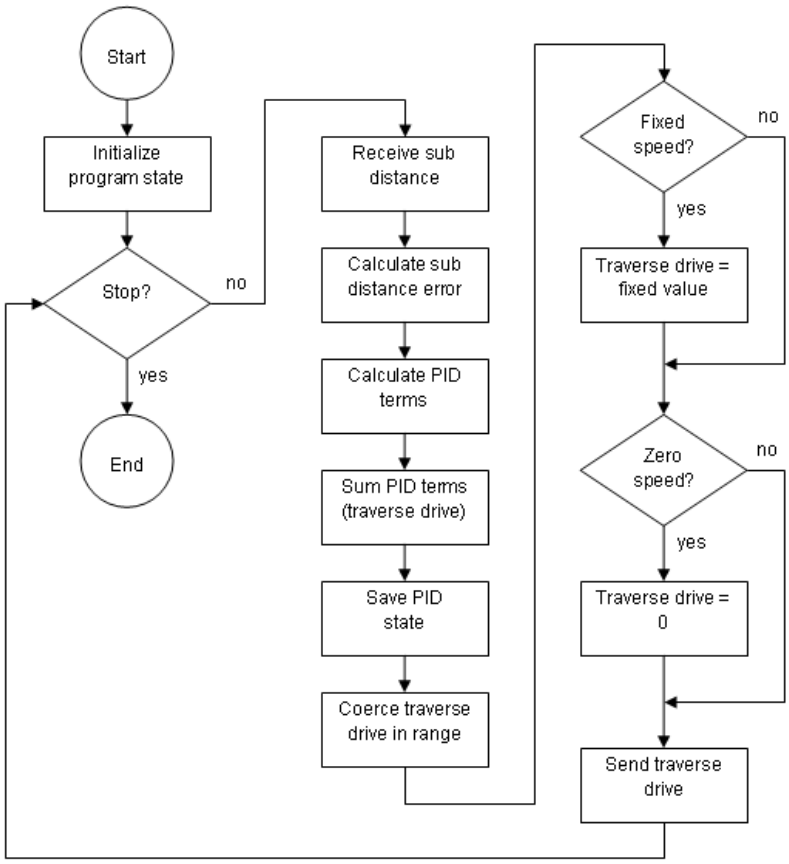

Figure B.1. Traverse Controller flow chart.

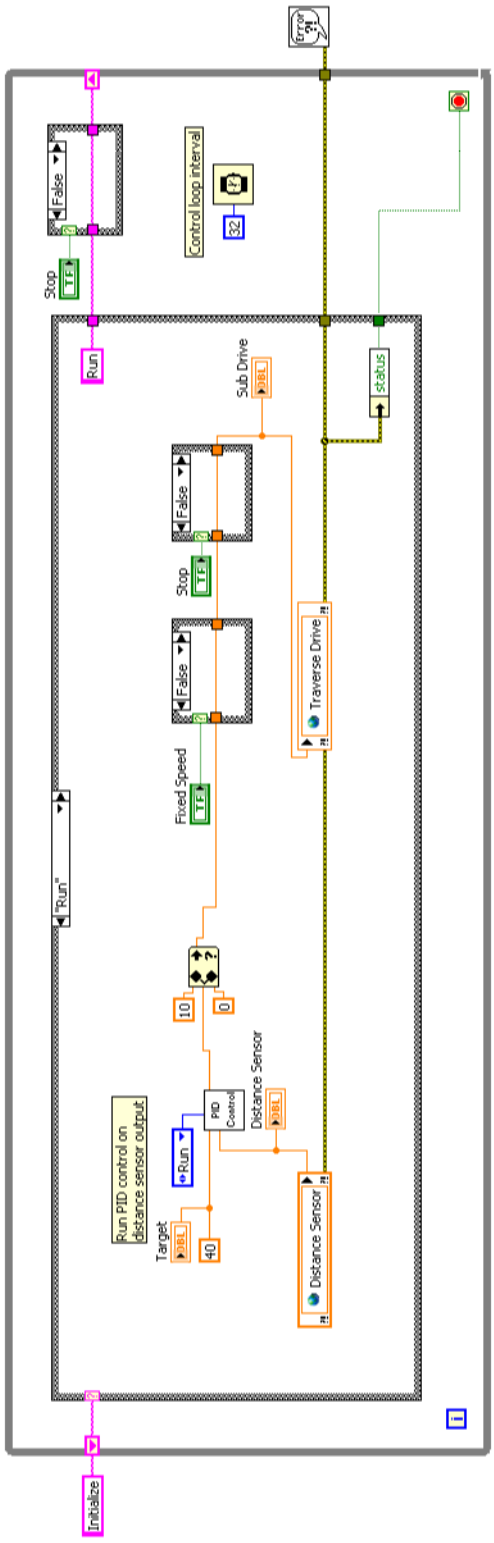

Figure B.2. Traverse Controller VI run state.

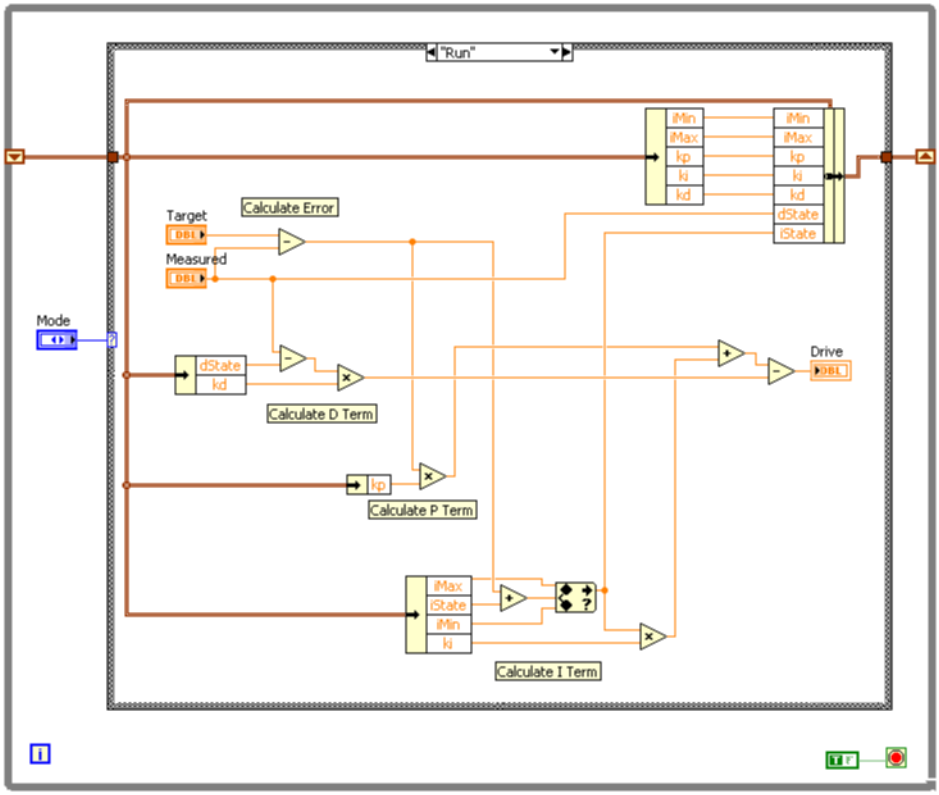

Figure B.3. PID algorithm implementation.

Appendix C

Electrical Box Wiring Diagram

Figure C.1 is the electrical box wiring diagram. Positive power lines are marked red, negative power lines are marked black and data signal lines are marked blue.

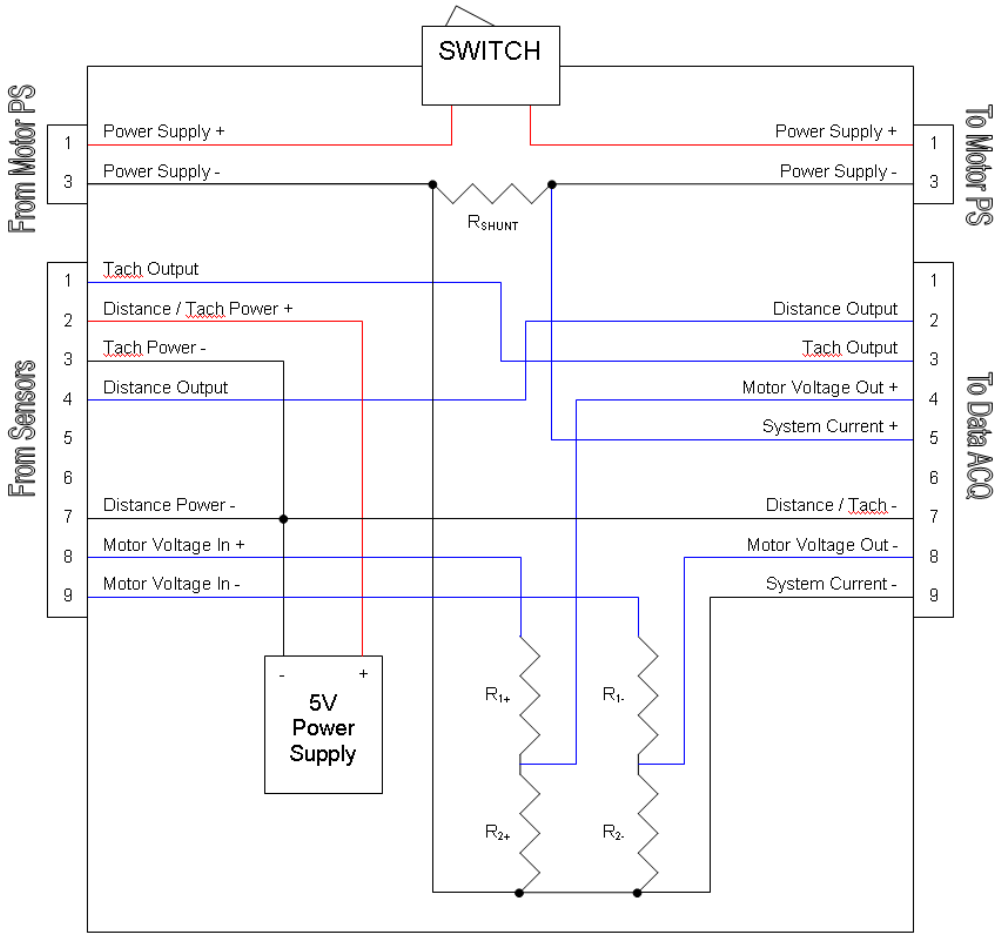

Figure C.1. Electrical box wiring diagram.

Appendix D

Summary of Data from Drag Experiments

Table D.1. Summary of experimental data for drag on traverse with vehicle attached

speed (cm/s)	σ_{speed} (cm/s)	drag (N)	σ_{drag} (N)
7.9	0.6	3.908	1.034
10.2	0.5	3.857	1.009
12.5	0.5	4.044	1.017
14.8	0.5	4.417	1.121
17.6	1.3	4.484	1.163
19.2	1.0	4.701	1.039
21.4	0.6	4.786	1.195
23.6	0.6	5.055	1.110
25.7	0.7	5.151	1.122
28.0	0.7	5.317	1.062
30.0	0.9	5.570	1.224
32.5	1.3	5.786	1.185
34.4	1.3	5.764	1.157
36.9	1.6	6.035	1.233
39.0	1.2	6.304	1.272
41.4	0.7	6.445	1.327
43.4	0.5	6.817	1.311
45.9	0.5	6.832	1.306
47.8	0.6	6.932	1.394
50.3	0.5	7.335	1.422
52.7	0.4	7.386	1.283
55.2	0.4	7.570	1.331
57.6	0.4	7.874	1.458
60.1	0.4	8.158	1.560

Table D.2. Summary of experimental data for drag on traverse without vehicle attached

speed (cm/s)	σ_{speed} (cm/s)	drag (N)	σ_{drag} (N)
7.9	0.6	3.643	0.678
10.2	0.5	3.704	0.752
12.6	0.6	3.690	0.884
14.8	0.5	3.982	0.848
17.0	1.7	4.135	0.832
19.2	1.0	4.284	0.853
21.2	0.7	4.287	0.751
23.5	0.6	4.432	0.795
25.6	0.6	4.663	0.882
27.8	0.7	4.679	0.851
29.8	0.8	4.993	0.958
32.5	1.4	5.073	0.842
34.5	1.5	5.309	0.872
36.6	1.6	5.428	0.984
39.0	1.2	5.557	0.951
41.2	0.7	5.764	0.960
43.6	0.6	5.827	0.913
45.9	0.5	6.042	1.023
48.0	2.1	6.185	0.935
50.4	0.6	6.214	1.031
52.8	0.5	6.426	1.016
55.2	0.5	6.702	0.967
57.5	0.4	6.747	1.021
59.9	0.4	6.999	1.033

Appendix E

Summary of Data from Performance Studies

Table E.1. Summary of performance data using initial motor.

Summary of Results Using Initial Motor								
Configuration	Trial	System Current (amps)	System Voltage (V)	RPM	Sub Velocity U_v (cm/s)	σ_{Uv} (cm/s)	Jet Velocity, U_{avg} (cm/s)	σ_{Uavg} (cm/s)
Steady w/out shell	1	9.89	36.61	2421	11.76	2.53	151.36	29.90
	2	12.75	36.21	2787	18.13	3.24	162.77	32.01
	3	12.33	36.24	2777	24.71	3.79	157.84	31.31
	4	11.80	36.27	2778	21.83	2.63	157.76	32.11
	5	11.96	36.13	2732	26.40	2.87	154.18	30.83
	6	9.90	35.58	2357	13.99	2.81	140.80	27.24
	7	14.01	34.69	2966	24.17	3.07	163.31	32.98
	8	13.33	34.58	2947	27.28	2.69	158.11	32.81
	9	13.73	34.39	2920	27.16	3.64	158.39	31.15
	10	13.48	34.21	2913	29.50	2.94	153.91	33.45
	11	12.07	34.46	2648	22.45	2.53	151.79	31.86
	12	12.04	34.41	2573	15.05	2.98	158.45	29.37
	13	11.34	34.38	2626	15.15	3.18	155.16	28.50
	14	11.67	34.38	2610	19.14	2.88	153.08	30.44
	15	12.29	35.99	2719	23.85	3.31	153.56	30.54
	16	12.84	36.15	2775	23.24	4.02	162.09	28.11
Steady w/ shell	1	13.60	35.80	2587	12.81	2.78	130.33	27.48
	2	14.18	35.73	2576	8.48	2.52	137.79	24.88
	3	16.44	34.00	2700	20.14	3.10	134.54	26.96
	4	16.39	33.96	2753	14.66	3.76	138.28	28.91
	5	16.37	33.86	2760	19.56	1.80	139.87	25.71
	6	15.86	33.77	2766	15.46	4.11	139.05	25.62
	7	18.22	33.02	2916	21.29	2.65	143.27	29.21
	8	18.13	32.80	2896	22.58	4.51	145.95	27.09
	9	17.98	32.69	2868	25.54	1.83	145.54	26.14
	10	18.20	32.65	2879	23.76	2.55	136.55	28.67
	11	13.71	35.95	2614	14.37	3.13	136.88	27.34
	12	13.85	36.01	2614	8.92	2.45	138.01	26.20
	13	16.00	35.53	2847	17.11	2.29	155.96	24.61
	14	15.85	35.38	2833	22.27	2.58	139.69	25.86
	15	15.48	35.30	2807	21.83	2.31	141.79	27.01
	16	15.54	35.19	2811	21.35	2.91	142.74	27.20
Pulsed	1	14.34	35.72	2559	22.65	2.82	148.04	24.70
	2	13.72	35.64	2580	18.75	3.75	147.82	27.62
	3	14.81	35.32	2543	19.48	4.05	147.79	28.21
	4	13.92	35.63	2556	21.72	4.06	145.95	27.01
	5	13.71	35.72	2609	21.41	2.53	148.02	28.47
	6	13.51	35.56	2605	19.62	3.83	148.43	28.06
	7	17.02	35.05	2820	34.26	4.34	155.01	29.33
	8	16.38	34.91	2813	32.28	3.41	151.41	28.34
	9	13.71	35.72	2609	21.41	4.13	160.39	27.86
	10	18.05	33.14	2887	32.93	4.57	154.35	28.84
	11	19.44	32.97	2959	36.48	5.10	153.26	28.46
	12	18.67	33.07	2913	37.36	2.91	150.91	28.11
	13	18.46	33.01	2906	30.74	2.64	143.03	28.84
	14	16.43	35.86	2887	35.76	3.63	146.45	29.51
	15	17.36	35.87	2867	35.20	2.95	150.33	28.01

Table E.2. Summary of performance data using second motor.

Summary of Results Using Second Motor														
Configuration	Trial	Motor Current (amps)	$\sigma_{\text{Motor Current}}$ (amps)	Motor Voltage (V)	$\sigma_{\text{Motor Voltage}}$ (V)	System Current (amps)	$\sigma_{\text{System Current}}$ (amps)	System Voltage (V)	RPM	σ_{RPM}	Sub Velocity U_v (cm/s)	σ_{Uv} (cm/s)	Jet Velocity, U_{avg} (cm/s)	σ_{Uavg} (cm/s)
Steady w/out shell	1	7.92	0.295	28.60	0.458	8.71	0.337	39.0	3152	33.1	24.16	5.28	162.13	39.11
	2	9.14	0.510	30.75	0.289	10.04	0.225	39.0	3400	29.6	33.88	4.56	169.56	41.94
	3	9.00	0.506	30.74	0.387	10.04	0.200	39.0	3240	17.5	33.22	3.55	164.23	42.95
	4	9.07	0.513	31.02	0.182	10.07	0.257	39.0	3343	13.4	34.13	3.45	165.26	40.90
	5	9.27	0.555	30.77	0.234	10.26	0.253	39.0	3381	24.4	35.81	4.69	172.92	41.39
	6	11.15	0.451	33.64	0.107	12.26	0.203	39.0	3710	30.4	41.48	5.78	181.01	46.84
	7	11.03	0.525	33.47	0.228	12.15	0.279	39.0	3756	34.2	43.25	5.95	177.74	44.88
	8	11.11	0.510	33.56	0.170	12.34	0.194	39.0	3716	39.2	43.90	6.13	180.26	45.61
	9	11.40	0.513	34.49	0.164	12.35	0.062	40.0	3830	25.8	40.11	5.50	178.11	48.50
	10	11.40	0.514	34.19	1.243	12.32	0.817	40.0	3783	29.0	43.99	4.84	173.11	51.69
	11	6.78	0.287	26.19	0.586	7.52	0.355	39.0	2896	27.2	16.71	6.13	154.22	38.00
	12	7.82	0.339	28.21	0.510	8.67	0.322	39.0	3157	35.9	25.56	6.13	157.39	38.00
Pulsed	1	11.01	0.492	29.89	0.373	12.15	0.164	39.0	3252	26.8	33.76	5.16	157.44	32.12
	2	13.16	1.236	32.58	0.151	14.81	0.1359	39.0	3508	19.5	39.58	4.81	164.93	41.94
	3	11.04	0.489	29.91	0.321	12.30	0.1998	39.0	3228	30.5	33.53	5.30	156.93	42.95
	4	13.95	0.272	33.16	0.072	15.59	0.1607	39.0	3535	23.9	44.67	5.22	169.50	40.90
	5	14.42	0.282	34.04	0.078	16.04	0.1481	40.0	3617	24.2	44.07	5.84	173.68	41.39
	6	14.32	0.362	34.02	0.077	15.97	0.2743	40.0	3627	21.3	47.02	4.58	170.40	46.84
	7	14.82	0.313	34.85	0.200	16.47	0.4173	41.0	3654	82.5	51.09	4.94	167.10	45.06
	8	15.42	0.314	35.65	0.099	17.10	0.0823	42.0	3748	38.3	53.58	2.88	176.63	36.67
	9	15.25	0.296	35.82	0.057	17.03	0.1705	42.0	3767	20.2	55.08	3.64	175.03	37.43
	10	7.70	0.380	24.91	0.733	8.42	0.3480	39.0	2745	29.3	13.87	5.04	141.90	30.00
	11	9.19	0.429	27.48	0.560	9.80	0.3620	39.0	2972	28.3	22.33	4.77	148.60	30.00
	12	11.47	0.754	30.24	0.430	12.55	0.3380	39.0	3200	29.1	32.77	5.11	157.74	32.00

Appendix F

Summary of Results Obtained Using Modeled Thrust Force

Table F.1. Summary of results obtained using modeled thrust force

Configuration	Motor Speed (rpm)	σ_{RPM}	Formation Time, t^*	Vortex Velocity, W (cm/s)	Q_{avg}/Q_o	Q_{avg} (cm^3/s)	I (Ns)	Modeled η_{hydro} (%)	Experimental η_{hydro} (%)	σ_{η_hydro} (%)
Pulsed Jet	3200	29	2.70	95.25	0.379	1082.98	0.609	47.93	43.16	7.28
	2970	28	2.74	85.46	0.410	1102.75	0.566	36.00	31.42	6.71
	2750	29	2.83	77.88	0.455	1168.23	0.547	24.17	20.04	6.73

Bibliography

Albrecht, H. E., Borys, M., Damaschke, N., and Tropea, C., 2003. *Laser Doppler and Phase Doppler Measurement Techniques*. Verlag, Berlin, New York: Springer.

Anderson, E. J. and DeMont, M. E., 2000. The mechanics of locomotion in the squid *Loligo pealei*: Locomotion function and unsteady hydrodynamics of the jet and intramantle pressure. *J. Exp. Biol.*, 203:2851–2863.

Anderson, E. J. and Grosenbaugh, M. A., 2005. Jet flow in steadily swimming adult squid. *J. Exp. Biol.*, 208:1125–1146.

Anderson, J. M. and Chhabra, N. K., 2002. Maneuvering and stability performance of a robotic tuna. *Integr. Comp. Biol.*, 42:118–126.

Auerbach, D., 1991. Stirring properties of vortex rings. *Phys. Fluids A*, 3:1351–1355.

Ayers, J., Davis, J., and Rudolph, A., editors, 2001. *Neurotechnology for Biomimetic Robots*. MIT Press.

Barrett, D. S., Triantafullou, M. S., and et al., 1999. Drag reduction in fish-like locomotion. *J. Fluid Mech.*, 392:183–212.

Bartol, I. K., Patterson, M. R., and Mann, R., 2001. Swimming mechanics and behavior of the shallow-water brief squid *Lolliguncula brevis*. *J. Exp. Biol.*, 204:3655–3682.

Batchelor, G. K., 1967. *An Introduction to Fluid Dynamics*. Cambridge: Cambridge.

Blaurock, J., 1990. An appraisal of unconventional aftbody configurations and propulsion devices. *Mar. Tech.*, 27:325–336.

Borazjani, I. and Sotiropoulos, F., 2008. Numerical investigation of the hydrodynamics of carangiform swimming in the transitional and inertial flow regimes. *J. Exp. Biol.*, 211:1541–1558.

Bremhorst, K. and Gehrke, P. J., 2000. Measured reynolds stress distributions and energy budgets of a fully pulsed round air jet. *Exp. Fluids*, 28:519–531.

Bremhorst, K. and Hollist, P. G., 1990. Velocity field of an axisymmetric pulsed, subsonic air jet. *AIAA J.*, 28:2043–2049.

Breslin, J. P. and Anderson, P., 1996. *Hydrodynamics of Ship Propellers*. Cambridge: Cambridge University Press.

Broze, G. and Hussain, F., 1994. Nonlinear dynamics of forced transitional jets: Periodic and chaotic attractors. *J. Fluid Mech.*, 263:93–132.

Broze, G. and Hussain, F., 1996. Transitions to chaos in a forced jet: Intermittency, tangent bifurcations and hysteresis. *J. Fluid Mech.*, 311:37–71.

Crow, S. C. and Champagne, F. H., 1971. Orderly stucture in jet turbulence. *J. Fluid Mech.*, 48:547–591.

Dabiri, J. O., 2004. Fluid entrainment by isolated vortex rings. *J. Fluid Mech.*, 511:311–331.

Dabiri, J. O., 2006. Note on the induced Lagrangian drift and added-mass of a vortex. *Fluid Mech.*, 547:105–113.

Dabiri, J. O., Colin, S. P., Costello, J. H., and Gharib, M., 2005. Flow patterns generated by oblate medusan jellyfish: Field measurements and laboratory analysis. *J. Exp. Biol.*, 208:1257–1265.

Dabiri, J. O. and Gharib, M., 2004. Delay of vortex ring pinchoff by an imposed bulk counterflow. *Phys. Fluids*, 16:L28–L30.

Didden, N., 1979. On the formation of vortex rings: Rolling-up and production of circulation. *Z. Angew. Math. Phys.*, 30:101–116.

Drucker, E. G. and Lauder, G. V., 1999. Locomotor forces on a swimming fish: Three-dimensional vortex wake dynamics quantified using digital particle image velocimetry. *J. Exp. Biol.*, 202:2393–2412.

Fish, F. E., 1998. Comparative kinematics and hydrodynamics of odontocete cetaceans: Morphological and ecological correlates with swimming performance. *J. Exp. Biol.*, 201:2867–2877.

Gharib, M., Rambod, E., and Shariff, K., 1998. A universal time scale for vortex ring formation. *J. Fluid Mech.*, 360:121–140.

Glauert, H., 1935. *Airplane Propellers*, volume 4. Verlag, Berlin, Germany: J. Springer.

Glezer, A., 1988. The formation of vortex rings. *Phys. Fluids*, 31:3532–3542.

Glover, E. J., 1987. Propulsive devices for improved propulsive efficiency. *Trans. Inst. Mar. Eng.*, 99:23–29.

Grim, O., 1980. Propeller and vane wheel. *J. Ship Res*, 24:203–226.

Grothues-Spork, H., 1988. Bilge vortex control devices and their benefits for propulsion. *Int. Shipbuilding Prog.*, 35:183–214.

Hadler, J. B., 1969. Contrarotating propeller propulsion-a state-of-the-art report. *Mar. Tech.*, 6:281–289.

Hill, P. G. and Peterson, C. R., 1992. *Mechanics and Thermodynamics of Propulsion.* Addison Wesley, second edition.

Ho, C. M. and Gutmark, E., 1987. Vortex induction and mass entrainment in a small-aspect ratio elliptic jet. *J. Fluid Mech.*, 179:383–405.

Husain, H. S. and Hussain, F., 1991. Elliptic jets. Part 2. Dynamics of coherent structures: Pairing. *J. Fluid Mech.*, 233:439–482.

Husain, H. S. and Hussain, F., 1993. Elliptic jets. Part 3. Dynamics of preferred mode coherent structure. *J. Fluid Mech.*, 248:315–361.

Krueger, P. S., 2001. The significance of vortex ring formation and nozzle exit over-pressure to pulsatile jet propulsion. Ph.D. thesis, California Institute of Technology.

Krueger, P. S., 2005. Thrust augmentation and vortex ring evolution in a fully pulsed jet. *AIAA J.*, 43:792–801.

Krueger, P. S., 2006. Measurement of propulsive power and evaluation of propulsive performance from the wake of a self-propelled vehicle. *Bioinsp. Biomim.*, 1:49–56.

Krueger, P. S., Dabiri, J. O., and Gharib, M., 2006. The formation number of vortex-rings formed in uniform background co-flow. *J. Fluid Mech.*, 556:147–166.

Krueger, P. S. and Gharib, M., 2003. The significance of vortex ring formation to the impulse and thrust of a starting jet. *Phys. Fluids*, 15(5):1271–1281.

Liepmann, D. and Gharib, M., 1992. The role of streamwise vorticity in the near-field entrainment of round jets. *J. Fluid Mech.*, 245:643–668.

Lim, T. T. and Nickels, T. B., 1995. *Vortex Rings. In Fluid Vorticies*. Kluwer Academic Publications.

Maxworthy, T., 1977. Some experimental studies of vortex rings. *J. Fluid Mech.*, 81:465–495.

Milne-Thomson, 1960. *Theoretical Hydrodynamics*. MacMillan Company.

Narita, H., Yagi, H., Johnson, H. D., and Breves, L. R., 1981. Development and full-scale experiences of a novel integrated duct propeller. *Trans. SNAME*, 89:319–346.

Nauen, J. C. and Lauder, G., 2002. Quantification of the wake of rainbow trout using three-dimensional stereoscopic digital particle image velocimetry. *J. Exp. Biol*, 205:3271–3279.

Nitsche, M., 1996. Scaling properties of vortex ring formation at a circular tube opening. *Phys. Fluids*, 8:1848–1855.

Olcay, A. B. and Krueger, P. S., 2008. Measurement of ambient fluid entrainment during laminar vortex ring formation. *Exp. Fluids*, 44:235–247.

Pullin, D., 1979. Vortex ring formation at tube and orifice opening. *Phys. Fluids*, 22:401–403.

Reynolds, W. C., Parek, D. E., and et. al., 2003. Bifurcating and blooming jets. *Annu. Rev. Fluid Mech.*, 35:295–315.

Sachs, A. H. and Burnell, J. A., 1962. Ducted propellers-a critical review of the state-of-the-art. *Prog. Aeronaut. Sci.*, 3:85–135.

Saffman, P. G., 1978. The number of waves on unstable vortex rings. *J. Fluid Mech.*, 84:625–639.

Schultz, W. W. and Webb, P. W., 2002. Power requirements of swimming: Do new methods resolve old questions? *Integr. Comp. Biol.*, 42:1018–1025.

Shadden, S. C., Katija, K., and et al., 2007. Transport and stirring induced by vortex formation. *J. Fluid Mech.*, 593:315–331.

Shariff, K. and Leonard, A., 1992. Vortex rings. *Annu. Rev. Fluid Mech.*, 24:235–279.

Smits, A. J. and Lim, T. T., editors, 2000. *Flow Visualization: Techniques and Examples*. Imperial College Press.

Stipa, L., 1931. Experiments with intubed propellers. Technical report, NACA Technical Report TM 655.

Tangorra, J. L., Davidson, S. N., and et al., 2007. The development of a biologically inspired propulsor for unmanned underwater vehicles. *IEEE J. Oceanic Eng.*, 32:533–550.

Tytell, E. D., 2004. The hydrodynamics of eel swimming II. Effect of swimming speed. *J. Exp. Biol.*, 207:3265–3279.

Tytell, E. D. and Lauder, G. V., 2004. The hydrodynamics of eel swimming I. Wake structure. *J. Exp. Biol.*, 207:1825–1841.

Vermeulen, P. J., Rainville, P., and Ramesh, V., 1992. Measurements of the entrainment coefficient of acoustically pulsed axisymmetric free air jets. *J. Eng. Gas Turb. Power*, 114:409–415.

Weihs, D., 1977. Periodic jet propulsion of aquatic creatures. *Forts. Zool.*, 24:171–175.

Willert, C. E. and Gharib, M., 1991. Digital particle image velocimetry. *Exp. Fluids*, 10:181–193.

Yeh, Y. and Cummins, H., 1964. Localized fluid flow measurements with a he-ne laser spectrometer. *Appl. Phys. Lett.*, 4:176–178.